

Implementation of Novel Deep Learning Algorithms for the High-resolution Study of the  
Lacuno-Canalicular Network from Individuals with a Documented History of Chronic Opioid  
Use

by © Joshua Thomas Taylor, B.Sc.

A thesis submitted to the School of Graduate Studies in partial fulfillment of the requirements for  
the degree of Master of Science in Medicine (Bioscience of Health and Disease).

Biomedical Sciences

Faculty of Medicine

Memorial University of Newfoundland

St. John's, Newfoundland, Canada

October 2024

## Abstract

Bone is a dynamic tissue that changes throughout life. This process is governed by osteocytes that exist in a lacuno-canalicular network (LCN), but is altered by several factors, including exercise, age, nutrition, and substance use. Artificial intelligence brought several enhancements to image segmentation for medical imaging. However, it has not been applied to study the LCN in human bone. This thesis implements novel deep learning methods on Synchrotron Radiation micro-Computed Tomography (SR $\mu$ CT) datasets of human rib cortical bone microstructure to characterize osteoporosis-related features.

Ninety-seven human left sixth rib specimens (male:  $n = 60$ , female  $n = 37$ ) were excised from cadavers with informed consent. The specimens were divided into age categories defined by decade. A 50-slice subset from six samples was segmented to train the U-Net++ deep learning model. It was compared to traditional and manual segmentation methods. Deep learning performed comparably to the traditional method, although it was more time-efficient. A follow-up model with the MA-Net architecture more accurately segmented the data. Comparing segmented microstructural parameters with opioid use, sex, and age revealed age as the most significant predictor of deteriorating bone health. The results did not provide strong evidence of drug-induced impacts on bone health as originally predicted, however, there are some indications hinting at a link between opioid use and bone health. A follow-up study implementing a rabbit model is underway to eliminate confounding factors present in a human population. However, this project successfully created a novel segmentation algorithm that performed more efficiently in SR $\mu$ CT data segmentation.

## **General Summary**

Bone tissue is composed of cells that alter its structure throughout life to maintain its health and stability. These cells coordinate responses to various stimuli, and are impacted by exercise, age, nutrition, and substance use. Traditional methods for analyzing bone health are time-consuming and cumbersome. However, innovations in computer science and artificial intelligence have facilitated new pathways for the automatic classification of structures for analysis. This thesis sought to utilize these new techniques to identify the impacts of opioid use on bone health.

Left sixth rib specimens were collected from 97 cadaveric specimens with a history of opioid abuse. The specimens were imaged using high-resolution imaging modalities. The novel techniques performed significantly better than the current techniques. The results did not reveal an impact of opioid use on the bone cellular network. A rabbit model is underway to tease out additional variables that affect bones.

## **Acknowledgments**

This endeavor would not have been accomplished without the tremendous support of countless individuals. First and most importantly, I want to thank my incredible supervisor, Dr. Janna M. Andronowski, for the conceptualization of the project and her careful supervision. Additionally, for her companionship throughout the entire process. Some of those highlights include bringing supplies and checking-in during MUN's two-week mandatory quarantine, road trip to Bonaventure to see Icey, Iceberg Alley, the countless beer runs, and road trip to Ohio. Of course, that includes suiting up for cadaveric dissections four hours into the road trip with a remaining two hours of driving afterward. This does not even remotely cover all of the fun activities, birthdays, and holidays we celebrated here, not to mention in my undergraduate program in Ohio. However, I would be remiss if I did not acknowledge the incredible amount of joy you brought me in the form of four adorable furry nurses. Thank you for taking a shot on me, providing the best graduate experience, and your continued support. It means more than you will ever know.

Thank you to Dr. Jessica Esseltine for your expertise and insight on the direction of the project and for providing invaluable feedback. Also, thank you to the Associate Dean of Research and Graduate Studies, Dr. Ann Dorward, for your endless support and encouragement. Additionally, I want to thank the beamline scientists at the Canadian Light Source for their invaluable assistance. Specifically, Dr. Arash Panahifar for his assistance in scheduling, Dr. Sergey Gasilov for his co-development of the reconstruction software and assistance in downloading it. Finally, I want to thank Drs. Adam Webb and Ning Zhu for preparing our imaging setup, calibrating it, and assisting us whenever we need it (even in the middle of the night!). Without this dedicated support team, this project would not have been completed. You all have my immense gratitude!

To my mom, who has helped supported me in every conceivable way since my birth. Thank you for being so incredibly strong in supporting two kids financially and as a mother, even though I know I was unbearable at times. This year is an important year in my life, it signifies the first year where you have been my sole parent for half of my life. Looking back on it now, I was so fortunate to have an awesome mom like you in my corner to support me through it all, even as a father.

Finally, I'd like to acknowledge all current and former Andronowski Lab members that have taught me so many invaluable life skills and bone biological concepts over the years as well as just being there for good company. Thank you to Reed Davis, Randi Depp, Mary Beth Cole, Gina Tubo, Kelly Cooper, Kassidy Wilson, Abigail LaMarca, Jacob Haschak, Sydney-Quinn Chizmeshya, Medhat Hassan, Shreya Hande, David Bennin, and Nafiza Haque. There is one last former Andronowski Lab member that deserves special recognition, so here's to you my first-grade friend, Logan Usher. Your simple and short recommendation to take the 'Human Anatomy for Biology Major's' course because of the invaluable access to cadaver and the amazing professor that taught the course. That simple conversation sitting in the lecture hall waiting for 'Cell and Molecular Biology' to start was undeniably life altering because it was Dr. Janna M. Andronowski that taught the course. That conversation led me to being here in Canada today, 5 years later, submitting my Master's thesis under her supervision.

## **Co-Authorship Statement**

Dr. Janna M. Andronowski provided the conceptualization, experimental imaging assistance of the synchrotron radiation micro-computed tomography imaging experiments at the Canadian Light Source (CLS), and supervision to this project. Additionally, Sydney-Quinn Chizmeshya and Medhat Hassan provided assistance with the synchrotron radiation micro-computed tomography imaging experiments at the Canadian Light Source. Gina Tubo acquired the raw image used in **Figure 1.3**. Drs. Adam Webb and Ning Zhu are beamline scientists at the Canadian Light Source that set up the imaging parameters and provided assistance whenever needed. Dr. Sergey Gasilov co-developed the tofu software used in this thesis to reconstruct data and provided assistance with its installation. Dr. Jessica Esseltine for the critical and insightful reviews. In completion of this project, I processed and prepared all 97 samples for imaging and assisted in imaging them at CLS. I downloaded CentOS and Ubuntu operating systems along with the reconstruction software on our workstations. I handled all data transfers, reconstructions, and deep learning model development. I was the sole person responsible for the statistical analyses and writing of the thesis with feedback from Dr. Andronowski.

## **Funding**

This research was funded by the School of Graduate Studies (SGS), Canadian Institutes of Health Research Project Grant (180520) awarded to Dr. Andronowski, MUN Faculty of Medicine's Dean's Fellowship Award (Master's), and a Graduate Research Fellowship from the Aging Research Centre -- Newfoundland and Labrador.

## **Ethics Statement**

Regarding the human bone tissue specimens used for this research, procurement protocols and anatomical specimen requests were prepared for each institution/organization according to proprietary protocols and were reviewed and approved by Medical Advisory Boards and/or Ethics Panels. These agreements subsequently allowed for the routine collection of cadaveric bone specimens in accordance with Medical Research guidelines. The study of the skeletal material was ethically cleared by The University of Akron Institutional Review Board for the Protection of Human Subjects and the Newfoundland and Labrador Health Research Ethics Board (Protocol Reference #2020.308). All cadaveric samples were collected with strict ethical oversight and explicit informed consent from the donor or next of kin. For organ donors, advanced procurement coordinators, who are responsible for securing authorizations to collect organs and tissues (e.g., heart valves, bone, corneas), specifically request permission to remove tissues for research.

## **Conflict of Interest**

I, Joshua Thomas Taylor, declare no conflict of interests. The funders had no role in the design of the study; in the collection, analyses, or interpretation of data; in the writing of the manuscript, or in the decision to publish the results.

# Table of Contents

<b>1. INTRODUCTION.....</b>	<b>14</b>
1.1 THE BONE HIERARCHICAL SYSTEM.....	14
1.2 BONE TYPES.....	16
1.3 BONE TISSUE TYPES.....	16
1.4 TYPES OF BONE CELLS.....	17
1.5 BONE EXTRACELLULAR MATRIX.....	23
1.6 THE LACUNO-CANALICULAR NETWORK.....	24
1.7 BASIC MULTICELLULAR UNITS AND SKELETAL REMODELING.....	26
1.8 OSTEOPOROSIS.....	31
1.9 CURRENT AND PROJECTED TRENDS IN OPIOID USAGE.....	32
1.10 OPIOIDS' INFLUENCE ON BONE HEALTH.....	35
1.11 QUANTIFICATION OF CORTICAL BONE MORPHOLOGY.....	37
1.12 SYNCHROTRON RADIATION MICRO-COMPUTED TOMOGRAPHY.....	39
1.13 DEEP LEARNING.....	41
1.14 RESEARCH OBJECTIVES:.....	45
<b>2. MATERIALS AND METHODS.....</b>	<b>46</b>
2.1 SAMPLE PROCUREMENT.....	50
2.2 SAMPLE PREPARATION.....	50
2.3 IMAGING.....	52
2.4 IMAGE PROCESSING.....	52
2.5 IMAGE SEGMENTATION.....	53
2.6 DEEP LEARNING.....	53
2.7 STATISTICAL ANALYSIS.....	54
<b>3. RESULTS.....</b>	<b>58</b>
3.1 KRUSKAL-WALLIS NONPARAMETRIC TESTS REVEALED SIGNIFICANT DIFFERENCES BETWEEN AGE, SEX, AND OPIOID USE.....	68
3.2 GENERAL AGE-RELATED TRENDS OF DECLINING LACUNAR MORPHOLOGY IS DISRUPTED BY OPIOID USE AND MALE.....	79
3.3 CTAN OUTPERFORMED DEEP LEARNING IN SEGMENTATION ACCURACY.....	86
3.4 DEEP LEARNING OUTPERFORMED CTAN USING A DIFFERENT MODEL ARCHITECTURE.....	88
<b>4. DISCUSSION.....</b>	<b>94</b>
4.2 DEEP LEARNING IS COMPARABLE TO TRADITIONAL SEGMENTATION METHODS WITH QUICKER PROCESSING TIMES.....	95
4.3 AGE IS THE STRONGEST PREDICTOR OF DETERIORATING BONE HEALTH FOLLOWED BY SEX.....	98
4.5 LIMITATIONS.....	106
<b>5. CONCLUSIONS.....</b>	<b>110</b>
<b>6. REFERENCES.....</b>	<b>111</b>
<b>7. APPENDICES.....</b>	<b>132</b>
APPENDIX 7.1: ETHICS APPROVAL RENEWAL.....	133
APPENDIX 7.2: DEEP LEARNING TRAINING TESTS.....	136
APPENDIX 7.3: EXTRACTING DATA WITH CTAN FROM ORS DRAGONFLY DEEP LEARNING OUTPUTS.....	145



**List of Tables:**

Table 1.1 – Standard bone nomenclature

Table 1.2 – CTAn Terminology

Table 2.1 – Opioid use history

Table 2.2 – CTAn to SR $\mu$ CT Terminology

Table 3.1 – Sample breakdown

Table 3.2 – Descriptives for lacunar and pore variables

Table 3.3 – Normality and homogeneity tests for lacunar and pore variables

Table 3.4 – Log-transformed normality and homogeneity tests for lacunar and pore variables

Table 3.5 – Kruskal-Wallis nonparametric tests for lacunar variables

Table 3.6 – Kruskal-Wallis nonparametric tests for pore morphometric

Table 3.7 – ANOVA tests

Table 3.8 – DICE and TPR

Table 3.9 – DICE and Accuracy

## List of Figures

Figure 1.1 – Hierarchical structure of bone

Figure 1.2 – Direct and indirect effects of opioids on bone

Figure 1.3 – Confocal laser scanning microscopy image of the lacuno-canalicular network

Figure 1.4 – Typical BMU

Figure 1.5 – Example of endocortical remodeling

Figure 1.6 – An example of a synchrotron facility

Figure 1.7 – An example of a multi-layered neural network

Figure 2.1 – Statistical workflow

Figure 3.1 – SR $\mu$ CT render of age-associated bone decline

Figure 3.2 – Significant Kruskal-Wallis bar graphs

Figure 3.3 – SR $\mu$ CT render of bone quality with opioid use

Figure 3.4 – Linear regression

Figure 3.5 – Multiple linear regression split by age and opioid use

Figure 3.6 – Multiple linear regression split by age and sex

Figure 3.7 – SR $\mu$ CT render of bone health between sexes

Figure 3.8 – Accuracy and DICE scores

Figure 3.9 – Segmentation comparison by ANOVAs

## **List of Appendices**

Appendix 6.1 – Deep learning tests

Appendix 6.2 – Data extraction

## **List of Acronyms**

AI – artificial intelligence

ANOVA – Analysis of variance

ARF Sequence – Activation, Resorption, Formation sequence

ARRFMQ sequence – Activation, Resorption, Reversal, Formation, Mineralization, Quiescence sequence

ASBMR – American Society of Bone Mineral Research

BLC – Bone-lining cells

BMD – Bone mineral density

BMIT-BM – BioMedical Imaging and Therapy Bend Magnet

BMU – Basic multicellular unit

CLS – Canadian Light Source

DOR – Delta opioid receptor

DXA – Dual X-ray absorptiometry

HPA – Hypothalamic pituitary adrenal axis

HPG – Hypothalamic pituitary gonadal axis

IGF-1 – Insulin-like growth factor-1

IKK – Inhibitors of NF-kappa $\beta$  kinase

JNK – c-Jun N-Terminal Kinase

KOR – Kappa opioid receptor

LCN – Lacuno-canalicular network

M-CSF – Macrophage colony-stimulating factor

Nano-CT – Nano-Computed Tomography

OGFR – Opioid Growth Factor Receptor

OPG – Osteoprotegerin

OPIAD – Opioid-induced androgen deficiency

OPO – Organ procurement organization

PTH – Parathyroid hormone

RANK – Receptor Activator for nuclear kappa-B

RANKL – Receptor activator for nuclear factor kappa-B ligand

ROI – Region of interest

Sema4d – Semaphorin 4D

SHBG – Sex hormone binding globulin

SLS – Swiss Light Source

SMI – Structural model index

Spring 8 – Super Photon Ring-8

SR $\mu$ CT – Synchrotron Radiation micro-Computed Tomography

SSRF – Shanghai Synchrotron Radiation Facility

TPR – True positive rate

TRAF – TNF receptor-associated factors

WHO – World Health Organization

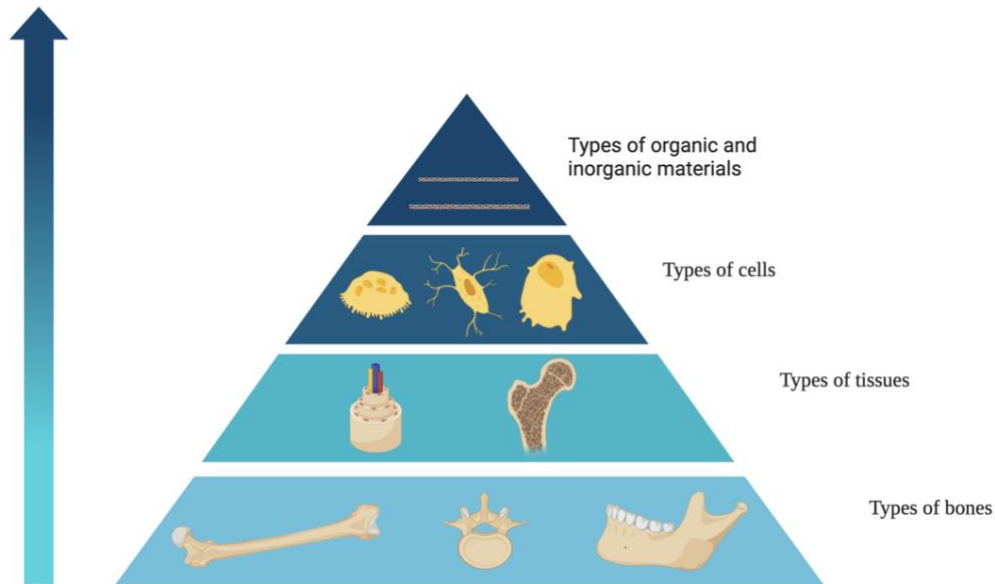
## **1. Introduction**

### **1.1 The Bone Hierarchical System**

The skeletal system is a highly dynamic organ that impacts other systems in the human body. Bones are continuously adapting to internal and external stimuli, including hormonal fluctuations and changing mechanical demands<sup>1-5</sup>. Further, bones are explicitly involved in maintaining calcium homeostasis, acting as a framework for muscle movement, and protecting internal organs<sup>6-9</sup>. These are but a few of the several important physiological processes that the skeletal system is involved in.

Bone itself is hierarchical, with complex compositions at each structural level<sup>6,10</sup> (**Figure 1.1**). At the surface level, bones can be separated into categories based on their shape which is important in the function of the skeletal elements. Further, all bones are comprised of cortical and trabecular bone layers which have distinct mechanical properties that contribute to the bone's mechanical environment. In order to coordinate and maintain the skeletal system, three main cell types work in tight regulation: osteocytes, osteoblasts, and osteoclasts. The cells work to regulate the amount and quality of the neighboring mineralized bone matrix which is primarily composed of individual crystals and collagen fibrils.

# Bone Hierarchical Structure



**Figure 1.1.** The hierarchical structure of bone. The most macroscopic categorization of bone is into long bones (e.g., femoral, radius) and flat bones (e.g., frontal, temporal) followed by the types of tissues (cortical and trabecular). Further delving into bone structure, the types of cells can be distinguished (e.g., osteoblast, osteoclast, osteocytes, bone lining cells). At the nanoscale resolution, the individual components of bone can be appreciated, including collagen fibrils and hydroxyapatite. This figure was created in BioRender.

## **1.2 Bone Types**

There are five major types of bones; long, short, flat, irregular, and sesamoid bones. Long bone morphology can be separated into three distinct regions; epiphyses, metaphyses, and diaphysis<sup>11</sup>. The epiphysis is either end of the long bone and contains an articular surface that allows the bone to associate with the bones superior and inferior to it. The articular surface is covered in articular cartilage, just beneath the cartilage is subchondral bone. This layer of bone acts as a shock absorber during mechanical loading<sup>12</sup>. The metaphysis is funnel-shaped and growth occurs from this region. The final region is the diaphysis which is a shaft that connects the two metaphyses together.

Short bones are cubed-shaped bones containing the carpals and tarsals of the hand and ankle. Flat bones are usually long and flat. They are not typically exposed to high mechanical loads, so they remain largely unaffected by exercise and other activities. Irregular bones do not fit neatly into any of the other categories. Vertebrae, os coxae, and scapulae are all examples of irregular bones. The os coxae and scapulae provide attachment sites for the limbs to facilitate movement. The final category, sesamoid bones, are a special categorization of bones where the skeletal element itself does not directly articulate with another bone<sup>13</sup>. The most well-known example is the patella or the 'knee cap'. The patella is encased in the quadriceps femoris tendon and acts as a jib to reduce the force required by adding torque to the system<sup>14</sup>.

## **1.3 Bone Tissue Types**

All bones are composed of two types of tissue: cortical and trabecular bone. The primary difference between these tissue types is the density of bone and consequently the amount of empty porous



space within them. Cortical (compact) bone is highly dense and has between 5-15% porosity. As a result, cortical bone is more resistant to mechanical regions than trabecular bone. As such, cortical bone is usually found as the outer layer of all bones providing a hard protective shell. This outer protective shell is referred to as the periosteal surface and is covered in soft tissue called the periosteum. Further, diaphyses of all long bones are primarily composed of cortical bone because of the concentration of mechanical strain to smaller regions. Due to its strong mechanical competency, cortical bone comprises 80% of the adult human skeleton<sup>15</sup>.

Trabecular (spongy or cancellous) bone is the compromise in mechanical resistance and material requirement. It has a porosity closer to 75% making it lightweight, especially in comparison to cortical bone<sup>16-18</sup>. Another key characteristic are unique structures termed trabecular struts. They are similar to I beams in a house. They provide structural support to the skeletal system without using too much space or material. They are typically concentrated in epiphyses and metaphyses of long bones, although they line inside of most bones. Additionally, these struts are usually aligned in an isotropic direction that corresponds with their principal mechanical demand. To resist stress in any particular direction, a trabecular strut has to be aligned in that direction. Struts that are not aligned in that direction are anisotropic. The general measure of a regions of the alignment of these struts is the degree of anisotropy.

#### **1.4 Types of bone cells**

The cortical and trabecular tissues are governed and maintained by four main bone cells: osteoblasts, osteoclasts, osteocytes, and bone lining cells (BLC). Each play a role in the

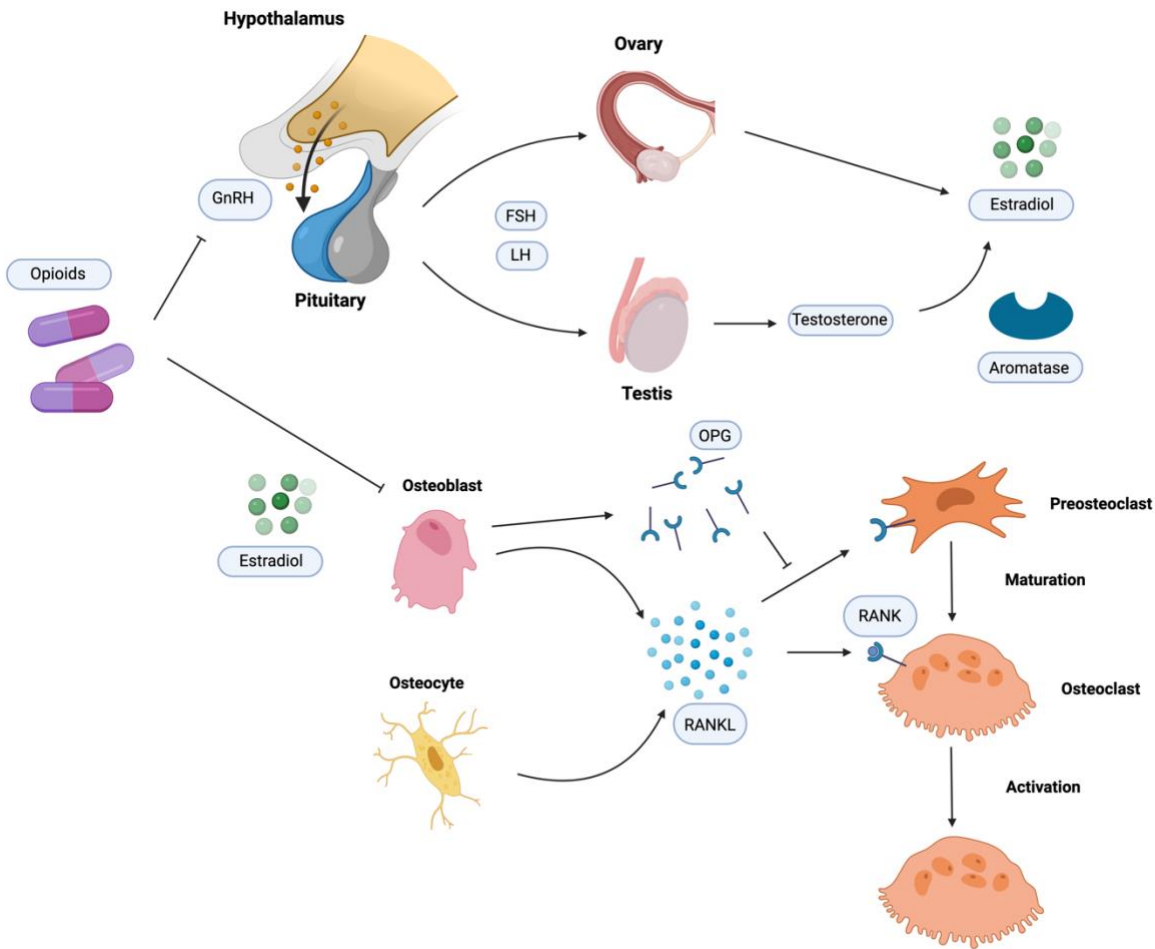
maintenance of bone tissues. Osteoblasts form new bone by secreting osteoid, a matrix of type 1 collagen, water, and non-collagenous proteins and then mineralize the tissue with hydroxyapatite,  $\text{Ca}_5(\text{PO}_4)_3(\text{OH})^{19}$ , forming a complete packet of bone. Osteoclasts remove old packets of bone by sealing them up and using hydrochloric acid and cathepsin, among others, to dissolve hydroxyapatite and the collagenous matrix, respectively. Osteocytes are the most ubiquitous cell in bone (95%) and work to modify their localized environment while coordinating the osteoblasts and osteoclasts in a larger scale bone remodeling process<sup>2,20,21</sup>. The BLCs have a similar function to osteocytes, however as their name implies, they line the inner and outer surfaces of bones. The function of these cells and their roles in bone remodeling will be discussed further in **section 1.7**. Despite these bone cells all working together in the maintenance of bone tissues, they have different origins.

Osteoblasts originate from mesenchymal stem cells located in bone marrow. These stem cells are encouraged to differentiate and mature into osteoblasts in response to complex coordination of pathways and gene expression (e.g., Wnt signaling, osterix). However, Runx2 is the master gene for osteoblast production, and it is highly conserved in the class Mammalia<sup>22</sup>. Evidence for this was provided in Runx2 knockout studies, as no osteoblasts were present in the knockout specimens<sup>23,24</sup>. The proliferation phase of mesenchymal stem cells is induced by the accumulation of Runx2 and Col1A1<sup>20</sup>. During this phase, the cells accumulate alkaline phosphatase, denoting the transition from mesenchymal stem cells to pre-osteoblasts. The signal of a mature osteoblast is the accrual of osterix and collagen type 1. Osteocytes and bone lining cells are terminally differentiated osteoblasts after the remodeling in that region has finished.

Osteoclasts are derived from mononuclear hematopoietic stem cells. The maturation and differentiation of osteoclasts are primarily controlled by macrophage colony-stimulating factor and RANKL, which are produced by osteoblasts, osteocytes, and bone lining cells. The M-CSF promotes differentiation and inhibits apoptosis, while RANKL is essential for inducing osteoclast formation. All three prominent bone cells have critical regulatory controls over each other to control their expression. One of the most critical control mechanisms is the RANKL/OPG signaling pathway.

Pre-osteoclasts and mature osteoclasts express the receptor activator for nuclear kappa-B (RANK) receptor extracellularly. This receptor binds its ligand (RANKL) and induces osteoclast differentiation and formation (**Figure 1.2**). The exact downstream mechanism has yet to be elucidated. However, several pathways have been determined to be involved, including TNF receptor-associated factors (TRAF), inhibitors of NF-kappa $\beta$  kinase (IKK), c-Jun N-Terminal Kinase (JNK), c-myc, p38, and NFATc1. Osteoblasts, osteocytes, and bone lining cells express RANKL and act as positive regulators of osteoclasts. However, studies have shown that osteocytes are the primary source of RANKL<sup>25,26</sup>. A study by Xiong and colleagues (2011) discovered that selectively knocking out osteocyte expression of RANKL reduced osteoclast numbers by 70%, suggesting the importance of osteocyte and local expression of RANKL. Additionally, Osteoblasts and BLCs can release OPG. It is a decoy receptor that binds RANKL, preventing it from binding to RANK receptors and inhibiting osteoclast activity (**Figure 1.2**). The absence of OPG leads to uncontrolled osteoclast activity. This pathway is further modulated by other systems (e.g., hypothalamic-pituitary-gonadal axis), hormone messengers (e.g., parathyroid hormone, estradiol,

testosterone), and local factors (e.g., TNF- $\alpha$ , BMPs, IL-1, IL-6, IL-11). The hypothalamic-pituitary-gonadal axis controls serum sex hormones that modifies osteoclast activity.



**Figure 1.2.** Opioids have two distinct direct and indirect ways of modulating osteoblast function. Normally, the hypothalamus releases gonadotropin releasing hormone (GnRH) that stimulates the pituitary to release follicle stimulating hormone and luteinizing hormone. Specifically, the luteinizing hormone increases the production of sex hormones (female – estradiol; male – testosterone). In males, aromatase converts testosterone to estradiol. Osteoblasts and osteocytes can control osteoclast production through the release of RANKL which binds to the osteoclast RANK receptor to induce maturation. Osteoblasts can further regulate this process through the release of decoy receptors (OPG) which bind RANKL and prevent it from binding to osteoclasts.

Estradiol regulates this pathway by increasing the release of OPG and decreasing the release of RANKL. When opioids are introduced, they reduce the release of GnRH resulting in decreased serum estradiol and increased osteoclast activity. Additionally, opioids bind directly to osteoblast inhibiting their bone-formation activities. This figure was created in BioRender and was adapted from Ming et al. 2020<sup>27</sup> and Seyfried et al 2012<sup>28</sup>.

## **1.5 Bone extracellular matrix**

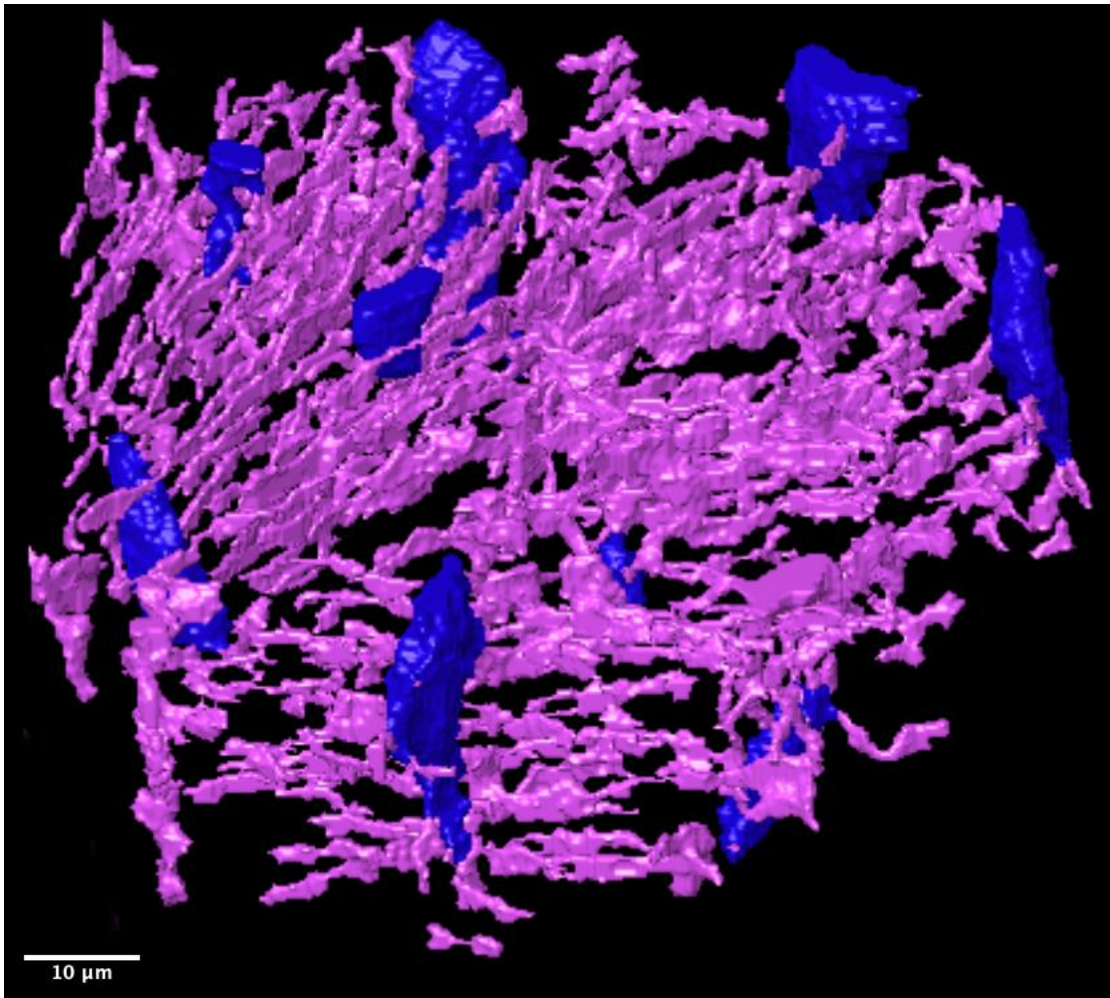
At the submicron level, hydroxyapatite comprises 65% of bone<sup>10</sup>. The rest of submicron bone is composed of collagen (25%) and water (10%)<sup>6,29</sup>. Hydroxyapatite is composed of calcium, phosphate, and hydroxyl groups and is primarily responsible for the strength and stiffness of bones<sup>30</sup>. However, hydroxyapatite is a brittle material unsuitable for the natural human condition alone. Collagen is a compliant material allowing deformation to occur before breaking under mechanical loads<sup>31</sup>. The balance of hydroxyapatite and collagen is delicate and contributes significantly to bone's mechanical properties. Previous studies have shown that highly mineralized bone is exceptionally stiff and brittle, whereas their less mineralized counterparts are more plastic<sup>31</sup>. They illustrate the delicate balance of bone composition and the importance of regulating it to achieve peak mechanical performance. Imbalance in this composition can lead to skeletal diseases.

One example of a skeletal disease from the imbalance of hydroxyapatite collagen is rickets. This disease is typically present in children. It is caused by low vitamin D, calcium, and/or phosphorous leading to weak bones<sup>32</sup>. Calcium and phosphorous are critical components to hydroxyapatite which is needed for strength. Osteogenesis imperfecta is another example of a skeletal disease impacting the balance of collagen and hydroxyapatite. This is a genetic disorder that impacts the ability to make type 1 collagen resulting in deficient and not enough collagen<sup>33</sup>. This disease is often referred to as brittle bone disease because the bones fracture more easily.

## 1.6 The lacuno-canalicular network

Throughout all types of bone is an extensive network that monitors bone health and coordinates an appropriate response to external stimuli. The network is called the lacuno-canalicular network (LCN) (**Figure 1.3**) and it connects the periosteal and endosteal surfaces together. As the name suggests, this network is composed of lacunae and canaliculi. Each osteocyte has 40-100 dendritic-like projections extending into the fluid-filled channels (canaliculi) and connecting via gap junctions<sup>21,25</sup>. Osteocytes have shown the ability to alter the length of their projections retroactively. The fluid contains nourishment for the osteocytes, and the canaliculi act as channels for the osteocytes to communicate with each other via pressure changes and signaling molecules. In addition to osteocytes, bone lining cells (BLCs) that line the periosteal and endosteal surfaces of bone are proposed to coordinate a process of bone renewal in conjunction with osteocytes<sup>34</sup>.





**Figure 1.3.** Confocal laser scanning microscopy image stack of the lacuno-canalicular network. Osteocytes reside in the lacunae (blue) and are interconnected with each other via fluid-filled canaliculi (pink). The lacunae are ellipsoid in nature and their associated canaliculi are thin channels. This network is the current theory for osteocyte communication. This figure was used with permission from Dr. Andronowski.

## 1.7 Basic multicellular units and skeletal remodeling

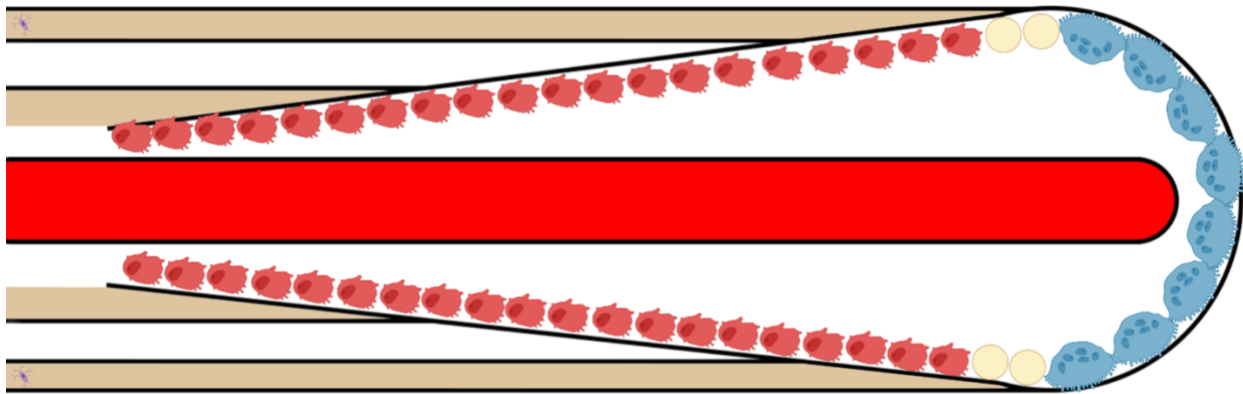
This extensive network can facilitate a highly coordinated process to repair bone in response to mechanical stressors or spontaneous remodeling events. Osteocytes act as mechanotransducers, translating the mechanical signals from dynamic changes in the canalicular fluid (e.g., microcrack) to chemical ones. Under significant mechanical loading, nitric oxide, adenosine triphosphate, and prostaglandins are released and are critical to signaling an appropriate response<sup>21</sup>. This process, typically referred to as the activation, resorption, and formation (ARF) sequence<sup>20</sup> can be further expanded into the activation, resorption, reversal, formation, mineralization, and quiescence (ARRFMQ)<sup>35,36</sup>. The ARRFMQ sequence is primarily spearheaded by the basic multicellular unit (BMU), which is composed of osteoclasts and osteoblasts.

Osteocytes and BLCs coordinate the remodeling process by recruiting BMUs in the activation phase through the release of osteopontin. Specifically, hematopoietic stem cells are recruited to the area where the expression of macrophage colony-stimulating factor (M-CSF) and receptor activator for nuclear factor kappa-B ligand (RANKL) initiate the differentiation and proliferation of osteoclasts<sup>25,26</sup>. Originally, apoptotic osteocytes were thought to be the primary signal, however, neighboring osteocytes have been shown to express a higher RANKL/OPG ratio comparatively<sup>21</sup>. The tip of the BMU, referred to as the cutting cone, is composed of osteoclasts resorbing old bone tissue away in the resorption phase. The osteoclasts form a seal around the bone using actin-rich podosomes, creating a ruffled area for increased surface contact, and they secrete cathepsin K and hydrochloric acid into the sealed space around the bone<sup>37,38</sup>. The acidic environment forces the dissolution of the old bone, and a large canal is produced. The edge of the canal is referred to as the reversal line (or cement line) and signifies the edge of the osteon. A typical resorptive event

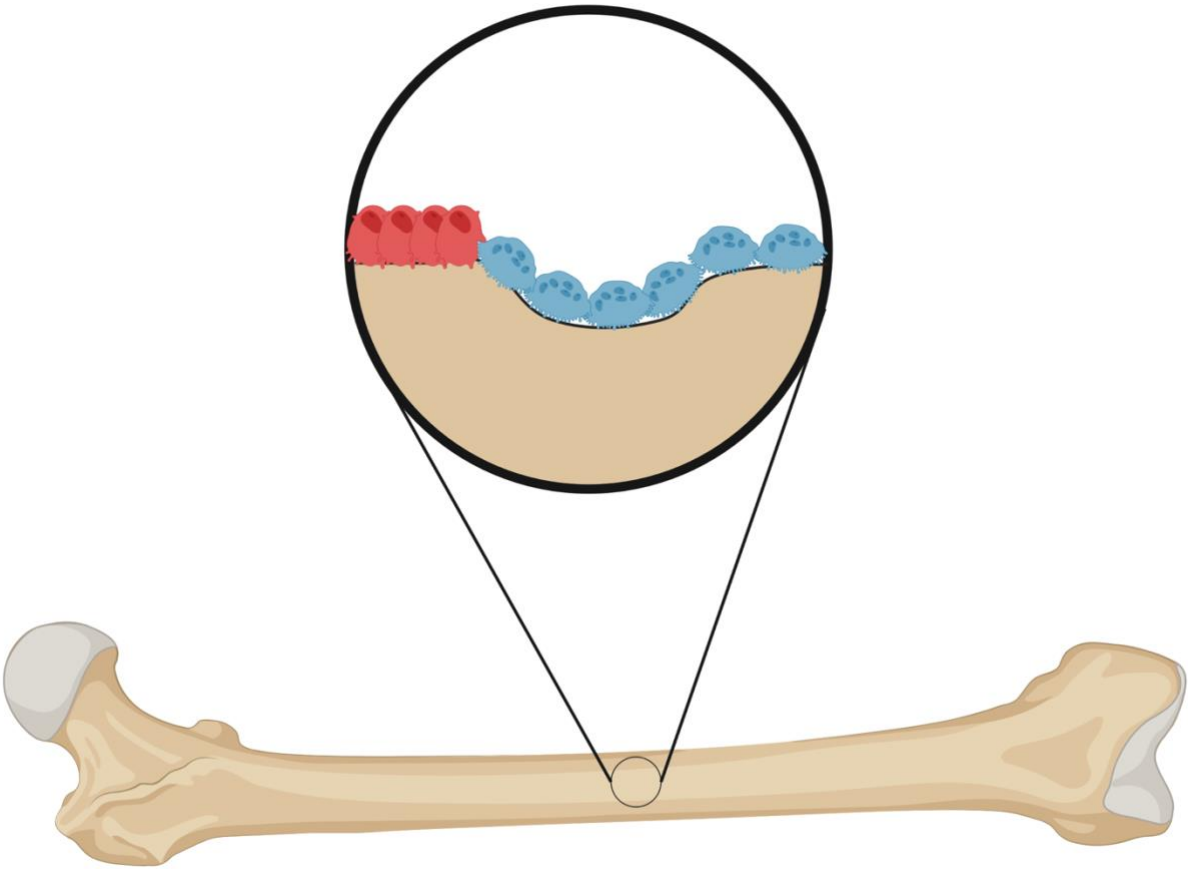
will create a resorptive bay between 200-300  $\mu\text{m}^5$ . Additionally, studies have shown that osteoclasts engulf and remove the apoptotic osteocytes<sup>3,20,39</sup>. During the reversal phase, mononuclear cells smooth out the canal in preparation for formation, specifically the deposition of the reversal (or cement) line.

Osteoblasts adhere to the reversal line and deposit osteoid, a soft bone matrix absent of hydroxyapatite, during the formation phase. The osteoid is laid down in concentric layers, forming individual lamellae. The constriction of the canal in formation gives a traditional BMU a cone-shaped appearance, often termed the osteoblastic closing cone<sup>36</sup>. At a certain point, closing ceases, leaving behind a Haversian canal permeated by blood vessels. Some osteoblasts become entombed when laying down the bone matrix. Osteoblasts secrete hydroxyapatite to mineralize the surrounding bone tissue in the mineralization phase<sup>5</sup>. This mineralization phase occurs in two stages: vesicular and fibrillar. Small vesicles (30 – 200 nm) are released from the osteoblasts into the surrounding osteoid during the vesicular phase. The osteoid immobilizes the vesicles, and during the fibrillar phase, the vesicles rupture, expelling the hydroxyapatite crystals<sup>20</sup>. The entrapped osteoblasts transition to immature osteocytes and begin extending projections to create communication channels with the surrounding osteocytes, thus forming the LCN. The decreased production of osteocalcin, collagen type 1, and alkaline phosphatase, along with the upregulation of dentin matrix protein and sclerostin, indicate a mature osteocyte<sup>20,21</sup>. The quiescence phase is marked by the transition from mature osteoblasts to mature osteocytes. However, not all osteoblasts transition to osteocytes. The rest either differentiate into BLCs or undergo apoptosis<sup>31</sup>. After approximately 120 days, the remodeling process is completed through one transverse cross-section in human cortical bone<sup>5</sup>. In one year, about 10% of the skeleton has been remodeled<sup>9</sup>.

Inside the bone matrix (intracortical), BMUs tunnel through the tissue (**Figure 1.4**). Bone on the periosteal and endosteal surfaces is also remodeled in a highly coordinated manner, however, it does not involve tunneling. Osteoclasts dig trenches, removing old bone, and osteoblasts fill the trenches with new bone (**Figure 1.5**). Lining the endosteal and periosteal surfaces of the bone are BLCs that can physically resist osteoclast activity. Additionally, BLCs can release osteoprotegerin (OPG) and RANKL to inhibit or induce osteoclast activity. Dysregulation of the bone remodeling system can lead to an imbalance of resorption and formation. While this imbalance typically favors resorption, leading to pathological conditions such as osteoporosis<sup>25</sup>, there are cases where formation predominates over resorption, such as osteopetrosis<sup>20</sup>. Understanding the cells that contribute to bone microstructure, their origin and function, is integral in furthering the foundational knowledge of various bone-related pathologies.



**Figure 1.4.** A BMU remodeling intracortical bone. The rounded aspect of the BMU is composed of osteoclasts (blue) that resorb away old bone. Mononuclear cells (yellow) smooth out the edge of the resorption bay to prepare it for the osteoblasts (red) that infill bone lamellae concentrically. During this process, some osteoblasts become encased in the bone matrix and transition into osteocytes (purple). The central Haversian canal remains unfilled and supplies nutrients through blood vessels to the surrounding cells (osteocytes, osteoblasts, osteoclasts, and mononuclear cells). This figure was created in BioRender.



**Figure 1.5.** Periosteal bone remodeling differs from intracortical remodeling in the appearance of the BMU. Osteoclasts (blue) resorb a crater of existing bone that is replaced with new bone by the osteoblasts (red). This figure was created in BioRender.

The LCN is a comprehensive, interconnected osteocyte system that permeates all bone structures. Its coordination BMUs and skeletal remodeling is inextricably linked to normal bone function, and its impairment is related to debilitating disease processes. This makes understanding this network crucial in developing proper treatments for common diseases. Osteoporosis is one such disease that may be treated with an increased understanding of the LCN. Another important consideration is the additional factors that potentially contribute to disease progression. Factors impacting the LCN and overall bone quality are diet, exercise, alcohol, tobacco, opioids, etc. The crux of this research project is determining the impact opioids may have on cortical bone microstructure and its impairment of the LCN, leading to debilitating conditions such as osteoporosis.

## **1.8 Osteoporosis**

One of the most debilitating bone diseases is osteoporosis, which afflicts 200 million people worldwide<sup>40</sup>. Canada is no exception, with two million people suffering from osteoporosis. Further, it is estimated that one in every three females and one in every five males will suffer from a fracture directly related to osteoporosis in their lifetime<sup>41</sup>. Hip fractures are exceptionally debilitating, as only 33% of older females can return to independent living, and 30% of patients require at-home nurses<sup>40</sup>. Annually, there are ~ 250,000 osteoporotic-related hip fractures with a 20% mortality rate<sup>40</sup>. The preference towards older females is attributed to menopausal bone loss<sup>1</sup>. This disease affects millions daily and immensely impacts public health<sup>42</sup>. Its global effect is set to increase as the World Health Organization (WHO) predicts 2.1 billion people at least 60 years old within the next 35 years<sup>43</sup>. The most common treatment for osteoporosis is the administration of bisphosphonates, however, it can have adverse side effects<sup>40</sup>.

Osteoporosis is caused by the uncoupling of resorption and formation involved in routine bone maintenance and is influenced by many risk factors (e.g., diet, activity level, hormones, etc.). The criteria for diagnosing osteoporosis as defined by the WHO is the comparison of the bone mineral density (BMD) of a patient to the BMD of a young, healthy adult female with a difference of 2.5 standard deviations being a positive diagnosis for osteoporosis<sup>44</sup>. Most measures rely on areal BMD provided by dual X-ray absorptiometry (DXA) and analysis of sites composed predominantly of trabecular bone (e.g., vertebrae). However, the human skeleton is almost entirely composed of cortical bone (~80%)<sup>9,45</sup>, and most appendicular bone loss is cortical. Cortical bone remains understudied even though it substantially deteriorates in the aging skeleton. This underpins a need for additional research studying cortical bone. Previously, this was due to imaging resolution's incapability of analyzing cortical bone microstructure<sup>46</sup>. Further, the diagnosis relies on the appearance of macroscopic structures. Still, the cellular system that controls the formation and resorption of bone lies at the microscopic level and may be necessary for increasing our foundational knowledge of the progression of this disease and possible targets for pharmaceutical intervention.

## **1.9 Current and projected trends in opioid usage**

Today, opioid use is increasing in prevalence and affecting millions worldwide. The World Health Organization estimated 62 million opioid users (1.22%) globally and 11.79 million (3.63%) in North America, representing the largest continent for opioid use in 2019<sup>47</sup>. In this report, opioids were the most concerning drug reported as they estimated that more than 70 percent of 18 million years of life lost were due to opioid use<sup>47</sup>. Further, they project an 11 percent increase in opioid



users by 2030, emphasizing that opioid use is not decreasing, especially in low and middle-income countries<sup>47</sup>.

Fentanyl, an opiate, is considered the most commonly used intraoperative analgesic in North America, South America, Europe, and parts of Africa and Asia<sup>48-50</sup>. There were 9,327 opioid-related hospitalizations in Canada in 2017<sup>51</sup>. One in eight people were prescribed opioids in 2018 alone<sup>52</sup>. Prescription opioid use is currently in decline in terms of starting/continuing prescriptions, dosages, and duration of opioid treatment<sup>52</sup>. However, it is still considered the gold standard in managing chronic pain<sup>53</sup>. This general trend is encouraging; however, it is not indicative of the entire narrative. Illicit opioids are increasingly available because they are cheap to manufacture and highly addictive<sup>54</sup>, and people are turning to this resource to supplement their opioid addiction. The consequences can be dire with seventy-eight percent of opioid-related deaths attributed to illicit fentanyl use in 2019<sup>55</sup>. Death statistics related to opioid use fluctuated in recent years until 2020 in Canada. There were 6,638 deaths, a 180% increase in deaths from 2019. A further increase in deaths was reported in 2021, with 7,902 deaths related to the narcotic<sup>56</sup>. This staggering increase is potentially linked to the global COVID-19 pandemic. The Public Health Agency of Canada (PHAC) used mathematical modeling to predict the number of opioid-related deaths in each quarter of 2022. In their model, there are two variables: 1) healthcare prevention of deaths (30 percent) and 2) availability of fentanyl. If healthcare interventions continue to prevent the same number of deaths (30%), mortality will continue to rise regardless of the fentanyl supply changing. If healthcare prevents more deaths (50%) and the fentanyl supply increases, opioid-related deaths will plateau and remain consistent with previous years. If healthcare prevents more deaths (50%) and the fentanyl supply remains the same, opioid-related deaths will decrease<sup>57</sup>.

The global COVID-19 pandemic, combined with government measures to curb the spread of infection, resulted in increased stress, isolation, and boredom. These factors have impacted people's choices and consumption of narcotics. Prescription drug shortages caused people to turn to illicit substances (e.g., heroin and fentanyl) as a supplement. There was a global increase in pharmaceutical opioid consumption of 25 percent, and the United States reported an increase in the use of heroin and fentanyl<sup>47</sup>. Additionally, opioids are consistently ranked as one of the main reasons for receiving addiction treatment, especially in Europe, North America, and Asia. Treatment for opioid addiction accounted for 57 percent of all European drug treatments<sup>47</sup>. The opioid epidemic has only worsened in the wake of the COVID-19 pandemic.

Opioids have widespread use, legally and illegally, in Canada and similarly have widespread health consequences. Side effects of opioids include dizziness, cognitive impairment, nausea, vomiting, respiratory depression, and overdose. Illicit opioid use and needle-sharing have caused the spread of HIV and hepatitis, unintended but often deadly consequences of opioid use<sup>47</sup>. Opioids can indirectly impact the skeletal system by altering an individual's mental faculties with sedative effects, increasing the risk of falls and fall-related fractures. Additionally, opioids can impact the skeletal system by altering osteoblast and osteoclast production. They can further dysregulate normal bone maintenance by affecting societal conditions (e.g., malnutrition) and contributing to disease and organ failure development and progression.

### 1.10 Opioids' influence on bone health

Opioids have negative direct and indirect effects on skeletal health. The direct impact on the skeletal system is through opioid receptors on osteoblasts. Osteoblasts canonically have three opiate receptors: mu, kappa, and delta. The more potent opiates (e.g., morphine, heroin, fentanyl) are all mu receptor agonists. Research on the effects of Kappa opioid receptors (KOR) and delta opioid receptor (DOR) agonists remains largely vacant<sup>58</sup>. Mu receptor agonists correspond with decreased serum calcium and estradiol and increased osteocalcin and alkaline phosphatase<sup>59</sup>. Increased osteocalcin and alkaline phosphatase are indicators of increased bone turnover, which are commonly elevated in diseases like osteoporosis. Boshra (2011) found an increase in osteopontin, a hematopoietic stem cell recruiter, corresponding to increased osteoclast activity and bone turnover. *In vitro* studies also indicate reduced osteoblast activity<sup>59,60</sup>. A new opioid receptor, the opioid growth factor receptor (OGFR), has recently been discovered and described<sup>60,61</sup>. Thakur et al. (2016) and Tanaka et al. (2019) show evidence of increased OGFR expression over the canonical opioid receptors. Blockage of OGFR resulted in decreased osteoblast proliferation but, interestingly, did not significantly affect differentiation<sup>60</sup>. Additionally, Thakur and colleagues (2016) described increased OGFR expression during differentiation. Naloxone, an opioid antagonist, only affects mesenchymal stem cells or osteoblasts if an opioid growth factor receptor is present, underlining the importance of OGFR<sup>61</sup>.

Opioids, especially mu receptor agonists, influence the hypothalamic-pituitary-gonadal (HPG) and hypothalamic-pituitary-adrenal (HPA) axes (**Figure 1.2**). They prevent the release of gonadotropin-releasing hormone from the hypothalamus, which reduces follicle-stimulating hormone and luteinizing hormone secretion from the pituitary gland. Ultimately, the production of

estradiol and testosterone is severely reduced. As described in **Figure 1.2** estradiol is crucial in modulating the OPG/RANKL/RANK pathway and further inhibits interleukin-1, 6 and tumor necrosis factor- $\alpha$  preventing osteoclastic activity<sup>59</sup>. The reduction in serum sex steroids is more pronounced in males. Coluzzi et al. (2015) reported androgen levels in males reached near castration levels. Opioid-induced androgen deficiency (OPIAD) affects many males prescribed an opioid to manage chronic pain<sup>53</sup>. This is an important phenomenon because testosterone is converted to estradiol in males via the enzyme, aromatase. Reduction in serum estradiol leads to increase bone turnover.

Long-term opioid use has also been linked to malnutrition. In a study analyzing the nutritional patterns of patients with long-term opioid usage, the authors found a substantial decrease in average caloric consumption from normal individuals as determined by the US Department of Health and Human Services<sup>62,63</sup>. Additionally, they noted decreased intake of vitamins D and E and magnesium<sup>62,63</sup>. Opioids can disrupt microbial diversity, cholesterol/bile metabolism, and the mucosal barrier, reducing intestinal immunity against gut pathogens<sup>64</sup> and leading to increased pathogenesis and sepsis<sup>65</sup>. They further dysregulate intestinal health by decreasing gut motility, contributing to constipation in patients<sup>63,66</sup>. Reduced intestinal calcium absorption is compensated for by bone resorption. This increased resorption leads to more fragile and brittle bones.

Additionally, opioids are proposed to reduce bone health in patients partially due to their sedative effects<sup>67</sup>. Dizziness is a side effect associated with the use of opioids, as they directly impair the central nervous system. The dizziness increases the risk of falls, ultimately contributing to fall-related fractures. Altogether, the direct and indirect consequences of prolonged opioid use cause a

maelstrom of complications to the skeletal system. Several studies have demonstrated the use of opioids causes prolonged recovery times after orthopedic surgeries<sup>53,68</sup>.

### **1.11 Quantification of cortical bone morphology**

For centuries, bone researchers communicated using terminology unknown and confusing to those outside the field. In 1987, Parfitt proposed a unified list of relevant bone nomenclature (**Table 1.1**) to standardize the field and make it more accessible. This widely accepted nomenclature has been modified and incorporated into imaging analysis programs since its inception<sup>69,70</sup>. BoneJ, a plugin for ImageJ<sup>71</sup>, uses the ASBMR nomenclature when extracting data related to cross-sectional geometry. Similarly, the imaging software CTAn v. 1.18.8.0 (Bruker, Billerica, United States of America) can characterize and quantify cross-sectional parameters of whole bone or cortical and trabecular bone from laboratory  $\mu$ CT. Cooper and colleagues (2003) converted CTAn's parameters for trabecular bone to apply to SR $\mu$ CT images of cortical bone for analysis of vascular pores and osteocyte lacunae (**Table 1.2**).

**Table 1.1.** Standard nomenclature for bone, bone cells, and morphological parameters

<b>Abbreviation</b>	<b>Meaning</b>
Ct	Cortical bone
BS	Bone surface
BV	Bone volume
TV	Tissue volume
Ca	Canal/canalicula/canlicular
Po	Pore/porous/porosity
Lc	Lacuna/lacunar
Dm	Diameter
Dn	Density
Th	Thickness
BMU	Basic multicellular unit
Ca.V	Canal volume
Ca.Ar	Canal area
Ct.Th	Cortical thickness
BV/TV	Bone volume (%)
BS/TV	Bone surface (mm <sup>2</sup> /mm <sup>3</sup> )
Ct.Po	Cortical porosity
Ct.Th	Cortical thickness

\*Modified from Parfitt et al. 1987 and Dempster et al. 2013.

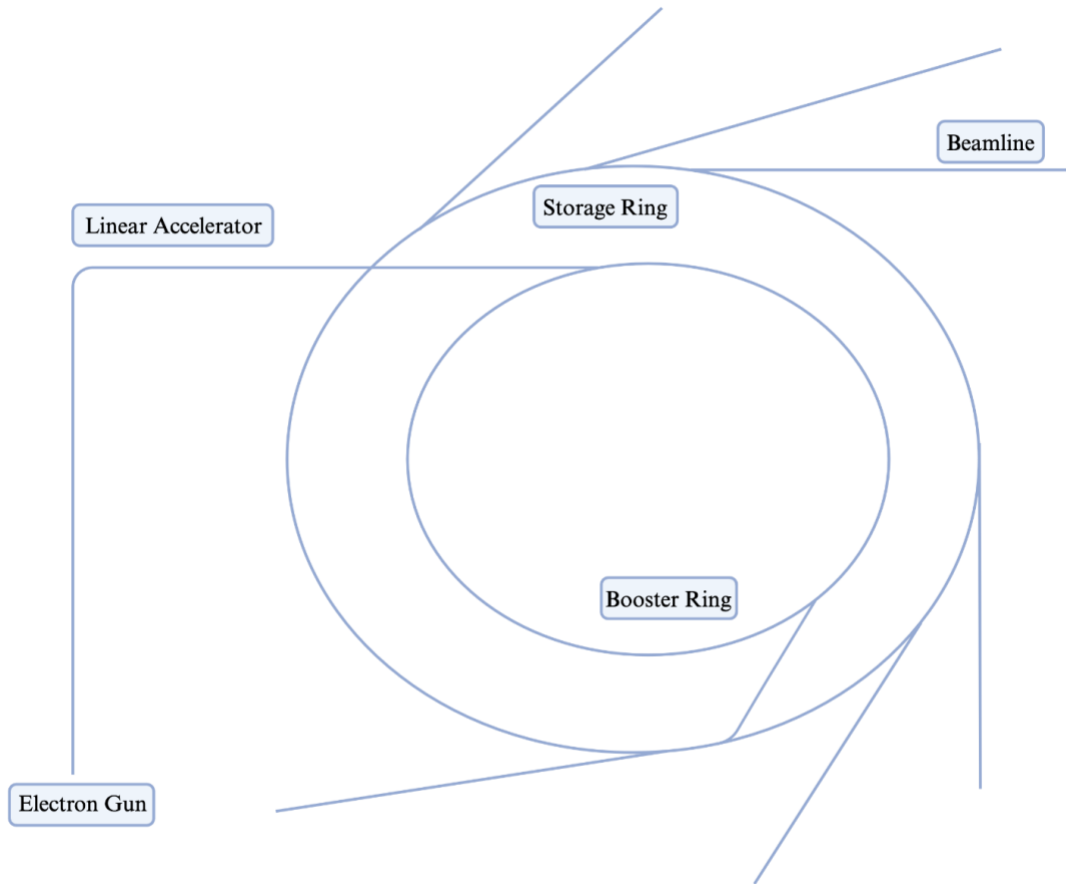
**Table 1.2.** CTAn terminology for  $\mu$ CT of trabecular bone and its conversion for SR $\mu$ CT cortical bone

<b>CTAn term</b>	<b>Translation for pores</b>	<b>Translation for lacunae</b>
Bone volume	Pore volume	Lacunar volume
Bone surface	Pore surface	Lacunar surface
Bone volume fraction	Cortical Porosity	-
Bone surface-to-tissue volume	Pore surface-to-tissue volume	Lacunar surface to tissue volume
Trabecular thickness	Pore diameter	Lacunar diameter
Trabecular separation	Pore separation	Lacunar separation

\*Modified from Cooper et al. 2003.

## 1.12 Synchrotron Radiation Micro-Computed Tomography

Desktop micro-computed tomography ( $\mu$ CT) machines lack the ability to acquire 3D datasets at  $1.5\ \mu\text{m}$ , the resolution required to reveal osteocyte lacunae. Thus, researchers are turning to synchrotron radiation micro-computed tomography (SR $\mu$ CT). Synchrotron imaging facilities are particle accelerators that produce brilliant braking radiation (bremsstrahlung) to achieve imaging resolutions and subsequent 3D datasets that are otherwise impossible without further tradeoffs (e.g., increased imaging time). Heated tungsten oxide serves as the electron producer for the system (**Figure 1.6**). The released electrons travel to the linear accelerator, which uses radio waves to energize the electrons to move near the speed of light<sup>72</sup>. Afterward, they enter the booster ring, where microwave fields raise the electrons' energy from 250 MeV to 2,900 MeV<sup>73</sup>. Finally, the electrons enter the storage ring surrounded by magnets that force the electrons to move around the ring<sup>74</sup> and the ring is kept at  $-270^\circ\text{C}$  to reduce excess power loss. This causes the electrons to give off energy accepted by the beamlines for imaging. Electron density in the ring gradually declines over time; thus, new electrons are constantly introduced to maintain the current. The synchrotron facility creates monochromatic light, allowing for higher spatial resolution than the polychromatic light of laboratory micro-computed tomography<sup>72</sup>.



**Figure 1.6.** A diagram of a typical third generation synchrotron facility. The electron gun encourages the release of electrons that are accelerated near the speed of light by the linear accelerator. Afterwards, the electrons move into the booster ring. A radiofrequency cavity inside the booster ring energizes the electrons to a desired energy level. This varies based on the facility, but usually ranges from 1 – 8 GeV. The electrons then travel to the storage ring where they reside for hours. Charged electrons want to travel in a straight line so large magnets are used to force the electrons around the ring. During that bend, energy is released by the electrons, this is referred to as synchrotron radiation. The radiation is accepted by the beamlines where they are modified to the researchers' experimental parameters. Specialized magnets exist in the booster ring that modify the electrons to produce higher intensity light. This figure was created in BioRender.

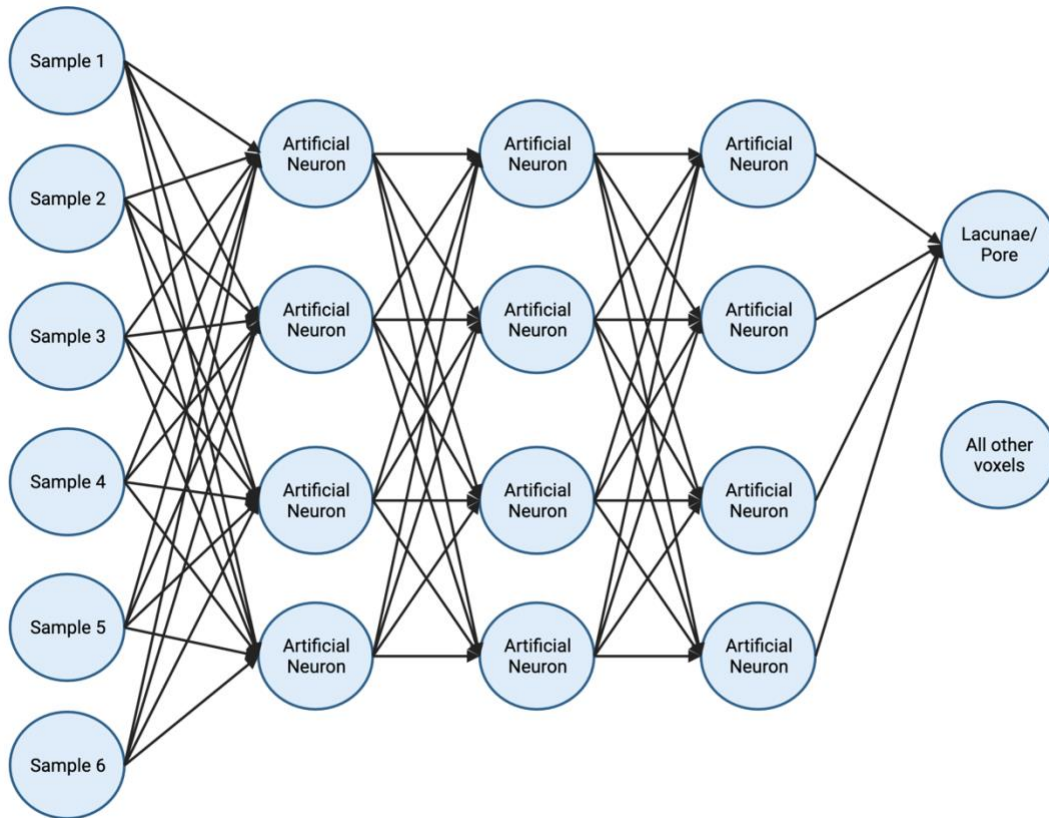


The Canadian Light Source (CLS) facility was first opened on December 9, 2003<sup>75</sup>, but the BioMedical and Imaging Therapy Bend Magnet (BMIT-BM) beamline would not open until 2011<sup>76</sup>. The purpose of the BMIT beamline is research in medicine, agriculture, and other biomedical sciences, with specific focus areas on respiratory, bone, tissue, and scaffold imaging<sup>76-79</sup>. SR $\mu$ CT has the unprecedented ability to non-destructively visualize osteocytes in 3D owing to its resolution capabilities of 0.5-10 $\mu$ m<sup>72,80</sup> and contributed to the revolutionary discovery of osteocyte function in bone<sup>21</sup>. Furthermore, SR $\mu$ CT has frequently been utilized to study lacunar and pore morphometry in connection with normal bone maintenance, aging, and disease<sup>2,81-87</sup> making this system an appropriate imaging technique for the analysis of lacunae and pores. At CLS, 22 beamlines produce different spectral ranges for various imaging modalities. This experiment necessitated using the BMIT-BM for SR $\mu$ CT. Further, the BM beamline has phase contrast potential.

### 1.13 Deep learning

Artificial intelligence is (AI) a broad categorization for the science of implementing computers to perform actions without human input. One subsection of AI is machine learning which implements computer algorithms and models to complete tasks. A novel subsection of machine learning has emerged as deep learning. The general principle of deep learning is to teach a computer to apply algorithms adaptively to complete tasks. Theoretically, this should allow deep learning to complete tasks too complicated for traditional machine learning algorithms. To accomplish this deep learning uses a multi-layered approach with at least three layers<sup>88</sup>. Each layer consists of several 'neurons' that together form a neural network. The design was based on biological neurons that learn to complete distinct tasks (**Figure 1.7**). A convolutional neural network is a type of neural

network that was developed to enhance image visualization and segmentation. A convolutional translation is applied at each layer and then passed down to the next layer. The convolution converts a cluster of neighboring pixels into a single number. This occurs until the computer has scanned the entire image. The resulting group of numbers is passed down to subsequent layers for further convolutions. Typically, the earlier layers focus on simple pattern recognition of shapes and edges. Deeper layers focus on more complex patterns using more sophisticated filters for complete processes such as full animal detection.



**Figure 1.7.** A typical example of a multilayered neural network. This is the most basic neural network architecture where each layer is composed of artificial neurons that learn from the image and pass their output to the next layer. Each layer learns different distinct features starting with basic structures (e.g., circles) to more complicated structures (e.g., hand). This figure was created in BioRender.

Several different architectures exist for convolutional neural networks, such as U-Net and MA-Net that apply different algorithms to learn and segment images. U-Net was groundbreaking by introducing a U-shaped architecture<sup>89</sup>. This architecture has been extensively tested on multiple biological specimens, achieving exceptional segmentation results on all tests<sup>89,90</sup>. Since its inception, the U-Net model architecture has been modified to improve its image segmentation capabilities in new models: wide U-Net and U-Net++.

U-Net++ has several advantages over its predecessor, including skip connections with dense convolutional layers and deep supervision<sup>91</sup>. The original U-Net architecture has a simple encoder backbone followed by a decoder sub-network<sup>89</sup>. The skip connections with heavy convolutional layers allow for improved recovery of fine details. Before each skip layer, a concatenation layer combines the previous convolutional layers with a corresponding up-sampled output<sup>91</sup>. The layer receives a concatenated input, applies a convolutional transformation to the data, and outputs it to the next<sup>91</sup>. The deep supervision, introduced in U-Net++, has two modes: accuracy and speed. The accurate mode averages all outputs of all segmentations, and the fast mode is only from segmentation branches to determine speed gain and model pruning. These improvements have significantly advanced image segmentation in medicine over its predecessors.

Deep learning has been applied extensively to the medical field, including automated image analysis of bone<sup>92-95</sup>. A common task in the medical field is assessing bone age from radiographs<sup>92,93,96,97</sup>. Previous manual techniques apply the use of Greulich and Pyle or the more accurate Tanner Whitehouse atlases, which are time-intensive determinations. Thus, deep learning

has been applied to circumvent the time-intensive procedure with a more efficient alternative. Generally, deep learning models have been demonstrated to outperform radiology residents and less experienced practitioners, and results are comparable to radiologists with more than ten years of experience<sup>92,93,96,97</sup>. In one study, the deep learning model outperformed all reviewers when grouped, but excluding the pediatric endocrinologist significantly improved the reviewers' results<sup>93</sup>. The authors concluded that this is possibly a result of real-time bone age assessment, further supporting deep learning given the time constraints of working in an outpatient clinic<sup>93</sup>. The use of deep learning has been further applied to the identification and labeling of bone tumors on radiographs. In both studies, the models outperformed radiology residents and junior radiologists but were comparable to experienced senior radiologists<sup>98,99</sup>.

#### **1.14 Research Objectives:**

The objectives of this research are to 1) apply deep learning architectures to SR $\mu$ CT data from human rib bone specimens with known demographics, 2) compare it to the existing standard for high-resolution bone data segmentation, and 3) characterize potential effects of opioid use on bone microstructure. Hypotheses include:

1. U-Net++ architecture will more accurately segment SR $\mu$ CT data of bone than the current standards (CTAn, Bruker) for data processing, and
2. Prolonged opioid exposure will dysregulate the bone remodeling process represented by increased cortical porosity, pore convergence, and pore diameter and reductions in osteocyte lacunar number, density, volume, and diameter.

## 2. Materials and Methods

To test the hypothesis of opioid-induced dysregulation of the bone remodeling process, 97 left-sixth midshaft human rib samples ( $n = 97$ ) were procured from organ donors through a contract with a non-profit organ procurement organization (OPO) (Lifebanc, Cleveland, United States of America) that obtained informed consent from the donors or their next-of-kin. The research was approved by Newfoundland and Labrador Health Research Ethics Board (Protocol Reference #2020.308, **Appendix 7.1**). The study cohort comprised nearly 38% female (37) and 62% male (60) donors. Similarly, there was almost an even distribution among opioid abuse (47) and controls (50). The cases were divided into opioid users and controls based on their reported health history (**Table 2.1**). Individuals were selected between the ages of 20 and 60 to avoid modeling events in younger growing individuals and age-associated degenerative changes in bone microstructure and hormonal changes resulting from menopause in older individuals. The OPO collected a detailed donor profile, including serology and toxicology reports, organ charts, past medical history, and a detailed questionnaire from the individual before death or the next of kin.

**Table 2.1.** Opioid use history for the experimental cohort.

Sample #	Sex	Age	Experimental Group	Notes Concerning Opioid Use
6	F	21	Control	-
1	F	28	Control	-
4	F	29	Control	-
92	F	32	Control	-
49	F	35	Control	-
97	F	35	Control	-
86	F	36	Control	-
31	F	38	Control	-
18	F	39	Control	-
19	F	39	Control	-
72	F	40	Control	-
93	F	43	Control	-
17	F	44	Control	-
47	F	47	Control	-
87	F	48	Control	-
25	F	49	Control	-
27	F	50	Control	-
65	F	53	Control	-
69	F	54	Control	-
12	F	55	Control	-
71	F	55	Control	-
39	F	56	Control	-
24	F	58	Control	-
85	M	20	Control	-
60	M	22	Control	-
38	M	23	Control	-
50	M	23	Control	-
41	M	24	Control	-
59	M	26	Control	-
48	M	29	Control	-
10	M	32	Control	-
15	M	34	Control	-
67	M	36	Control	-
68	M	36	Control	-
36	M	37	Control	-
22	M	38	Control	-
45	M	39	Control	-
7	M	40	Control	-

77	M	41	Control	-
43	M	43	Control	-
57	M	45	Control	-
21	M	46	Control	-
32	M	46	Control	-
52	M	48	Control	-
81	M	50	Control	-
23	M	51	Control	-
58	M	53	Control	-
80	M	53	Control	-
28	M	55	Control	-
35	M	56	Control	-
83	F	25	Opioid user	OD, heroin abuse
30	F	26	Opioid user	OD, prior ODs
29	F	28	Opioid user	OD, heroin, cocaine, benzos, marijuana abuse ~13 years
46	F	28	Opioid user	Polysubstance abuse
42	F	29	Opioid user	Opioid use disorder
62	F	32	Opioid user	Heroin use (7 years)
75	F	33	Opioid user	Drug abuse
66	F	39	Opioid user	Polysubstance use (fentanyl) for 2 years
89	F	40	Opioid user	Heroin and fentanyl abuse
13	F	43	Opioid user	Opioid use disorder
76	F	44	Opioid user	Crack cocaine, heroin abuse
11	F	49	Opioid user	Street opioid use for past year (suicide by benzos)
88	F	50	Opioid user	Heroin, fentanyl abuse
37	F	52	Opioid user	ODs
56	M	23	Opioid user	Heroin use (5 years)
26	M	25	Opioid user	Cocaine, meth, suspected synthetic opioid, THC use; IV opioid use
94	M	25	Opioid user	Heroin use for a while
79	M	27	Opioid user	Heroin (10 years), fentanyl (3-4 years)
95	M	28	Opioid user	Polysubstance abuse
3	M	29	Opioid user	OD (Tox + Fentanyl)
2	M	32	Opioid user	Positive toxicology of opiates, THC, amphetamines
5	M	32	Opioid user	OD, daily heroin use for 12 years)



40	M	35	Opioid user	Heroin use (5 years)
70	M	38	Opioid user	Heroin abuse
84	M	38	Opioid user	Drug abuse
96	M	38	Opioid user	Fentanyl for 2 years
61	M	39	Opioid user	OD (Heroin + fentanyl)
33	M	41	Opioid user	OD, 10-year history of heroin use
54	M	42	Opioid user	OD
73	M	43	Opioid user	Heroin use (3 years)
16	M	45	Opioid user	Methamphetamine use on and off for 30 years
55	M	45	Opioid user	Polysubstance use for 1 year
44	M	46	Opioid user	Heroin and fentanyl use for 8-15 years
14	M	47	Opioid user	Nothing listed
34	M	47	Opioid user	Polysubstance abuse
90	M	47	Opioid user	Drug OD (meth for 2 years)
78	M	48	Opioid user	Polysubstance abuse (heroin, meth, crack cocaine)
53	M	49	Opioid user	Opioid use for 2 years
64	M	50	Opioid user	Smoked methamphetamines daily
9	M	51	Opioid user	OD
8	M	52	Opioid user	History of polysubstance abuse
74	M	53	Opioid user	Polysubstance abuse
91	M	54	Opioid user	Heroin (~17-20 years)
51	M	56	Opioid user	Fentanyl use for 5 years
63	M	57	Opioid user	Opioid abuse (Heroin for 25 years)
20	M	58	Opioid user	Past cocaine use
82	M	58	Opioid user	Heroin, fentanyl abuse

\* The thickest bar indicates a split between opioid user and control. The two thicker bars indicate a split between male and female within the opioid use and control groups. The ‘-’ indicates no reported opioid use.

The ideal sampling site was the left sixth rib to eliminate the influence of mechanical loading on bone microstructural parameters. Mechanical load can vary amongst individuals and may be an indirect consequence of substance use. For example, a person with a more active lifestyle will have different bone microstructure in the femoral cortex compared to someone with a more sedentary lifestyle regardless of opioid use history. Additionally, during the 1960s left sixth ribs were routinely used for bone biopsy. This excess of sample material allows for comparisons to be made from the project. These two essential factors make the left sixth rib a suitable candidate for this study.

## **2.1 Sample Procurement**

Following the OPO's collection of vital organs for transport, Dr. Andronowski procured three-to-five-inch segments of the mid-shaft left sixth rib in the operating room for research purposes. Samples were wrapped in saline-soaked gauze, transported on ice, and subsequently stored in a negative -20°C freezer until further processing.

## **2.2 Sample Preparation**

In order to prepare the samples for imaging, the samples had to be stripped of soft tissue and fixed. The frozen samples were thawed in the refrigerator for 24 hours to accomplish this. All soft tissues were removed from the periosteal and endosteal borders following a protocol outlined by Crowder<sup>100</sup>. The samples were stripped of soft tissue by pulling on the soft tissues with a pair of tweezers. The soft tissue that remained adhered to the periosteal surface sample was removed with gentle scraping using a dental scraper (Catalog No. MERKQ0130JK, Antonki, Shenzhen, the People's Republic of China). The Endosteal (inner) surface of the bone was flushed using a water

flosser (ASIN: B0CC95VN4L, INSMART, Hanoi, The Socialist Republic of Viet Nam). Afterwards, the samples were fixed in 70% denatured ethanol to preserve the tissue<sup>101</sup>.

The field of view of our experimental setup is approximately four millimeters by five millimeters, which is far smaller than the procured samples. An Andronowski et al. (2020) initiative created a standardized protocol to create samples that are two millimeters by five millimeters to fit the field of view and account for some lateral movement of the sample during rotation<sup>102</sup>. Some modifications have been made to the original procedure. Briefly, a five-millimeter section was removed using an Isomet 1000 (Buelher, Catalog No. 11-2180, Lake Bluff, United States of America) equipped with a diamond-tipped wafering blade. The rib was gently secured to a chuck and lowered onto the blade, spinning at 100 rotations per minute. A small section of bone was initially removed to produce a smooth surface for mounting. Then the five-millimeter section was procured by adjusting the blade 5.5 millimeters to account for the thickness of the blade. At this stage, the sample has the appropriate height but is still too wide for the experimental setup. To acquire a sample of the proper width, the sample is adhered to an aluminum tin via thermal epoxy resin (CrystalBond™, Electron Microscopy Sciences, Catalog No. 50400-01, Hatfield, United States of America) and cored with a three-millimeter diamond-tipped bench drill press (Proxxon, Catalog No. 38-128, Hickory, United States of America). The sample is submerged in deionized water to prevent heat-associated damage to the sample. The resulting product is a cylindrical core with a two-millimeter diameter and a five-millimeter height. The cores are stored in a labeled micro-centrifuge tube for safe storage and transportation.

### **2.3 Imaging**

The cores were securely transported to the CLS for imaging experiments (University of Saskatchewan, Saskatoon, Saskatchewan). The cores were secured to the mounting station in the BMIT-BM beamline. Before imaging, the samples were rotated to check for lateral movement. Significant lateral movement can cause issues during subsequent reconstruction and image analysis. Three thousand image projections were acquired for each sample with a 180-degree rotation and a 0.06-step increment. An additional 100 flat and 50 dark images were taken to correct for noise of the detector and X-rays in the images during reconstruction for a total of 3,150 projections. Flat images are images acquired with the shutter open and x-rays passing through, but the sample has been removed, so no x-rays are passing through the sample and on to the detector. Dark images are taken with the shutter closed to acquire a dark profile. The highly sensitive camera cannot be removed and cleaned every time dust collects on it or the scintillator. The flats and dark images correct for these 'impurities' to improve data quality. The energy set for the experiments, pixel size, and sample detector distance were 20 keV, 1.5  $\mu\text{m}$ , and 0.05 m, respectively.

### **2.4 Image Processing**

Tofu (Karlsruhe Institute of Technology, Karlsruhe, Germany)<sup>103,104</sup>, software developed by beamline scientists at CLS and colleagues, was the platform used to reconstruct the images with a Fourier transform to produce 3-dimensional image stacks while reducing noise and artifacts within the sample. A set of images typically includes cortical and trabecular bone, and outside space. Cortical bone was the target of analysis. Thus, the sample was cropped using ImageJ v. 1.53t (National Institute of Health, Bethesda, United States of America)<sup>71</sup>, excluding trabecular bone

and empty space. All samples were cropped, striking a balance between the largest area and the number of slices included.

## 2.5 Image Segmentation

The image segmentation aimed to isolate osteocyte lacunae and porous structures for morphological analysis. The nomenclature was standardized according to the American Society of Bone Mineral Research (ASBMR)<sup>69,70</sup>. Several morphological parameters extracted for statistical comparison include lacunar and pore diameter, lacunar and pore thickness, lacunar and pore volume, and lacunar and pore density (**Table 2.2**).

**Table 2.2.** CTAn laboratory  $\mu$ CT parameters converted to SR $\mu$ CT parameters

CTAn ASBMR term	Translation for pores	Translation for lacunae
Bone volume	Pore volume	Lacunar volume
Bone surface	Pore surface	Lacunar surface
Bone volume fraction	Pore volume percentage	Lacunar volume percentage
Bone surface-to-tissue volume	Pore surface to volume	Lacunar surface to volume
Trabecular thickness	Pore diameter	Lacunar diameter
Trabecular separation	Pore separation	Lacunar separation
Structural model index	Pore circularity	Lacunar circularity
Degree of anisotropy	Pore degree of anisotropy	Lacunar Degree of Anisotropy
Number of objects	Number of pores	Number of lacunae

## 2.6 Deep Learning

All SR $\mu$ CT data sets were imported into ORS Dragonfly software for segmentation and deep-learning training. Using Dragonfly’s extensive region of interest (ROI) tools, pores and lacunae were isolated into separate ROIs. All slices were manually checked, ensuring all humanly identifiable objects, such as pores and lacunae, were correctly labelled. All issues were manually corrected before training the deep learning model. Each sample dataset consisted of 57 slices with

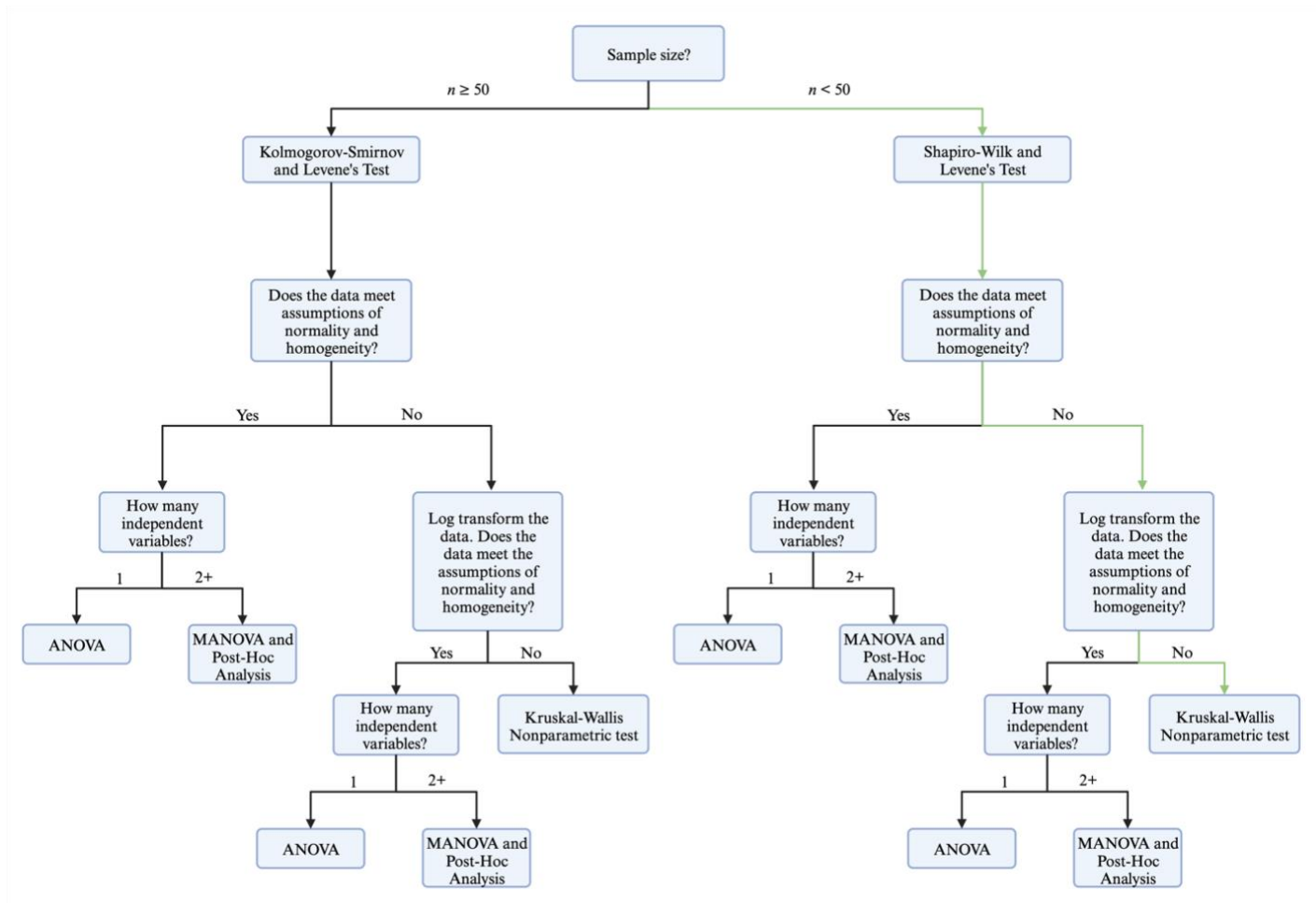
six total datasets. Two deep learning models were trained: one for porosity (as it includes resorptive areas) and the other for the lacunae. Each model has two classes: the segmentation target (pore or lacunae) and the background. This process has yet to be applied to bone specimens. As such, all available architectures in ORS Dragonfly were tested. The efficacy of these models was compared using their best reported ORSDiceLoss (**Appendix 7.2**). The lower the reported DiceLoss values, the more overlap between the ground truths and the trained model and less unlabeled neighboring voxels. DiceLoss was the chosen metric because it is not affected by imbalanced classes and is generally recommended for medical imaging<sup>90</sup>. The architecture that was determined to provide the best segmentation results was UNet++<sup>91</sup>.

The training parameters (e.g., data augmentation, stride ratio, patch size) were extensively tested to develop the most accurate model (**Appendix 7.2**). The model was trained for two days using the six pore training datasets. A different model with identical parameters was trained for two days using the six lacunar datasets. These fully operational models were applied to all 97 samples. Each sample underwent morphological operations (e.g., closing) to correct the few mistakes in the model's segmentation output. All samples were manually checked and approved by the user. All ROIs produced by the deep learning model and corrected by the user are binarized and exported. The samples are imported CTAn (Bruker, Billerica, United States of America) for data extraction (**Appendix 7.3**).

## **2.7 Statistical analysis**

All statistics were computed in SPSS (v. 28.0.1.0, IBM, Armonk, United States of America). Descriptive statistics were calculated for each dependent variable. The distribution of data points

was tested for normality using Shapiro-Wilk tests. Homogeneity of variances were calculated using Levene's tests. If a variable violated the Shapiro-Wilk or Levene's test, it was log-transformed with a base of 10. The data were also tested for outliers and extreme outliers. A data point was considered an extreme outlier if it was outside the first and third quartile  $\pm$  three \* the interquartile range. A normal outlier follows the same equation except substituting the three for a 1.5. Samples that were repeatedly classified as outliers were considered for removal. Kruskal-Wallis nonparametric tests were used to compare the effects of age, sex, and experimental group on lacunar and pore morphometric variables (**Figure 2.1**). Multivariate linear regressions were conducted to determine the relationship between age and sex and age and experimental group.



**Figure 2.1.** The statistical decision tree employed to choose the correct tests. The chosen route (green arrows) saw the employment of Shapiro-Wilk’s normality test, Levene’s homogeneity test, and Kruskal-Wallis nonparametric test. This image was created in BioRender.



The deep learning model was compared to CTAn and manual segmentations with their respective pore and lacunar measurements. Additionally, the DICE similarity coefficient and true positive rate (TPR) were calculated using manual segmentation and utilized to compare the deep learning U-Net++ model and CTAn approach. DICE is a comparison between the manual outcome and the segmentation being compared. The score is between 0 and 1, with a closer value to one representing a segmentation more similar to the manual outcome. TPR is comparable to DICE in its measurement scoring, however, it measures the number of pixels correctly identified as a group. These measurements were selected as they are commonly used to evaluate the effectiveness of a model<sup>90,94,99,105</sup>.

### 3. Results

A breakdown of the sample demographics and potential categorical groups can be viewed in **Table 3.1**. The samples were categorized into opioid use or control based on their previous reported history of opioid use which is presented in **Table 2.1**. Descriptives for the bone morphometric parameters were extracted in CTAn from dragonfly-trained SR $\mu$ CT data and are located in **Table 3.2**. The data were tested for normality and homogeneity. When split by age and sex, eight variables failed the Shapiro-Wilks normality tests, and two failed Levene's test for homogeneity of variances. The trend persisted even after log-transforming the data (**Table 3.3**). Similarly, when split into groups based on sex, age, and opioid use, the data failed to meet assumptions of normality and homogeneity (**Table 3.4**). Since no normality and homogeneity could be established in the data, a Kruskal-Wallis nonparametric test was used to analyze the differences between the groups with a Tukey-Kramer post hoc analysis. This test does not make assumptions based on the dataset's normality. Additionally, linear regressions were used to determine if there was a linear relationship between each variable and age. The linear regressions were further split by sex to establish sex-specific trends in aging. To analyze the efficaciousness of our deep learning model an analysis of variance (ANOVA) and a student's *t*-test were employed. Data were extracted in CTAn and ORS Dragonfly to avoid any potential computer software biases. For the normality, homogeneity, Kruskal-Wallis, ANOVA, and student *t*-tests, a *p*-value less than 0.05 was considered statistically significant.

**Table 3.1.** The specific breakdown of all samples crossed by age, sex, and experimental group.

<b>Experimental Group</b>			
<b>Age</b>	<b>Sex</b>	<b>Control</b>	<b>Opioid user</b>
20-29	Male	7	6
	Female	3	5
30-39	Male	7	7
	Female	7	3
40-49	Male	7	11
	Female	6	4
50-59	Male	6	9
	Female	7	2
Totals		50	47

**Table 3.2.** Descriptive statistics for lacunar and pore morphometric variables

<b>Variable</b>	<b>Mean</b>	<b>Skewness</b>	<b>Kurtosis</b>
<b>% Lacunar Volume</b>	0.637	0.88	3.035
<b>% Lacunar Surface Area</b>	0.769	1.101	1.993
<b>Lacunar Surface : Volume</b>	1.035	-0.038	14.135
<b>Lacunar Surface Density</b>	4.329	-1.1492	5.156
<b>Lacunar Diameter</b>	2280.416	4.716	20.778
<b>Lacunar Separation</b>	38296.331	4.719	20.8
<b>Lacunar Structural Model Index</b>	2.603	-1.457	4.356
<b>Lacunar Degree of Anisotropy</b>	0.727	0.303	3.288
<b>Lacunar Number Density</b>	5651.031	6.456	42.695
<b>% Pore Volume</b>	5.805	1.86	6.665
<b>% Pore Surface Area</b>	48.042	0.642	0.794
<b>Pore Surface : Volume</b>	0.119	2.391	11.057
<b>Pore Surface Density</b>	0.006	1.317	3.628
<b>Pore Diameter</b>	67.048	0.972	1.585
<b>Pore Separation</b>	271.975	0.729	0.273
<b>Pore Structural Model Index</b>	2.649	0.387	0.005
<b>Pore Degree of Anisotropy</b>	0.864	-1.608	3.800
<b>Pore Number Density</b>	22.516	1.742	2.493

**Table 3.3.** Normality and homogeneity tests when split by sex and age after log transformation

<b>Homogeneity Test (Sex_Age)</b>	<b>% Pore Volume</b>	<b>% Pore Surface Area</b>	<b>Pore Surface Volume Ratio</b>	<b>Pore Surface Density</b>	<b>Pore Diameter</b>	<b>Pore Separation</b>	<b>SMI</b>	<b>DA</b>	<b>Number Density</b>
Levene	0.053	0.143	0.445	0.19	0.475	0.911	0.95	0.198	0.129
<b>Normality Tests (Sex_Age)</b>	<b>% Pore Volume</b>	<b>% Pore Surface Area</b>	<b>Pore Surface Volume Ratio</b>	<b>Pore Surface Density</b>	<b>Pore Diameter</b>	<b>Pore Separation</b>	<b>SMI</b>	<b>DA</b>	<b>Number Density</b>
Shapiro-Wilk (20F)	0.578	0.205	0.263	0.164	0.807	0.094	0.98	0.029	0.454
Shapiro-Wilk (20M)	<b>0.001</b>	<b>0.0001</b>	0.187	<b>0.0002</b>	0.366	0.463	0.92	<b>0.0001</b>	0.836
Shapiro-Wilk (30F)	0.866	0.834	0.14	<b>0.032</b>	0.256	0.325	0.79	0.05	0.65
Shapiro-Wilk (30M)	0.522	0.126	0.195	0.957	0.538	0.971	0.41	0.314	0.438
Shapiro-Wilk (40F)	0.608	0.138	0.804	0.546	0.817	0.526	0.94	<b>0.023</b>	0.471
Shapiro-Wilk (40M)	0.701	0.6	0.466	0.075	0.167	0.293	0.38	<b>0.002</b>	0.816
Shapiro-Wilk (50F)	0.746	0.785	<b>0.043</b>	0.729	0.146	0.245	0.54	<b>0.01</b>	0.176
Shapiro-Wilk (50M)	0.585	0.192	0.613	0.915	0.37	0.151	0.99	0.758	0.668
<b>Homogeneity Test (Sex_Age)</b>	<b>% Lacunar Volume</b>	<b>% Lacunar Surface Area</b>	<b>Lacunar Surface Volume Ratio</b>	<b>Lacunar Surface Density</b>	<b>Lacunar Diameter</b>	<b>Lacunar Separation</b>	<b>SMI</b>	<b>DA</b>	<b>Number Density</b>
Levene	0.235	0.124	<b>0.01</b>	0.34	0.706	<b>0.001</b>	0.57	0.221	<b>0.004</b>
<b>Normality Tests (Sex_Age)</b>	<b>% Lacunar Volume</b>	<b>% Lacunar Surface Area</b>	<b>Lacunar Surface Volume Ratio</b>	<b>Lacunar Surface Density</b>	<b>Lacunar Diameter</b>	<b>Lacunar Separation</b>	<b>SMI</b>	<b>DA</b>	<b>Number Density</b>
Shapiro-Wilk (20F)	<b>0.004</b>	0.828	0.351	0.051	0.269	0.768	0.55	<b>0.045</b>	0.256

Shapiro-Wilk (20M)	0.768	<b><i>1.71E-15</i></b>	<b><i>0.000011</i></b>	0.891	0.347	<b><i>0.000004</i></b>	<b><i>0</i></b>	0.723	<b><i>0.000045</i></b>
Shapiro-Wilk (30F)	0.606	<b><i>0.015</i></b>	0.276	0.782	0.142	0.367	0.52	0.236	0.46
Shapiro-Wilk (30M)	0.445	0.973	<b><i>0.000062</i></b>	0.061	0.004	<b><i>0.005</i></b>	0.98	0.21	<b><i>0.000022</i></b>
Shapiro-Wilk (40F)	0.165	0.898	0.963	0.25	0.791	0.948	0.79	0.591	0.217
Shapiro-Wilk (40M)	0.086	0.944	<b><i>0.000001</i></b>	<b><i>0.025</i></b>	<b><i>0.000009</i></b>	<b><i>0.001</i></b>	0.66	0.152	<b><i>0.000006</i></b>
Shapiro-Wilk (50F)	0.983	<b><i>0.000089</i></b>	<b><i>0.000217</i></b>	0.149	0.059	<b><i>0.000013</i></b>	0.37	0.413	<b><i>0.000211</i></b>
Shapiro-Wilk (50M)	0.604	0.281	<b><i>0.000028</i></b>	0.981	<b><i>0.000424</i></b>	0.115	<b><i>0</i></b>	0.068	<b><i>0.000035</i></b>

\* Bold and italics represent statistical significance. SMI – structural model index and DA – degree of anisotropy. Essentially SMI is a measure of roundness of an object and DA is a measure of orientation of structures along a particular axis.

**Table 3.4.** Log-transformed normality and homogeneity tests when split by age, sex, and opioid use.

<b>Normality Tests</b>	<b>% Pore Volume</b>	<b>% Pore Surface Area</b>	<b>Pore Surface Volume Ratio</b>	<b>Pore Surface Density</b>	<b>Pore Diameter</b>	<b>Pore Separation</b>	<b>SMI</b>	<b>DA</b>	<b>Number Density</b>
Shapiro-Wilk (20Fc)	0.764	0.841	0.502	0.211	0.966	0.436	0.6	<b>0.02</b>	0.902
Shapiro-Wilk (20Fd)	0.577	0.057	0.206	0.149	0.607	0.163	0.84	0.09	0.238
Shapiro-Wilk (20Mc)	0.135	0.982	0.603	0.372	0.39	0.71	0.9	<b>0</b>	0.957
Shapiro-Wilk (20Md)	0.046	<b>0.006</b>	0.379	<b>0.021</b>	0.291	0.096	0.55	0.13	0.297
Shapiro-Wilk (30Fc)	0.954	0.905	0.42	0.073	0.482	0.606	0.8	0.58	0.882
Shapiro-Wilk (30Fd)	0.583	0.862	0.852	0.463	0.739	0.148	0.71	0.24	0.635
Shapiro-Wilk (30Mc)	0.741	0.314	0.53	0.168	0.628	0.465	0.82	0.4	0.622

Shapiro-Wilk (30Md)	0.328	<b>0.013</b>	0.294	0.76	0.702	0.464	0.63	0.14	0.481
Shapiro-Wilk (40Fc)	0.387	<b>0.047</b>	0.797	0.976	0.651	0.694	0.65	<b>0.02</b>	0.653
Shapiro-Wilk (40Fd)	0.714	0.877	0.478	0.955	0.807	0.575	0.22	0.78	0.819
Shapiro-Wilk (40Mc)	0.566	<b>0.014</b>	0.954	<b>0.001</b>	0.92	0.533	0.27	0.75	0.963
Shapiro-Wilk (40Md)	<b>0.047</b>	0.695	0.285	0.722	0.163	0.721	0.36	<b>0</b>	0.781
Shapiro-Wilk (50Fc)	0.489	0.815	0.216	0.779	0.341	0.414	0.15	<b>0.01</b>	0.169
Shapiro-Wilk (50Fd)	-	-	-	-	-	-	-	-	-
Shapiro-Wilk (50Mc)	<b>0.02</b>	0.285	0.86	0.724	0.881	0.72	0.66	0.88	0.926
Shapiro-Wilk (50Md)	0.608	0.076	0.494	0.681	0.593	0.145	0.75	0.94	0.922



Normality Tests	% Lacunar Volume	% Lacunar Surface Area	Lacunar Surface Volume Ratio	Lacunar Surface Density	Lacunar Diameter	Lacunar Separation	SMI	DA	Number Density
Shapiro-Wilk (20Fc)	<b>0.025</b>	0.559	0.793	0.701	0.529	0.803	0.59	0.37	0.461
Shapiro-Wilk (20Fd)	<b>0.001</b>	0.991	0.549	0.153	0.416	0.482	<b>0.03</b>	0.11	0.263
Shapiro-Wilk (20Mc)	0.931	0.338	0.828	0.904	0.495	0.678	0.73	0.81	1
Shapiro-Wilk (20Md)	0.937	<b>0.01</b>	<b>0.005</b>	0.787	0.635	<b>0.000971</b>	<b>0.04</b>	0.42	<b>0.029</b>
Shapiro-Wilk (30Fc)	0.793	<b>0.003</b>	0.125	0.896	0.142	0.523	0.38	0.28	0.654
Shapiro-Wilk (30Fd)	0.594	0.427	-	0.632	0.918	0.475	0.19	0.47	0.864
Shapiro-Wilk (30Mc)	0.301	0.548	<b>0.003</b>	<b>0.025</b>	<b>0.031</b>	<b>0.019</b>	0.92	0.36	<b>0.00007</b>

Shapiro-Wilk (30Md)	0.569	0.471	0.85	0.644	0.748	0.745	0.71	0.72	0.654
Shapiro-Wilk (40Fc)	0.349	0.617	0.951	0.148	0.941	0.989	0.74	0.51	0.177
Shapiro-Wilk (40Fd)	0.1	0.493	0.886	0.345	0.244	0.282	0.26	0.06	0.875
Shapiro-Wilk (40Mc)	0.647	0.474	0.885	0.23	0.994	0.984	0.87	0.73	0.736
Shapiro-Wilk (40Md)	0.287	0.932	<b>0.000004</b>	<b>0.012</b>	<b>0.000044</b>	<b>0.000413</b>	0.66	<b>0</b>	<b>0.000002</b>
Shapiro-Wilk (50Fc)	0.684	<b>0.001</b>	<b>0.000058</b>	0.512	0.182	<b>0.000021</b>	0.21	0.25	<b>0.000003</b>
Shapiro-Wilk (50Fd)	-	-	-	-	-	-	-	-	-
Shapiro-Wilk (50Mc)	0.973	<b>0.024</b>	<b>0.004</b>	0.982	0.051	0.245	0.49	0.8	<b>0.014</b>
Shapiro-Wilk (50Md)	0.245	0.791	0.446	0.34	0.983	0.932	<b>0</b>	0.27	0.058

\* F – Female, M – Male, c – control, d – opioid use. Bold and italics represent the significance.

### **3.1 Kruskal-Wallis nonparametric tests revealed significant differences between age, sex, and opioid use.**

Kruskal-Wallis nonparametric tests was split by opioid use, sex, and age, and revealed a significant difference in percent lacunar volume ( $p = 0.016$ ), percent lacunar surface area ( $p = 0.029$ ), lacunar surface density ( $p = 0.029$ ), and lacunar number density ( $p = 0.047$ ) (**Table 3.5**). The remaining lacunar variables and all pore variables were not significant (**Table 3.6**). Tukey-Kramer post hoc tests indicate that most comparisons are significantly different due to age (**Figure 3.1**) or the interaction of sex and age. The percentage of lacunar surface area decreased with opioid use between males in their 20s ( $p = 0.029$ ) and their 50s ( $p = 0.046$ ) (**Table 3.5**). Further, males in their 30s differed in lacunar surface area to volume ratio ( $p = 0.018$ ) and lacunar diameter ( $p = 0.025$ ) from opioid use. Lacunar degree of anisotropy significantly differed among males in their 20s ( $p = 0.032$ ) and females in their 50s ( $p = 0.034$ ) due to opioid use (**Figures 3.2, 3.3**). Degree of anisotropy for lacunae is the level of which the lacunae are not organized along the same direction. Groups with a higher degree of anisotropy are likely to be stronger in all directions, but weaker in the principal loading direction compared to samples that are more isotropic. There are an additional 37 interactions where opioid use may contribute to deteriorating bone health, however, sex or age (in some instances both) differ, so discerning the cause of the deterioration is impossible.

**Table 3.5.** Kruskal-Wallis Non-parametric Tests with Tukey Kramer Post Hoc Analysis of Lacunar Morphometric Variables.

	<b>% Lacunar Volume</b>	<b>% Lacunar Surface Area</b>	<b>Lacunar Surface Volume Ratio</b>	<b>Lacunar Surface Density</b>	<b>Lacunar Diameter</b>	<b>Lacunar Separation</b>	<b>Lacunar SMI</b>	<b>Lacunar DA</b>	<b>Lacunar Number Density</b>
<b>Kruskal-Wallis (significance)</b>	<b>0.016</b>	<b>0.029</b>	0.402	<b>0.029</b>	0.575	0.254	0.828	0.387	<b>0.047</b>
<b>20 Male Opioid user - 20 Female Control</b>	0.269	<b>0.018</b>	0.485	0.734	0.538	0.549	0.237	0.808	0.719
<b>20 Male Opioid user - 20 Female Opioid user</b>	0.289	<b>0.041</b>	0.394	0.949	0.641	0.562	0.449	0.081	0.936
<b>20 Male Opioid user - 20 Male Control</b>	0.195	<b>0.029</b>	0.137	0.957	0.207	0.641	0.663	<b>0.032</b>	0.95
<b>30 Male Control - 20 Male Control</b>	0.059	0.202	<b>0.044</b>	0.138	0.054	0.479	0.351	0.235	0.144
<b>30 Male Control - 30 Male Opioid user</b>	0.149	0.758	<b>0.018</b>	0.37	<b>0.025</b>	0.518	0.176	0.711	0.428
<b>30 Male Opioid user - 20 Female Control</b>	0.665	0.158	<b>0.029</b>	0.449	0.058	0.3	0.236	0.396	0.402
<b>40 Female Control - 20 Female Control</b>	0.13	<b>0.014</b>	0.142	0.094	0.139	0.066	0.132	0.913	0.144

<b>40 Female Control - 20 Female Opioid user</b>	0.124	<b>0.033</b>	0.963	0.135	0.589	0.386	0.257	0.182	0.228
<b>40 Female Control - 20 Male Control</b>	0.069	<b>0.022</b>	0.612	0.08	0.869	0.267	0.397	0.089	0.144
<b>40 Female Control - 30 Female Control</b>	0.266	<b>0.048</b>	0.818	0.247	0.438	0.388	0.16	0.319	0.467
<b>40 Female Opioid user - 20 Female Opioid user</b>	<b>0.048</b>	0.42	0.331	0.069	0.693	0.315	0.877	0.505	0.085
<b>40 Female Opioid user - 20 Male Control</b>	<b>0.025</b>	0.407	0.124	<b>0.04</b>	0.275	0.222	0.610	0.352	<b>0.048</b>
<b>40 Male Control - 20 Female Control</b>	<b>0.008</b>	<b>0.025</b>	0.168	<b>0.005</b>	0.203	<b>0.007</b>	0.296	0.216	<b>0.007</b>
<b>40 Male Control - 20 Female Opioid user</b>	<b>0.004</b>	0.058	0.92	<b>0.005</b>	0.784	0.065	0.558	0.957	<b>0.007</b>
<b>40 Male Control - 20 Male Control</b>	<b>0.001</b>	<b>0.042</b>	0.489	<b>0.001</b>	0.628	<b>0.028</b>	0.812	0.754	<b>0.002</b>
<b>40 Male Control - 20 Male Opioid user</b>	0.063	0.818	0.412	<b>0.002</b>	0.426	<b>0.01</b>	0.836	0.065	<b>0.004</b>

<b>40 Male Control - 30 Female Control</b>	<i>0.011</i>	0.087	0.939	<i>0.01</i>	0.621	0.053	0.413	0.676	<i>0.019</i>
<b>40 Male Control - 30 Male Opioid user</b>	<i>0.005</i>	0.285	0.297	<i>0.009</i>	0.422	<i>0.033</i>	0.856	0.615	<i>0.015</i>
<b>40 Male Control - 50 Male Control</b>	0.258	0.17	0.836	0.089	0.715	0.169	0.709	0.85	<i>0.045</i>
<b>40 Male Opioid user - 20 Female Control</b>	0.051	<i>0.017</i>	0.223	0.053	0.31	0.073	0.281	0.426	0.068
<b>40 Male Opioid user - 20 Female Opioid user</b>	<i>0.036</i>	<i>0.037</i>	0.69	0.069	0.916	0.464	0.52	0.496	0.1
<b>40 Male Opioid user - 20 Male Control</b>	<i>0.012</i>	<i>0.022</i>	0.277	<i>0.03</i>	0.324	0.314	0.786	0.298	<i>0.045</i>
<b>40 Male Opioid user - 20 Male Opioid user</b>	0.333	0.825	0.553	<i>0.044</i>	0.657	0.142	0.827	0.174	0.066
<b>40 Male Opioid user - 30 Male Opioid user</b>	<i>0.044</i>	0.225	0.14	0.127	0.181	0.348	0.848	0.891	0.206
<b>50 Female Control - 20 Female Control</b>	<i>0.029</i>	<i>0.008</i>	0.585	0.104	0.513	0.141	0.278	0.816	0.104
<b>50 Female Control - 20</b>	<i>0.019</i>	<i>0.016</i>	0.28	0.149	0.65	0.681	0.532	0.074	0.161

<b>Female Opioid user</b>									
<b>50 Female Control - 20 Male Control</b>	<i>0.007</i>	<i>0.01</i>	0.078	0.087	0.2	0.534	0.779	<i>0.027</i>	0.091
<b>50 Female Control - 30 Female Control</b>	<i>0.048</i>	<i>0.024</i>	0.319	0.275	0.761	0.715	0.389	0.139	0.355
<b>50 Female Control - 30 Male Opioid user</b>	<i>0.024</i>	0.105	<i>0.034</i>	0.26	0.11	0.575	0.89	0.163	0.307
<b>50 Female Control - 50 Male Control</b>	0.563	0.057	0.41	0.797	0.688	0.894	0.74	<i>0.044</i>	0.518
<b>50 Female Control - 50 Male Opioid user</b>	0.843	0.988	0.707	0.544	0.953	0.162	0.307	<i>0.039</i>	0.481
<b>50 Female Opioid user - 20 Male Control</b>	0.561	0.268	<i>0.047</i>	0.801	<i>0.046</i>	0.875	0.828	0.518	0.889
<b>50 Female Opioid user - 20 Male Opioid user</b>	0.755	0.687	0.346	0.833	0.272	0.637	0.933	<i>0.036</i>	0.925
<b>50 Female Opioid user - 30 Male Opioid user</b>	0.776	0.644	<i>0.026</i>	0.89	<i>0.027</i>	0.908	0.951	0.234	0.759



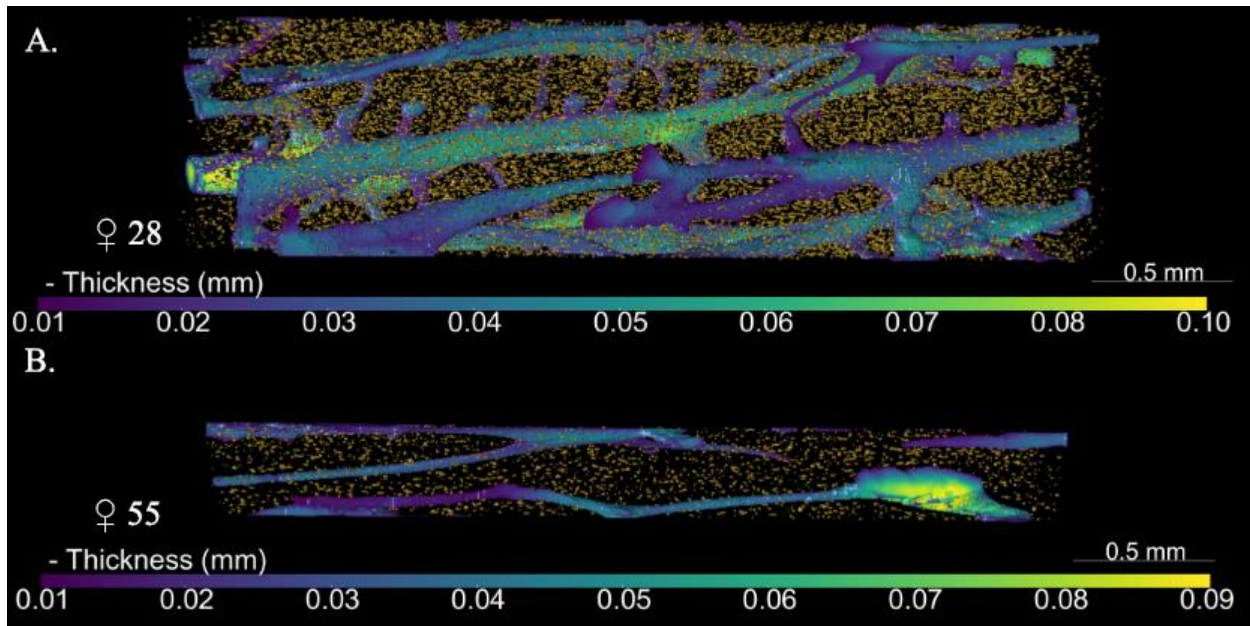
<b>50 Female Opioid user - 50 Female Control</b>	0.221	0.537	0.415	0.375	0.254	0.796	0.976	<b>0.034</b>	0.323
<b>50 Male Control - 20 Male Control</b>	<b>0.043</b>	0.558	0.384	0.166	0.406	0.464	0.548	0.91	0.328
<b>50 Male Opioid user - 20 Female Control</b>	<b>0.035</b>	<b>0.006</b>	0.379	<b>0.032</b>	0.47	<b>0.01</b>	0.731	0.187	<b>0.027</b>
<b>50 Male Opioid user - 20 Female Opioid user</b>	<b>0.023</b>	<b>0.012</b>	0.448	<b>0.039</b>	0.672	0.09	0.789	0.992	<b>0.035</b>
<b>50 Male Opioid user - 20 Male Control</b>	<b>0.007</b>	<b>0.006</b>	0.146	<b>0.016</b>	0.193	<b>0.04</b>	0.469	0.779	<b>0.013</b>
<b>50 Male Opioid user - 20 Male Opioid user</b>	0.234	0.763	0.86	<b>0.024</b>	0.93	<b>0.014</b>	0.249	<b>0.046</b>	<b>0.02</b>
<b>50 Male Opioid user - 30 Female Control</b>	0.058	<b>0.017</b>	0.522	0.078	0.793	0.074	0.914	0.621	0.092
<b>50 Male Opioid user - 30 Male Opioid user</b>	<b>0.028</b>	0.089	0.067	0.072	0.101	<b>0.046</b>	0.243	0.558	0.074
<b>50 Male Opioid user - 50 Male Control</b>	0.673	<b>0.046</b>	0.678	0.394	0.714	0.232	0.184	0.881	0.175

\*Interactions where there is no significance have been removed. Bold and italics represent statistical significance.

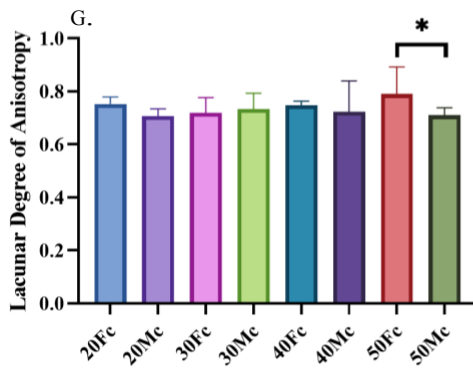
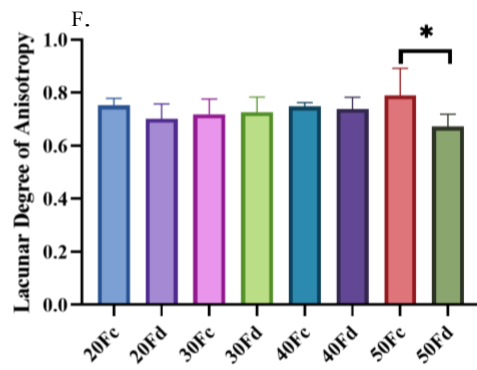
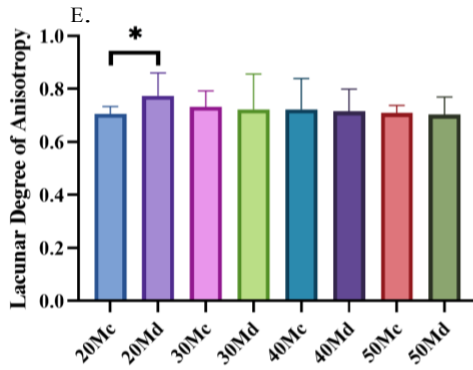
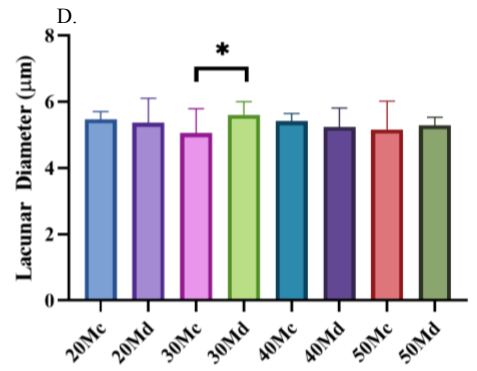
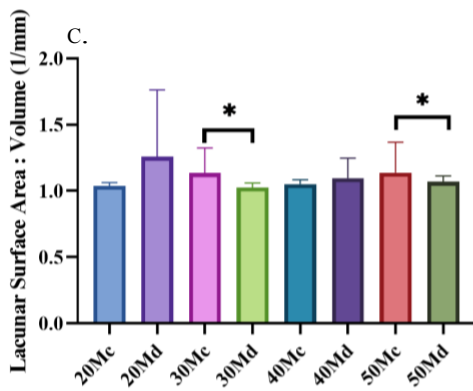
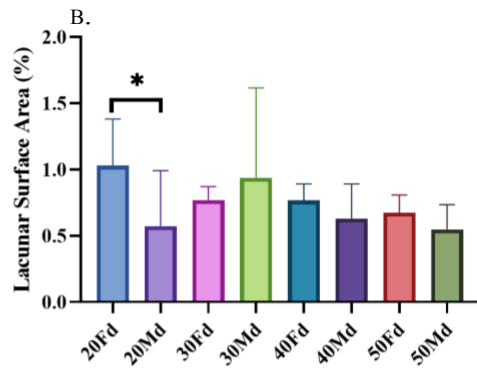
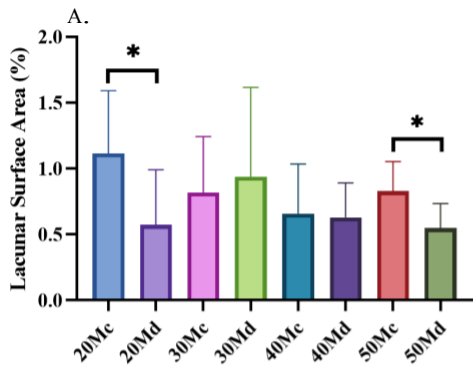
**Table 3.6.** Kruskal-Wallis Non-parametric Tests with Tukey Kramer Post Hoc Analysis of Pore Morphometric Variables.

	<b>% Pore Volume</b>	<b>% Pore Surface Area</b>	<b>Pore Surface Volume Ratio</b>	<b>Pore Surface Density</b>	<b>Pore Diameter</b>	<b>Pore Separation</b>	<b>Pore SMI</b>	<b>Pore DA</b>	<b>Pore Number Density</b>
<b>Kruskal-Wallis (significance)</b>	0.781	0.848	0.747	0.920	0.816	0.564	0.916	0.819	0.902
<b>20 Female Opioid user - 20 Female Control</b>	0.122	0.496	0.082	0.902	<b><i>0.048</i></b>	0.93	0.273	0.938	0.627
<b>30 Female Opioid user - 20 Female Control</b>	0.197	0.495	<b><i>0.03</i></b>	0.695	<b><i>0.03</i></b>	0.622	0.885	0.622	0.258
<b>40 Female Opioid user - 50 Male Opioid user</b>	0.258	0.915	0.509	0.109	0.559	<b><i>0.032</i></b>	0.98	0.854	0.722
<b>40 Male Control - 50 Male Control</b>	0.36	<b><i>0.028</i></b>	0.688	0.526	0.628	0.426	0.504	0.117	0.808
<b>50 Male Opioid user - 20 Female Control</b>	0.011	0.378	<b><i>0.011</i></b>	0.387	<b><i>0.012</i></b>	0.169	0.201	0.827	0.84
<b>50 Male Opioid user - 30 Female Opioid user</b>	0.331	0.962	0.915	0.179	0.882	<b><i>0.048</i></b>	0.271	0.41	0.113

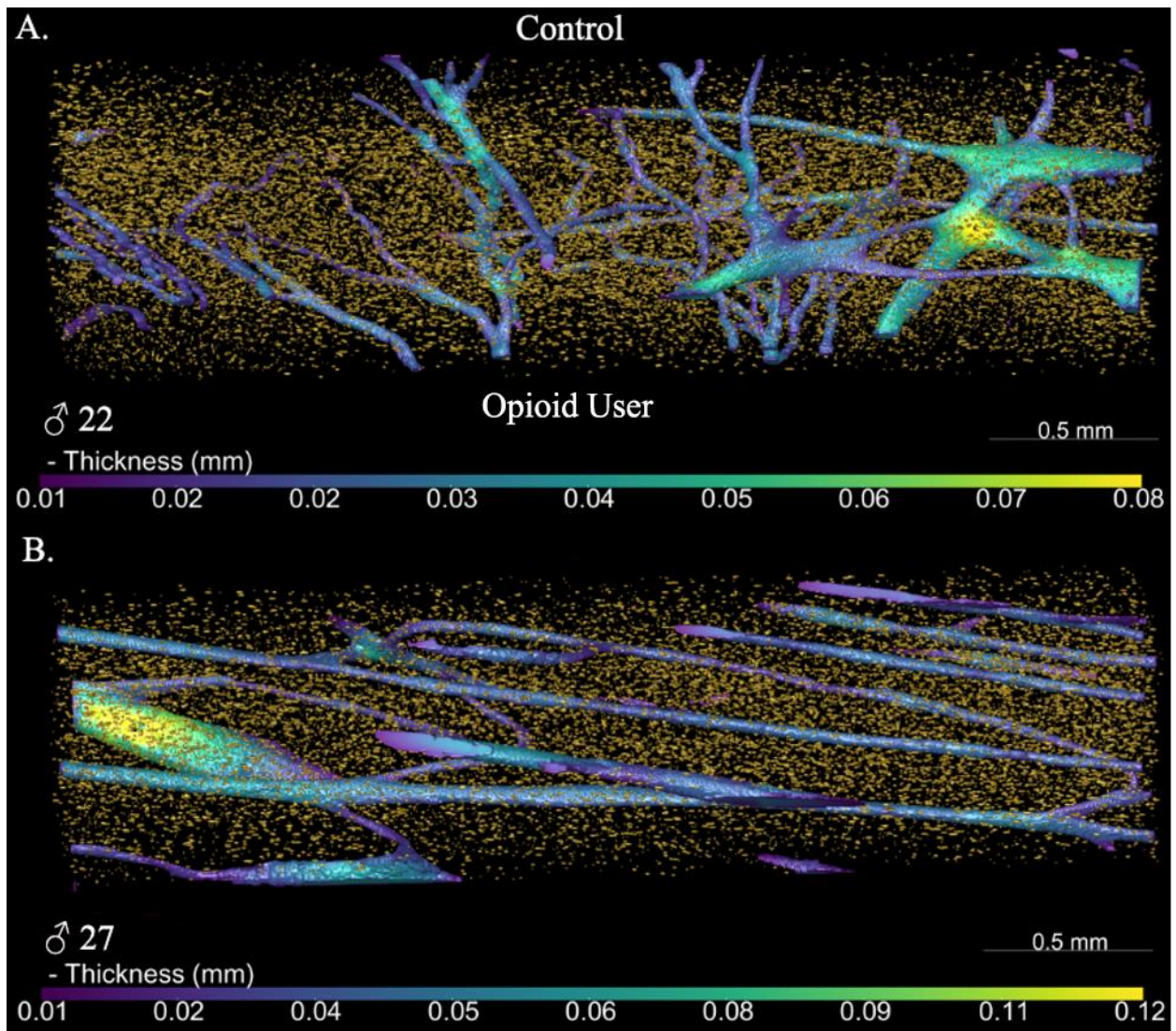
\*Interactions where there is no significance have been removed. Bold and italics represent statistical significance



**Figure 3.1.** SR $\mu$ CT renders of a young female adult (A) and an older female adult (B). Qualitatively, the density of lacunae (gold) decreases with age and porosity increases with age (multi-coloured). Scale Bar: 0.5 mm.



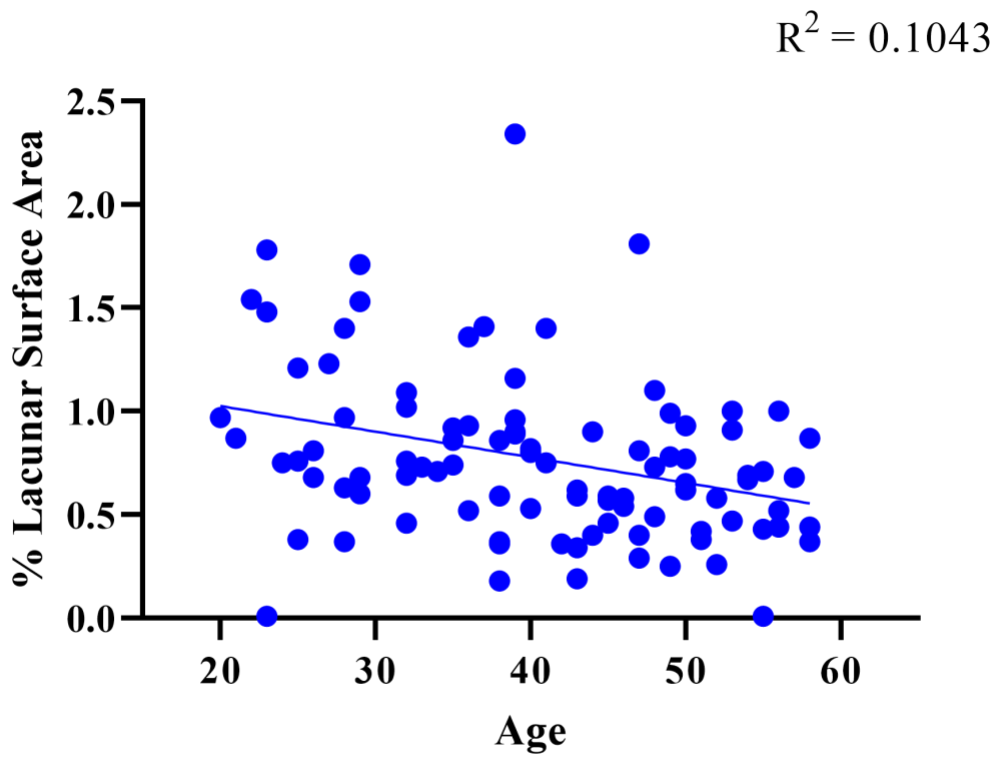
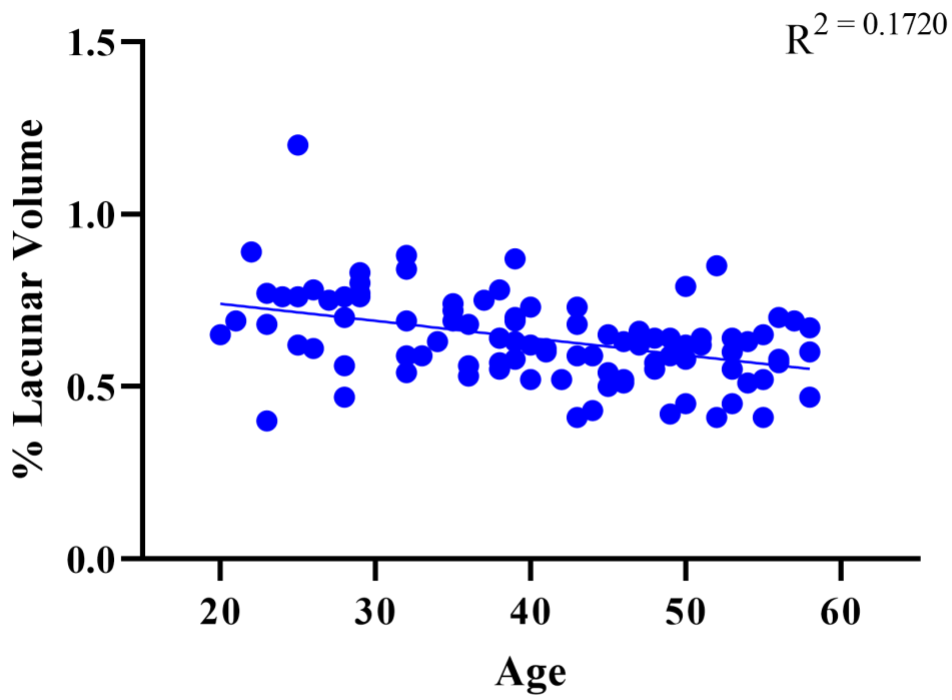
**Figure 3.2.** Synchrotron micro-CT data from ninety-seven human left sixth femora separated into age, sex, and opioid use classes (c – control, d – opioid use) lacunar morphometry compared via Kruskal-Wallis non-parametric tests. The \* indicates significant differences ( $p$ -value < 0.005) between the groups included under the brackets. Only differences where sex or opioid use were significant are represented. In the first graph (A), lacunar surface area was significantly different in the opioid use comparison for 20-year-old and 50-year-old males. A similar trend is observed as a sex difference in the 20-year-old opioid user category (B). Lacunar surface area to volume ratio (C) indicates a significant difference between opioid users and controls in the 30-year-old and 50-year-old males. A significant difference was observed in the 30-year-old male opioid user category for lacunar diameter (D). Lacunar degree of anisotropy displayed a significant difference between the 20-year-old male opioid user group and the controls (E). However, 50-year-old female opioid user group show an opposite trend for lacunar degree of anisotropy (F), with a decrease with opioid use compared to an increase with opioid use in the male subgroup. Finally, lacunar degree of anisotropy exhibited a significant difference between the 50-year-old male and females control groups (G).



**Figure 3.3.** Left sixth rib SR $\mu$ CT renders from a healthy control (A) and opioid user (B). Lacunar density (gold) is decreased in opioid users while their pores (multi-coloured) are larger in diameter. Scale Bar = 0.5 mm.

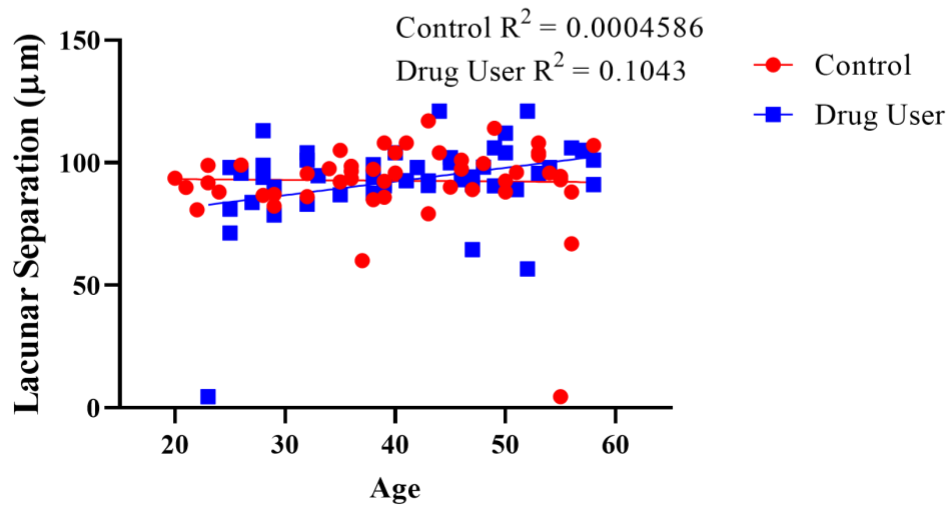
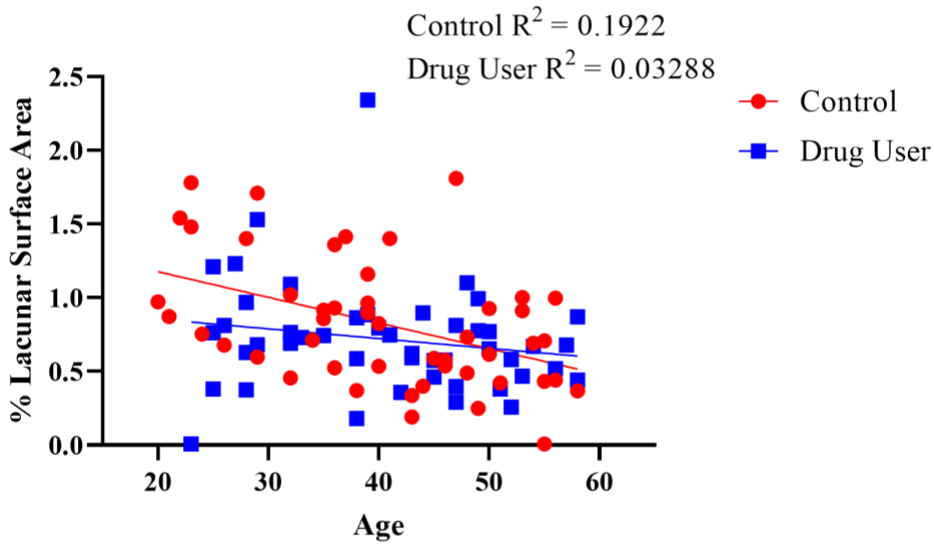
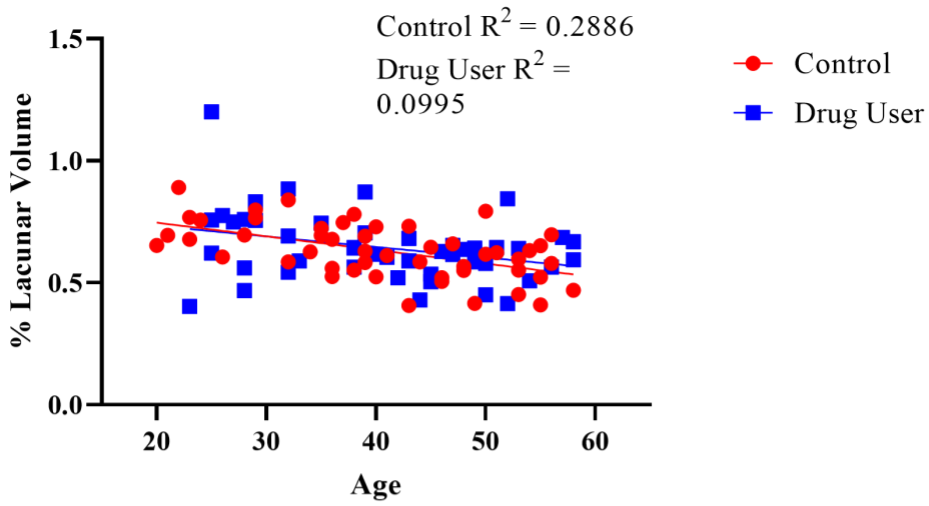
### 3.2 Age-related decline of lacunar morphology is disrupted by opioid use

Linear regressions were run to assess the impact of age on lacunar and pore morphometric variables over the lifespan. Weak correlations were determined between percent lacunar volume ( $r^2 = 0.1720$ ), percent lacunar surface area ( $r^2 = 0.1043$ ), and age (**Figure 3.4**). Running a multiple regression with age and opioid use revealed in percent lacunar volume (control  $r^2 = 0.2886$ , opioid user  $r^2 = 0.09995$ ) and percent lacunar surface area (control  $r^2 = 0.1922$ , opioid user  $r^2 = 0.03288$ ) that the linear trend was more significant in the control group than the opioid user group (**Figure 3.5**). A similar trend was observed when a multiple regression was run with age and sex. Females had a stronger correlation with age in percent lacunar volume (female  $r^2 = 0.2354$ , male  $r^2 = 0.1470$ ), percent lacunar surface area (female  $r^2 = 0.2451$ , male  $r^2 = 0.0529$ ), and pore number density (female  $r^2 = 0.1836$ , male  $r^2 = 0.002052$ ) than males (**Figures 3.6, 3.7**). These results suggest that drug use disrupt the normal aging process, however, percent lacunar surface area was lower in the drug use group compared to the control. This may suggest that drug use has created conditions where young drug users have bone similar to older controls.

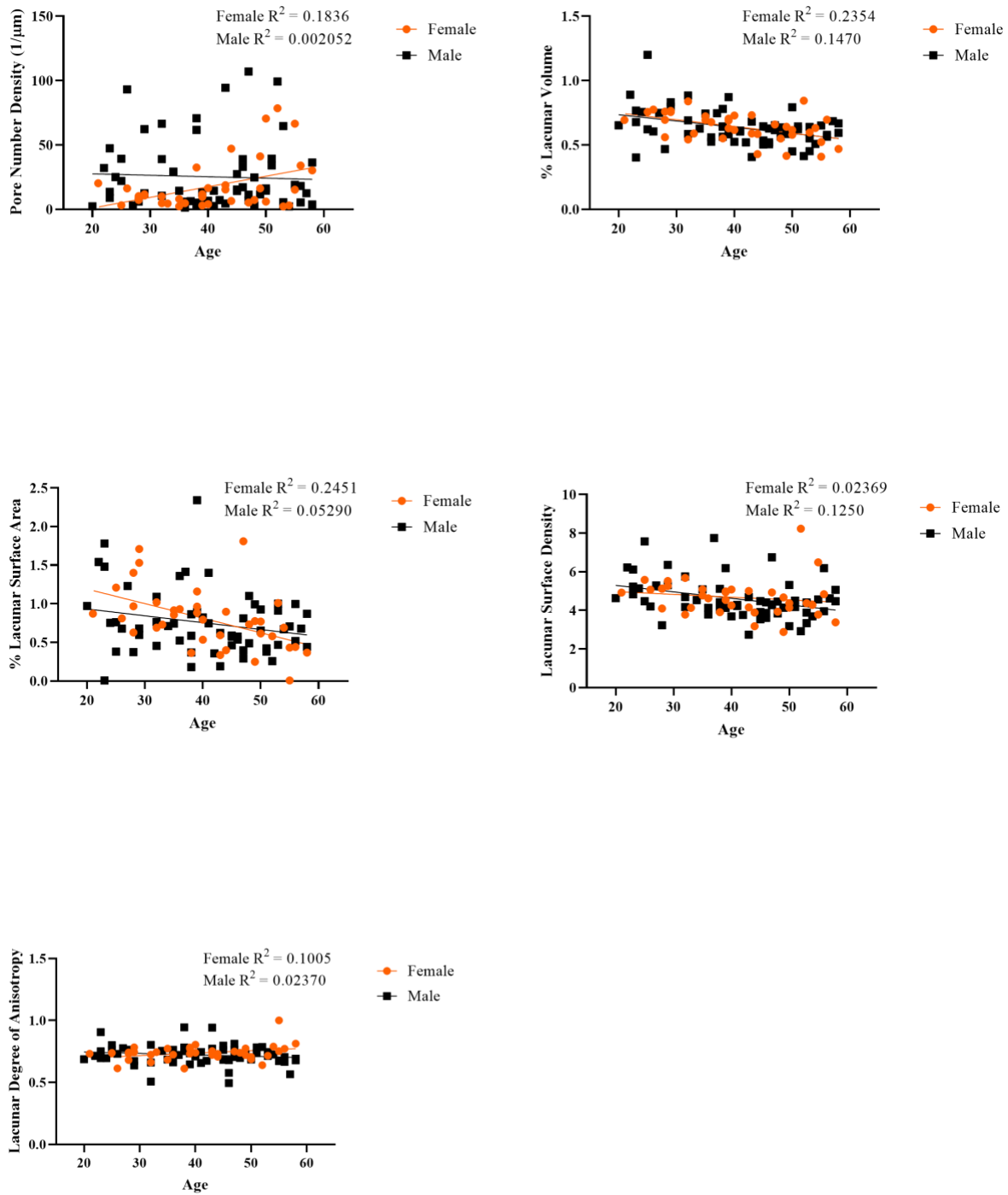




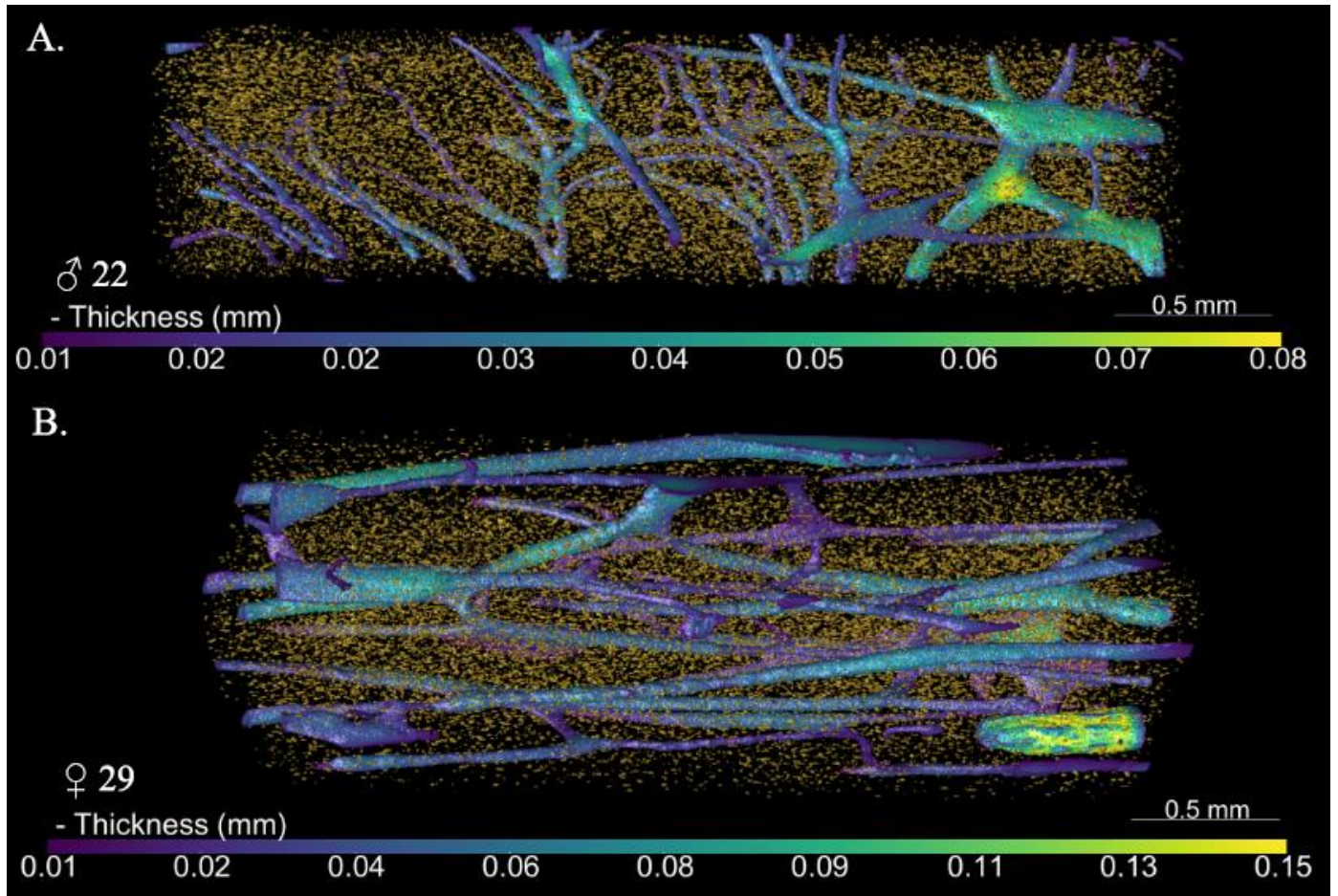
**Figure 3.4.** Linear regressions of 97 human left sixth ribs analyzing lacunar morphometrical parameters. The regressions show a correlation between declining percent lacunar volume and percent lacunar surface area with age. These are the two strongest correlations between all lacunar and pore morphometric variables analyzed.



**Figure 3.5.** Multiple linear regression correlating age and opioid use in the cohort of 97 individuals comparing lacunar morphometric data. A correlation between controls and age were observed in percent lacunar volume and percent lacunar surface area. However, opioid use does not have the same correlation. In fact, opioid use may have contributed to dysregulation of this correlation. This trend is reversed in lacunar separation with opioid use having a strong correlation with age and increasing separation.



**Figure 3.6.** Multiple linear regressions correlating age and sex. Deterioration of lacunar morphology was more highly correlated with females than males. The lone exception is lacunar surface density where males had a stronger correlation.



**Figure 3.7.** Three-dimensional renders of male (A) and female (B) left sixth ribs from SRμCT data. There is a higher lacunar density (gold) in the male specimen compared to the female. Porous structures (multi-coloured), however, were larger in diameter in females. Scale Bar = 0.5 mm.

### 3.3 CTAn outperformed deep learning in segmentation accuracy

The deep learning architecture chosen for this experimental model was U-Net++. A subsection of these data were segmented manually, using the deep learning model, and traditional thresholding and despeckling techniques in CTAn (Bruker). The products of the two methods were compared to each other and the manual segmentation, which acted as the ground truth<sup>121</sup>. An analysis of variance (ANOVA) revealed that the established CTAn protocol and the deep learning model significantly differed in average lacunar volume ( $p = 0.005$ ), average lacunar surface ( $p = 0.022$ ), lacunar diameter ( $p = 0.001$ ), average pore volume ( $p = 0.005$ ), average pore surface ( $p = 0.002$ ), and pore number ( $p = 0.001$ ). The deep learning model differed from the manual segmentation in average lacunar surface area ( $p = 0.038$ ), average pore volume ( $p = 0.005$ ), average pore surface area ( $p = 0.002$ ), and pore number ( $p = 0.001$ ). However, CTAn differed from the manual segmentation in lacunar diameter ( $p = 0.018$ ; **Table 3.7**). The presented results indicate no statistical difference between DICE and TPR (**Table 3.8**). The DICE similarity coefficient represents the overall similarity of the segmentation to the manual segmentation indicating the most accurate segmentation. The DICE scores for lacunae were average for both CTAn and deep learning (0.668 and 0.599, respectively), while it was markedly improved for the identification of pores (0.815 and 0.807). True positive rate, known more commonly as sensitivity, is the ability of the segmentation methods to correctly identify a structure and classify it appropriately. For pore morphology, CTAn and deep learning segmentations performed exceptionally well (0.835 and 0.839). CTAn similarly performed well in the positive identification of lacunae (0.845), however, deep learning's performance was dismal in comparison (0.543).

**Table 3.7.** ANOVA tests between the deep learning model, CTAn, and manual segmentation

	<b>Lacunar Morphology</b>	<b>Avg Lacunar Volume (<math>\mu\text{m}^3</math>)</b>	<b>Total Lacunar Volume (<math>\mu\text{m}^3</math>)</b>	<b>Avg Lacunar Surface Area (<math>\mu\text{m}^2</math>)</b>	<b>Total Lacunar Surface Area (<math>\mu\text{m}^2</math>)</b>	<b>Lacunar Diameter (<math>\mu\text{m}</math>)</b>	<b>Lacunar Separation (<math>\mu\text{m}</math>)</b>	<b>Lacunar Number (#)</b>
<b>ANOVA</b>	Levene Statistic	0.976	0.315	0.96	0.474	0.752	0.025	0.957
	Shapiro-Wilk	0.753	0.757	0.905	0.56	0.891	0.001	0.092
	<i>p</i> -value	<b><i>0.007</i></b>	0.264	<b><i>0.015</i></b>	0.513	<b><i>0.001</i></b>	0.569	0.945
<b>Post-hoc</b>	CTAn - Deep Learning	<b><i>0.005</i></b>	0.98	<b><i>0.022</i></b>	0.534	<b><i>0.001</i></b>	0.742	0.942
	CTAn - Manual	0.672	0.929	0.957	0.987	<b><i>0.018</i></b>	0.984	0.97
	Deep Learning - Manual	<b><i>0.005</i></b>	0.861	<b><i>0.038</i></b>	0.625	0.225	0.73	0.995
	<b>Pore Morphology</b>	<b>Avg Pore Volume (<math>\mu\text{m}^3</math>)</b>	<b>Total Pore Volume (<math>\mu\text{m}^3</math>)</b>	<b>Pore Surface Area (<math>\mu\text{m}^2</math>)</b>	<b>Total Pore Surface Area (<math>\mu\text{m}^2</math>)</b>	<b>Pore Diameter (<math>\mu\text{m}</math>)</b>	<b>Pore Separation (<math>\mu\text{m}</math>)</b>	<b>Pore Number (#)</b>
<b>ANOVA</b>	Levene Statistic	0.047	0.935	0.028	0.988	0.971	0.227	0.001
	Shapiro-Wilk	0.045	0.002	0.02	0.003	0.061	0.032	0.001
	<i>p</i> -value	<b><i>0.001</i></b>	0.858	<b><i>0.001</i></b>	0.91	0.997	0.173	<b><i>0.001</i></b>
<b>Post-hoc</b>	CTAn - Deep Learning	<b><i>0.005</i></b>	0.98	<b><i>0.002</i></b>	0.911	0.997	0.234	<b><i>0.001</i></b>
	CTAn - Manual	0.672	0.929	0.644	0.996	0.998	1	0.961
	Deep Learning - Manual	<b><i>0.005</i></b>	0.861	<b><i>0.002</i></b>	0.945	1	0.226	<b><i>0.001</i></b>

\* Bold and italics represent statistical significance.

**Table 3.8.** DICE and TPR scores between the deep learning model and CTAn

<b>DICE</b>	<b>Lacunae</b>	<b>Pores</b>	<b>TPR</b>	<b>Lacunae</b>	<b>Pores</b>
<b>CTAn</b>	0.668	0.815	<b>CTAn</b>	0.849	0.835
<b>Deep Learning</b>	0.599	0.807	<b>Deep Learning</b>	0.543	0.839
<b>Levene</b>	0.14	0.991	<b>Levene</b>	0.056	0.144
<b>Shapiro-Wilk</b>	0.035	0.912	<b>Shapiro-Wilk</b>	0.03	0.324
<b><i>p</i>-value</b>	0.431	0.38	<b><i>p</i>-value</b>	0.052	0.634

\* Bold and italics represent statistical significance.

### 3.4 Deep learning outperformed CTAn using a different model architecture

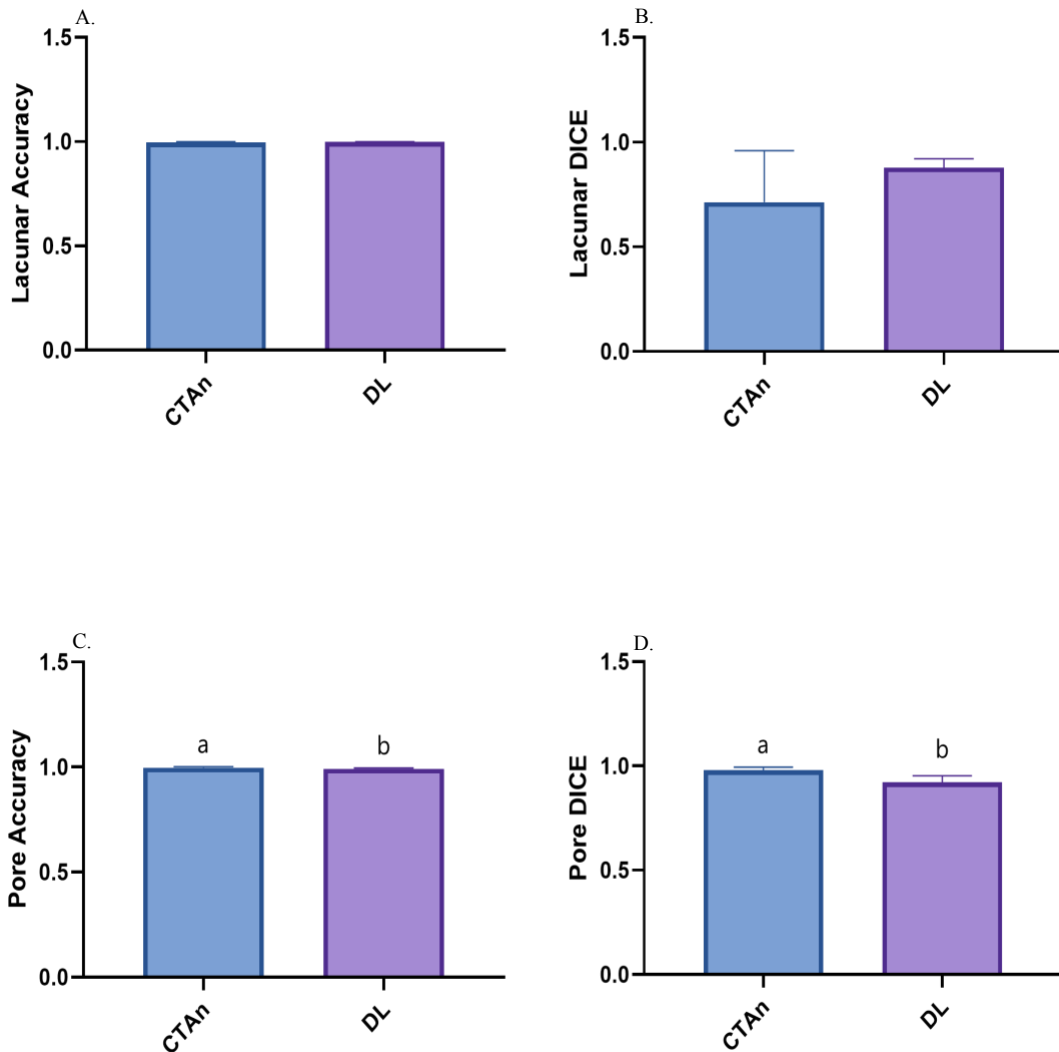
Noticeable improvements could be made to the original U-Net++ model architecture. Further, more model architectures were tested to find out if a different model architecture could perform better than U-Net++. During the initial testing, only one model architecture appeared to be slightly better than U-Net++, the multiscale attention network (MA-Net)<sup>106</sup>. Comparing DICE and accuracy scores (**Table 3.9**) for these two networks revealed MA-Net and U-Net++ were comparable with some comparisons favoring one network over the other. However, when it comes to normalization and normalization plus denoising, MA-Net had a higher DICE score than U-Net++ (0.914 and 0.652, and 0.929 and 0.829, respectively). Thus, further testing with MA-Net was conducted to see if it outperformed CTAn where its predecessor U-Net++ failed.



**Table 3.9.** DICE and Accuracy scores calculated between U-Net++ and MA-Net

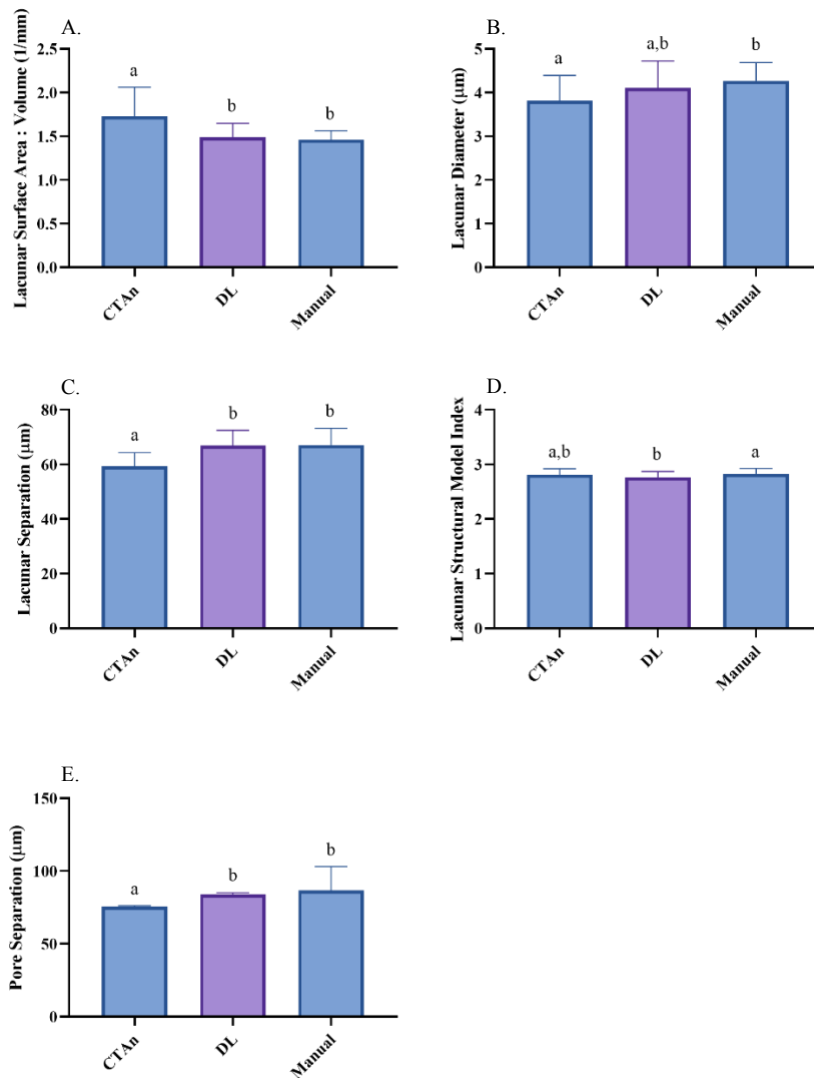
Parameter Test	U-Net++		MA-Net	
	Accuracy	DICE	Accuracy	DICE
Default	0.99309	0.91712	0.99371	0.9212
Normalization	0.9843	0.6517	0.99324	0.9140
Normalization + Calibration	0.99563	0.94857	0.99485	0.9402
Bilateral Smoothing Filter + Normalization	0.99418	0.9285	0.99402	0.9253
Denoising (Mean Shift Smoothing Filter) + Normalization	0.98883	0.82867	0.99433	0.9290

Similar to the comparisons made with U-Net++ and CTAn, lacunar and pore morphometric data, along with DICE and accuracy scores were used to determine if MA-Net was better than CTAn. Accuracy and DICE scores showed that CTAn outperform deep learning's segmentation in porosity significantly (**Figure 3.8**)<sup>107</sup>. The deep learning DICE and accuracy scores, while significantly different, still averaged 0.92 and 0.99, respectively. These scores are indicative of a highly successful segmentation. However, the lacunar segmentation showed no significant difference between CTAn and deep learning. Despite this, CTAn had a greater standard error than deep learning. The comparison of morphometric variables reveals a different trend. CTAn's segmentation differed from the manual segmentation in lacunar surface area to volume ratio, lacunar diameter, lacunar separation, and pore separation; meanwhile, the MA-Net architecture did not (**Figure 3.9**)<sup>107</sup>. MA-Net only differed from the manual segmentation in the lacunar structural model index.



**Figure 3.8.** Fourteen samples were segmented using deep learning, CTAn’s segmentation tools, and manually. Accuracy and DICE scores were extracted for the segmentations by comparing them to the manual segmentations. Accuracy is the quotient of the number of correct predictions to the total number of predictions. DICE is a direct measure of the similarity between the two segmentations. A score of 1.0 indicates the deep learning’s segmentation (or CTAn’s) is the exact same as the ground truth for accuracy and DICE scores. The letters above each bar represent their

group identifier. If the identifier differs from another group this indicates a significant difference from each other. For example, in pore DICE, CTAn is denoted by 'a' and deep learning is denoted by 'b'. CTAn is significantly different from deep learning. Graphs A and C are comparing the accuracy of the labeling of lacunae and pores by CTAn and deep learning when compared to the manual segmentation. Lacunar DICE comparisons did not reveal a significant difference (B), however, pore DICE scores are reportedly significant with CTAn having a higher score than deep learning (D).



**Figure 3.9.** Structural data was extracted from 14 samples using the manual CTAn, and deep learning segmentations. ANOVAs were used to test the difference between the groups. CTAn differed significantly from manual and deep learning in four comparisons (A, B, C, E). Conversely, CTAn only differed from deep learning once in the lacunar structural model index (D). In that variable, deep learning also differed from manual segmentation. Deep learning’s close association with the manual segmentation and CTAn’s significant deviation from it suggests that this deep

learning algorithm segmented the data more similarly to the manual segmentation indicating that it was more accurate than CTAn. The letters above each bar represent their group identifier. If the identifier differs from another group this indicates a significant difference from each other. For example, in pore separation, CTAn is denoted by 'a', and deep learning and manual are denoted by 'b'. CTAn is significantly different from deep learning and manual, however, deep learning and manual are not significantly different from each other.

## **4. Discussion**

This study implemented novel AI-based segmentation techniques to study the impact of prolonged opioid use on human bone microstructure. The microstructure was analyzed with high resolution synchrotron technology that allowed the visualization of osteocyte lacune and porous spaces. These parameters were used as proxies to determine bone health. Separately deep learning models (U-Net++ and MA-Net) were compared to manual and CTAn segmentations. The U-Net++ model was slightly worse than CTAn segmentations, but MA-Net outperformed both. However, U-Net++ was the fastest model to implement.

### **4.1 Synchrotron Radiation Micro Computed Tomography**

Employing synchrotron-based imaging techniques offers many benefits. For example, synchrotron radiation micro-computed tomography can image at higher resolutions than laboratory  $\mu$ CT with significantly improved throughput. SR $\mu$ CT can produce images with 1.5  $\mu$ m resolution, which is greater than the 5  $\mu$ m resolution that most laboratory  $\mu$ CT machines can achieve. Increasing the resolution shrinks the field of view, but 1.5  $\mu$ m is necessary as it is the minimum resolution needed to resolve osteocyte lacunae<sup>46</sup>. This compromise creates a resolution dependency<sup>108</sup>. The field of view must be partially sacrificed to achieve a high resolution to visualize the structures of interest. It should be noted that nano-computed tomography (nano-CT) machines can produce resolutions as minuscule as 400 nm<sup>109</sup>. However, the synchrotron can produce a full scan in minutes, and nano-CT produces a scan at a similar resolution in hours. More prolonged exposure to radiation increases the risk of radiation-induced damage, affecting the study results. Thus, SR $\mu$ CT imaging is the preferred imaging modality for this study.

## **4.2 Deep learning is comparable to traditional segmentation methods with quicker processing times**

Artificial intelligence has been around for decades but has recently seen an increase in popularity and usage due to the advent of deep learning. The most famous example of AI in recent times is ChatGPT (OpenAI). The full scope of AI has yet to be realized; however, various disciplines are working to incorporate AI into their research, including the medical and anthropological areas. Deep learning has been applied to attempt to automate the evaluation of bone mineral density<sup>110,111</sup>, fractures<sup>95</sup>, and trabecular bone architecture<sup>112</sup>. Using a convolutional neural network deep learning model resulted in significantly improved detection and diagnosis of osteoporosis<sup>110,111</sup>. Deep learning has seen similar results in fracture detection. One of the first studies, for example, did not use convolutional layers and achieved an accuracy of 94.3% in correctly labeled fractures<sup>95,113</sup>. Using convolutional neural networks, fracture detection outperformed general physicians and orthopedists and was comparable to senior radiologists<sup>95,114,115</sup>. Implementing deep learning alongside medical professionals has proven helpful in fracture detection<sup>95,116</sup>.

AI segmentation has recently been implemented to segment osteons in cortical bone microstructure. Littek and colleagues (2023) used deep learning to segment intact and fragmentary osteons. Intact osteons had 90% of their borders, and fragmentary osteons were defined as having more than 10% of canals within their border<sup>94</sup>. The model achieved a DICE score of 0.73 for intact osteons, however, it only managed a 0.38 DICE score for fragmentary osteons<sup>94</sup>. The segmentation of fragmentary osteons was far too inconsistent for reliable use. Perhaps deep learning could perform more reliably with refinement or an alternative model. To my knowledge, the current

study is the first to implement deep learning in the image segmentation of cortical bone microstructure in SR $\mu$ CT data. One sample from this data typically has more than 2,000 images, making it impossible to manually segment all slices within a reasonable time frame. Previously, these data were segmented using thresholding, despeckling, and closing in CTAn. However, these tools struggle because they do not allow for manual correction and often fail to accurately segment the edges of lacunae and pores. Deep learning was presented as a possible more time-efficient and accurate method of segmenting the images.

The data revealed that CTAn was closer to the manual segmentation in lacunar and pore morphometric variables than deep learning. The deep learning U-Net++ model significantly differed from manual segmentation in four cases, where CTAn was different from manual in one case. However, the DICE and TPR scores contradict these findings. When these scores between the deep learning model and CTAn were compared, they did not differ significantly. The average DICE scores were comparable for lacunae (CTAn – 0.668, U-Net++ – 0.599) and pores (CTAn – 0.815, U-Net++ – 0.807)<sup>117</sup>. True positive rate values support CTAn over U-Net++ for lacunae (0.849 and 0.543, respectively) but support U-Net++ for pores (0.839 and 0.835, respectively)<sup>117</sup>. Overall, the data supports a comparable performance between the two segmentation methods, with U-Net++ performing slightly worse.

There are two critical caveats in this work: 1) there were no morphological tools applied to the U-Net++ results that can dramatically increase the model's performance, especially the TPR for lacunae, which could likely be increased with a simple filter to filter out artifacts labeled as lacunae



based on their size, and 2) the time required to achieve the segmentation. While time was not actively measured, the time required to apply the model is less than that required to design and apply a set of operations via CTAn. Additionally, the time spent is different; in CTAn, the person has to manually monitor and adjust the segmentation. With the deep learning model, the computer handles the rest after setup, allowing the researcher to complete other pertinent tasks. This model could likely be improved using morphological operations, primarily through the exclusion of artifacts incorrectly identified as lacunae.

A follow-up to the U-Net++ model was conducted to see if there was a better model architecture. MA-Net was the only other model that performed the segmentation accurately. MA-Net had better DICE scores when normalization was applied<sup>107</sup>. Normalization was the only factor that had a substantial impact on the reported DICE scores, so MA-Net was concluded to be a better model for the segmentation of bone microstructure. MA-Net was further used to determine if it was better than the CTAn protocol. Pore DICE and accuracy scores were significantly better in CTAn, however, both segmentation models reported scores in the 90% range. Specifically, the accuracy scores only differed from each other by 0.0057%. While statistical significance is observed and reported, the actual impact on the success and reliability of the segmentation is negligible. A better contribution to the comparison is analyzing the lacunar DICE scores. For CTAn, the scores ranged from 0.286681 – 0.96332 and MA-Net ranged from 0.794538 – 0.946417. Overall, the ranges for both segmentation methods are concerning. The use of MA-Net has a better distribution and will likely provide a more accurate segmentation for lacunae than CTAn. Additionally, in morphometric variables, MA-Net was significantly better than CTAn as it was more consistent

with the manual segmentation. This further supports the use of deep learning models in image segmentation and highlighted a promising potential to improve its efficacy.

### **4.3 Age is the strongest predictor of deteriorating bone health followed by sex**

The nonparametric tests revealed age as a significant predictor in percent lacunar volume, percent lacunar surface area, lacunar surface area volume ratio, lacunar surface density, lacunar diameter, lacunar separation, lacunar degree of anisotropy, lacunar number density, percent pore volume, percent pore surface area, pore surface to volume ratio, pore diameter, pore separation. Thirty-nine significant interactions were identified where age was the only variable. Additionally, only 10 out of 133 (~8%) significant interactions did not have age as a significant variable. Age is one of the most significant, if not essential, factors for deteriorating bone health (**Figure 3.1**). It has been postulated that humans reach skeletal maturity by the third decade of life, after which bone resorption tends to outpace bone formation, leading to increased bone loss. However, aging can affect multiple systems, including the levels of sex hormones.

The most exaggerated example of this is menopause in females, which leads to a substantial decline in estradiol. As described in **section 1.4** and summarized in **Figure 1.5**, estradiol modulates the release of OPG and RANKL to prevent the accumulation of osteoclasts, subsequently protecting bone health. Menopause is a significant reason that fractures are more common in older females than older males. Thus, there should be an expected difference in bone health between older females and males. This study's results differ as a significant difference was not discovered between the older sexes. The evidence of only sex playing a factor in this study was between males

and females in their 20s for percent lacunar surface area and in their 50s for lacunar degree of anisotropy. Sex is perceived to be integral in an additional 58 interactions (**Figure 3.7**). Regardless, both sexes are more likely to experience a fracture as they age than their younger counterparts.

One of the most well-studied phenomena in bone biology is the aging process. Over a century ago, Todd<sup>118</sup> described the macroscopic changes to the pubic bone regarding age and sex. Since then, the field exploded with hundreds of articles describing macroscopic changes to bone and the attention turning to microstructural bone alterations. Most literature agrees that bone mineral density and bone mineral content increase until the mid-thirties when a gradual shift to declining bone health is noticed<sup>15,119–126</sup> at various skeletal sites (e.g., lumbar spine, hip, forearm). Chen and colleagues (2013) reported a decrease of 70% in volumetric bone mineral density between 40-70 years of age, with similar decreases in BV/TV at the femoral neck (20%) between 60-90 years old. However, the radius appeared more resistant to aging, with only a 27% decrease in BV/TV over 70 years<sup>121</sup>. Nearly 40% of total trabecular bone loss is estimated to occur before 50, however, this differs dramatically from cortical bone (10%)<sup>127</sup>. This observation is explained by endosteal resorption of trabecular bone due to its high surface area and is more metabolically active than cortical bone<sup>15,122,123,128</sup>. Halloran and colleagues<sup>124</sup> reported a decrease in trabecular bone volume by 52%, marked by reductions in trabecular number, increases in trabecular separation, and structural model index (SMI). An increase in SMI indicates that the trabecular struts are more rod-like. This is significant because rod-like trabeculae are more susceptible to bending and buckling failures<sup>121</sup>. These findings were further corroborated by Russo and colleagues<sup>129</sup> who reported an age-associated decrease in lower total and trabecular bone density.

However, cortical bone comprises 80% of the adult skeleton<sup>15</sup>, so it is improbable that it will remain unaffected by the aging process. In fact, around the age of 50, a more rapid decline is reported and involves cortical bone<sup>119,125</sup>. The femoral diaphysis increased with age but was coupled with cortical thinning and decreased cortical area<sup>124,130</sup>. This study reports decreased lacunae and their surface area and volume with age. This is further made evident by the increased separation between lacunae and decreased surface density. These results are only apparent in the furthest age categories and suggest that age does not significantly impact cortical bone microstructure until the sixth decade, consistent with the literature on age-associated impacts on the cortical bone. The linear regressions for percent lacunar volume and lacunar surface area corroborate these findings with a decreasing trend (negative correlation) with age. One study found that cortical thickness decreased by 3-5% and cortical porosity increased by 31-33% per decade at the femoral neck between 60-90<sup>121</sup>. This led to a 2-fold increase in fracture risk every four years. Similarly, the radius showed increased cortical porosity and pore diameter with age and an associated decrease in cortical thickness<sup>121</sup>. Similarly, this study found that cortical porosity increased with age. Further, this study reported that the number of pores increased, and their separation decreased. The increasing pore volume and decreasing separation have been noted in previous studies<sup>2</sup>. They may indicate pore coalescence in a process called trabecularization, which is the transition of cortical bone to trabecular bone during aging<sup>131,132</sup>. Further evidence of this phenomenon is phenomenon a study where they indicated a decrease in cortical volumetric bone mineral density and cortical thickness, and an increase in cortical porosity and diameter, however, their trabecular parameters were healthier than their cortical ones in the older population at the ultra-distal radius<sup>133</sup>. Due to trabecularization and age-associated degeneration of bone, people

over 60 have an increase in incomplete osteons<sup>128</sup>. Twenty-five percent of the endosteal surface is actively involved in remodeling in individuals 70 and older<sup>128</sup>.

Several researchers have sought to determine the reason for the age-associated decline in bone health. A prevailing explanation is the disuse or ‘use it or lose it’ principle. This principle is more colloquially used to describe building and maintaining muscle. This is suitable because muscle and bone interaction (or lack thereof) may cause age-associated decline. More force is exerted on bone by muscle than by body weight, as the muscles need to generate two pounds of force to move one pound of body weight<sup>123</sup>. This is under normal conditions; however, athletes can sometimes briefly exert muscle force that is five times that of their body weight<sup>123</sup>. Muscle and bone loss becomes more rapid at 60 years of age<sup>120</sup>, and by 80, nearly 50% of muscle strength has dissipated, and bone mass may follow changes in bone strength<sup>123</sup>. Physical activity declines with age<sup>15,126</sup> in line with the age-associated decline in bone health. Some reports list it as an extrinsic factor in bone health<sup>122</sup>. Further muscle paralysis has been shown to exacerbate bone loss, possibly due to the release of irisin by muscle tissue, which interacts with estradiol to impact bone negatively<sup>122</sup>. Exercise is a possible treatment showing positive outcomes on bone health<sup>134</sup>, however, even ambulatory older females lose 1% of femoral bone annually<sup>135</sup>. There must be other contributing factors leading to age-associated bone fragility.

Several studies have analyzed hormonal and mineral fluctuations over the human lifespan and calculated their impact. Serum calcium decreases with age<sup>136</sup>, which stimulates the activation of vitamin D and parathyroid hormone (PTH). Vitamin D is responsible for maintaining calcium and

phosphorous intestinal absorption and retention in the kidneys. Parathyroid hormone stimulates osteoclasts to increase bone resorption and release calcium and phosphorus. Disrupting the balance of vitamin D and PTH can lead to increased bone resorption to restore calcium and phosphorus homeostasis. Aging disrupts this homeostasis with vitamin D significantly decreasing<sup>122</sup> and intact parathyroid hormone increasing (iPTH) after age 65<sup>15,136</sup>. Additionally, sclerostin increases nearly 3.5 times<sup>127</sup> with age. The *sost* gene and its product, sclerostin, are involved in osteoblast downregulation and decreased bone formation<sup>126</sup>. Aging also significantly impacts testosterone and estradiol levels. A preliminary study indicated a significant fall in the Free Androgen Index (FAI) in males<sup>137</sup>. A follow-up study reported a decrease in available testosterone by 64% and a 124% increase in sex hormone-binding globulin (SHBG)<sup>127</sup>. Estradiol also decreases with age, especially during menopause. Demontiero and colleagues (2012) reported an 87.5% decrease in estradiol and a 70% decrease in estrone, and this period can last for up to 10 years.

Researchers have analyzed the sex-related differences. Bone mineral density is increased in males compared to females at the lumbar spine, and with age, femoral sites decrease among the sexes, however, it is more pronounced in females with a bone loss rate twice that of males<sup>138</sup>. By 90, Kiebzak (1991) reported that females may lose 50% of peak trabecular bone mass while males will only lose 10-25%. Warming and colleagues (2002) analyzed the distal forearm, total hip, and lumbar spine, determining that peak BMD was 12-25% higher in males than females. Males had 35-42% more bone area than females<sup>127</sup>. Additionally, females experience significant bone loss in midlife, while it does not begin in males until 70-75 years<sup>127</sup>. Several studies indicate that females had significant bone loss between 50-59 during perimenopause<sup>119,127,139</sup>. Studies have shown that females have lower trabecular and cortical bone density<sup>121,122,129</sup>. The sex-related differences in

trabecular bone appear from females losing whole trabeculae while males' trabecular struts get thinner<sup>121,127</sup> and the trabecular number has a more significant impact on bone strength. Cortical vBMD and cortical thickness are lower in females than in males<sup>121</sup>. This study revealed that females have a higher lacunar surface area and degree of anisotropy than males, meaning their lacunae are oriented in different planes. When the linear regressions were split by sex it became evident that there was a more significant correlation between females and aging than males for percent lacunar volume and surface area. The use of hormone replacement therapy can markedly attenuate the effect of estradiol deficiency<sup>119</sup>. Several other factors can influence bone health, including genetics, alterations in cellular components, biochemical and vasculature status, nutrition, physical activity, medical conditions, and drugs<sup>122</sup>.

#### **4.4 Opioid use is not a significant predictor of LCN dysregulation**

Opioid use had few significant interactions (45/133) and fewer interactions (5/133) where it was the sole contributor. Lacunar surface area differed between control and opioid users for males in their 20s and 50s. Males in their 30s differed significantly based on opioid use for lacunar surface area to volume ratio and lacunar diameter. Males in their third decade of life and females in their 6<sup>th</sup> decade of life varied by opioid use in the lacunar degree of anisotropy (**Figure 3.3**). Additionally, multiple regressions revealed that opioid use dysregulated the normal aging process, as seen in the control group, possibly due to the overall lower values for percent lacunar volume and surface area. The trends observed in this study directly conflict with some of the available literature. Literature on opioid use trends suggests that older populations were more likely to have and refill opioid prescriptions than younger individuals<sup>140–143</sup>. Schieber and colleagues (2020) reported 2.6 times increase in prescriptions for opioids among patients 65 and older than 20-24 years old. The 55–64-year-old category had the highest prescriptions filled per person at four and

a half. The most common perceptible rationale reported for this trend was pain and the push by the American Pain Society to include pain as the fifth vital sign<sup>143,144</sup>. This corroborates the significant differences visualized in the older age categories in this study.

However, these trends do not support the differences seen in the younger age groups. The most probable cause for this is the use of illicit opioids. Heroin use in the United States has been rising since 2002<sup>145</sup>. Additionally, Park and colleagues (2020) reported that the significant sources of misused prescription opioids for younger individuals were from friends and relatives, while the primary source for older individuals was from physicians. Another contradiction with this study is several reports indicating that females had a higher prevalence of opioid use than males<sup>140,142,146</sup>. Again, it appears that this trend is from legal sources of opioids. Males have higher rates of heroin use than females<sup>145</sup> and males are more likely to get opioids from relatives, friends, and drug dealers than females<sup>141</sup>.

The literature suggests that opioids would produce a more exaggerated effect on bone quality than is represented in this study. One study found that 74.3% of opioid users have low bone mass, with 29% with osteoporosis and 48% with osteopenia<sup>147</sup>. Other studies found that opioid use is correlated to hypogonadism with 50%<sup>148</sup>, 85%<sup>149</sup>, and 87.5%<sup>150</sup> of opioid users having hypogonadism. Of the 85% of patients, 21% were diagnosed with osteoporosis, and 50% were diagnosed with osteopenia<sup>149</sup>. Methadone, a synthetic long-acting opioid, is commonly used to treat opioid addiction. Grey and colleagues (2011) reported that the dosage and duration of the prescription have increased due to improved outcomes for opioid users, however, there are several



concerns, including the development of osteoporosis. Studies have validated the concern for the development of osteoporosis. One study reported 97% of males and 75% of females having low DXA scores, with 61% of the males having osteoporosis and 54% of the females having osteopenia<sup>151</sup>. An Additional study on males on methadone treatment reported they had a lower BMD by one standard deviation, leading to an increased risk of fracture<sup>152</sup>. The results of this study may conflict with the existing literature due to the complex nature of humans and the several varying facets that affect bone health. In the study, 30 (60%) samples from the control group reported excessive tobacco and alcohol abuse. These substances can negatively affect bone health, similar to opioids. The extensive use of tobacco can cause hypogonadism and directly inhibit osteoblast production<sup>153,154</sup>. The literature surrounding alcohol use is conflicting mainly due to the variable and arbitrary definitions of alcohol consumption. However, the literature is consistent that heavy alcohol consumption negatively impacts bone health<sup>155-158</sup>.

Fortunately, the effects of opioid use can be counteracted through several interventions, including hormonal replacement therapy and exercise. In one study, 73% of males on testosterone supplements had normal bone mineral density, while the remaining 27% had osteopenia<sup>150</sup>. Eight months of aerobic exercise in young opioid-dependent females increased bone quality in all participants. The experimental group had a 32.8% increase in bone quality at the calcaneus<sup>134</sup>. These treatments have positive effects on both health and have provided evidence that they can reverse the effects of opioid abuse.

## 4.5 Limitations

Despite the utility of synchrotron analysis, it has several inherent limitations. There are only 23-member synchrotron facilities worldwide, all with competitive peer-review application processes for instrumental operating time. Even fewer synchrotrons offer the capabilities to complete biomedical research, including two in North America, one in Europe, and one in Asia. The Advanced Photon Source in the United States is undergoing substantial upgrades, leaving only three facilities worldwide. As a result of the scarcity of facilities and the high demand of potential users, allotted time at a facility is rare, competitive, and often requires expensive travel arrangements.

Additionally, due to the nature of X-rays ( $\mu$ CT and SR $\mu$ CT) and our sample processing techniques, the quantification of osteocytes is conducted indirectly through the measurement of their lacunae. However, the lacunae can be unoccupied. The percentage of filled lacunae varies with age, with a report indicating that 5-40% of lacunae are unoccupied<sup>83,84</sup>. Additionally, due to the radiation dose of SR $\mu$ CT at 1.5  $\mu$ m resolution, the experiment had to be *ex vivo*, sacrificing the context of an *in vivo* model.

Regardless, SR $\mu$ CT provides a wealth of invaluable knowledge into bone microstructure that is otherwise impossible without decreasing efficiency (nano-CT) or sacrificing the third dimension (confocal laser scanning microscopy and serial sectioning).

Another complicated yet necessary aspect of this study involves using human skeletal material. Humans, by nature, are multifaceted, with extensive and complex life histories. The donors involved in the study have complicated past medical records that must be clarified. Most medical information is received through questionnaires and relies on the donor or their next of kin's honesty, accurate recollection, and knowledge of the events. Sometimes, only the use of 'opiates' is reported, which makes analysis more troubling. An opiate is a peptide with analgesic properties<sup>60</sup> and represents a broad class of narcotics. However, different opiates can affect any of the three canonical receptors ( $\mu$ ,  $\kappa$ ,  $\delta$ ) and the OGFR differently and have different affinities for these receptors. For example, morphine targets the  $\mu$  receptor, but dezocine has a higher affinity than morphine for  $\mu$  and  $\kappa$  receptors<sup>159</sup>. Other examples of opiates include tapentadol, oxycodone, buprenorphine, hydromorphone fentanyl, and methadone. Tapentadol is a  $\mu$  receptor agonist and noradrenaline reuptake inhibitor, and hydromorphone is a semisynthetic opioid. Fentanyl is fully synthetic and 100 times more potent than morphine<sup>160</sup>. The varying types of opioids, their side effects, and the additional past medical information make unraveling the cause of bone degradation challenging. Surgeries and associated recovery drugs or diseases, such as chronic kidney disease, can additionally impact the skeletal system.

Other lifestyle factors complicate the interpretation of the results. For example, an opioid user may also be engaged in polysubstance use. In this study, the most common confounding substances reportedly used were tobacco and alcohol. At the same time, the directionality of alcohol's specific effect on the skeleton is shrouded by conflicting reports. All known reports suggest alcohol impacts the skeletal system<sup>155,156,158,161</sup>. Tobacco use diminishes bone quality directly and indirectly by modulation of osteoblastogenesis, inducing hypogonadism, reducing intestinal calcium

absorption, and increasing the ratio of RANKL to OPG<sup>153,162,163</sup>. Substance users are often associated with poor socio-economic status, which can affect their diet and exercise. Both are incredibly important for the maintenance and healthy aging of bone tissues.

Additionally, the questionnaires are collected at or near the time of death. This is a tumultuous time for the families and may inhibit an accurate recollection of the events. Additionally, the staff has to deal with death and suffering families daily. The healthcare system was pushed to the brink of collapse amidst the global COVID-19 pandemic<sup>164,165</sup>. The taxing workload of healthcare workers has them struggling to maintain their mental health<sup>166</sup>. Given their immense workload and emotionally stressful positions, it is probable that they will make mistakes.

Drug addiction is the most heavily stigmatized condition internationally<sup>167</sup>, but there are further stigmatized conditions that are often associated with drug addiction. Joblessness, homelessness, and unkemptness are heavily stigmatized qualities worldwide, and drug-addicted persons can often find themselves associated with these categories<sup>167</sup>. Similarly, surveys have reported that people believe that those suffering from drug addiction (legal or illegal) should have lower priority in the healthcare system<sup>168</sup> and are often receiving inferior healthcare<sup>169-172</sup>. Additionally, fear of stigmatization can cause people to avoid seeking medical care<sup>170</sup> or hiding their opioid use entirely<sup>173,174</sup>. As a result, the accuracy of the information on their opioid use is questionable.

An ongoing live animal study in the Andronowski Lab seeks to control for several of these confounding factors. New Zealand White rabbits will be administered subcutaneous injections of

low or high-dose morphine and fentanyl. The rabbits will be under the same living conditions with food and water *ad libitum* and a designated amount of time for enrichment. The serum will be analyzed to ensure total administration of the opioids and to test hormone levels. This study seeks to reveal key morphological distinctions between the opioid groups and the controls.

## 5. Conclusions

The skeletal system is a crucial component to several critical human functions, including protecting the internal organs, acting as scaffolding for movement, and production of red blood cells. Similar to other systems, various pathologies exist that can impair the bone's ability to function. One such pathology, osteoporosis, afflicts millions of people worldwide and the incidence of this debilitating disease is only set to increase. It is marked by increased resorption cavities and reduced cortical and trabecular bone. The resulting brittle bone is more susceptible to fractures leading to complicated recoveries. Age, diet, disease, and exercise are a few risk factors for the development of osteoporosis. Some drugs (pharmaceutical and illicit) have been implicated as additional risk factors (e.g., opioids, alcohol, tobacco). Opioids inhibit osteoblastogenesis, sex hormone production, and cognitive function leading to an increased risk of osteoporosis.

This work sought to evaluate the impacts of the opioid exposure microstructural bone health in humans. Utilizing SR $\mu$ CT, osteocyte lacunae and resorption spaces were the primary targets of investigation. To increase efficiency of image analysis, a novel deep learning algorithm was employed to semi-automatically segment all datasets. However, no significant trends were established between bone health and opioid use likely due to the multifactorial nature of the human specimens. A follow-up study is being conducted using a rabbit model to control for most confounding variables, including activity, diet, amount and timing of opioid administration. Further, fluorochrome injections will allow the tracking of bone remodeling over time. Despite the results of this study, the deep learning algorithm employed demonstrated comparable performance to established segmentation methods. This suggests a use for it in the future of data acquisition in SR $\mu$ CT and other imaging modalities.

## 6. References

1. Oury, F. *et al.* Endocrine Regulation of Male Fertility by the Skeleton. *Cell* **144**, 796–809 (2011). doi: 10.1016/j.cell.2011.02.004
2. Andronowski, J. M. *et al.* A multimodal 3D imaging approach of pore networks in the human femur to assess age-associated vascular expansion and Lacuno-Canalicular reduction. *Anat Rec (Hoboken)* **306**, 475–493 (2023). doi: 10.1002/ar.25089
3. Boabaid, F., Cerri, P. S. & Katchburian, E. Apoptotic bone cells may be engulfed by osteoclasts during alveolar bone resorption in young rats. *Tissue and Cell* **33**, 318–325 (2001). doi: 10.1054/tice.2001.0179
4. Frost, H. M. Tetracycline-Based Histological Analysis of Bone Remodeling. *Calc. Tis Res.* **3**, 211–237 (1969). doi: 10.1007/BF02058664
5. Robling, A. G., Castillo, A. B. & Turner, C. H. BIOMECHANICAL AND MOLECULAR REGULATION OF BONE REMODELING. *Annu. Rev. Biomed. Eng.* **8**, 455–498 (2006). doi: 10.1146/annurev.bioeng.8.061505.095721
6. Boskey, A. L. & Coleman, R. Aging and Bone. *J Dent Res* **89**, 1333–1348 (2010). doi: 10.1177/0022034510377791
7. Murshed, M. Mechanism of Bone Mineralization. *Cold Spring Harb Perspect Med* **8**, a031229 (2018). doi: 10.1101/cshperspect.a031229
8. Watson, R., Turley, R. & Gersten, T. What Are White Blood Cells? - Health Encyclopedia - University of Rochester Medical Center.  
<https://www.urmc.rochester.edu/encyclopedia/content.aspx?ContentID=35&ContentTypeID=160> (2023).

9. Brandi, M. L. Microarchitecture, the key to bone quality. *Rheumatology* **48**, iv3–iv8 (2009). doi: 10.1093/rheumatology/kep273
10. Weiner, S. & Traub, W. Bone structure: from ångstroms to microns. *FASEB j.* **6**, 879–885 (1992). doi: 10.1096/fasebj.6.3.1740237
11. Greitz-Miller, R. & Frisch, F. Issues In-Depth: Making some bones about it. *Science Scope* **031**, 7 (2007).
12. Stewart, H. L. & Kawcak, C. E. The Importance of Subchondral Bone in the Pathophysiology of Osteoarthritis. *Front. Vet. Sci.* **5**, 178 (2018). doi: 10.3389/fvets.2018.00178
13. MacConaill, M. A. THE MOVEMENTS OF BONES AND JOINTS: 5. The Significance of Shape. *The Journal of Bone and Joint Surgery. British volume* **35-B**, 290–297 (1953). doi: 10.1302/0301-620X.35B2.290
14. Gilroy, A. M., Voll, M. & Wesker, K. *Anatomy: An Essential Textbook*. (Thieme, New York, 2021).
15. Kiebzak, G. M. Age-related bone changes. *Experimental Gerontology* **26**, 171–187 (1991). doi: 10.1016/0531-5565(91)90010-J
16. Renders, G. A. P., Mulder, L., Van Ruijven, L. J. & Van Eijden, T. M. G. J. Porosity of human mandibular condylar bone. *Journal of Anatomy* **210**, 239–248 (2007). doi: 10.1111/j.1469-7580.2007.00693.x
17. Martin, R. B., Burr, D. B., Sharkey, N. A. & Fyhrie, D. P. *Skeletal Tissue Mechanics*. (Springer, New York, 2015).
18. Currey, J. D. *Bones: Structure and Mechanics*. (Princeton University Press, Princeton, NJ, 2002).



19. Gao, M. *et al.* Capacitive deionization toward fluoride elimination: Selective advantage, state of the art, and future perspectives. *Desalination* **577**, 117392 (2024). doi: 10.1016/j.desal.2024.117392
20. Florencio-Silva, R., Sasso, G. R. da S., Sasso-Cerri, E., Simões, M. J. & Cerri, P. S. Biology of Bone Tissue: Structure, Function, and Factors That Influence Bone Cells. *BioMed Research International* **2015**, 1–17 (2015). doi: 10.1155/2015/421746
21. Dallas, S. L., Prideaux, M. & Bonewald, L. F. The Osteocyte: An Endocrine Cell ... and More. *Endocrine Reviews* **34**, 658–690 (2013). doi: 10.1210/er.2012-1026
22. Zhang, Y. *et al.* A program of microRNAs controls osteogenic lineage progression by targeting transcription factor Runx2. *Proc. Natl. Acad. Sci. U.S.A.* **108**, 9863–9868 (2011). doi: 10.1073/pnas.1018493108
23. Ducy, P., Zhang, R., Geoffroy, V., Ridall, A. L. & Karsenty, G. Osf2/Cbfa1: A Transcriptional Activator of Osteoblast Differentiation. *Cell* **89**, 747–754 (1997). doi: 10.1016/S0092-8674(00)80257-3
24. Komori, T. *et al.* Targeted Disruption of Results in a Complete Lack of Bone Formation owing to Maturation Arrest of Osteoblasts. *Cell* **89**, 755–764 (1997). doi: 10.1016/S0092-8674(00)80258-5
25. Xiong, J. *et al.* Matrix-embedded cells control osteoclast formation. *Nat Med* **17**, 1235–1241 (2011). doi: 10.1038/nm.2448
26. Nakashima, T. *et al.* Evidence for osteocyte regulation of bone homeostasis through RANKL expression. *Nat Med* **17**, 1231–1234 (2011). doi: 10.1038/nm.2452
27. Ming, J., Cronin, S. J. F. & Penninger, J. M. Targeting the RANKL/RANK/OPG Axis for Cancer Therapy. *Front. Oncol.* **10**, 1283 (2020). doi: 10.3389/fonc.2020.01283

28. Seyfried, O. & Hester, J. Opioids and endocrine dysfunction. *British Journal of Pain* **6**, 17–24 (2012). doi: 10.1177/2049463712438299
29. Currey, J. D. *Bones: Structure and Mechanics*. (Princeton Univ. Press, Princeton, NJ, 2006).
30. Lin, K. & Chang, J. Structure and properties of hydroxyapatite for biomedical applications. in *Hydroxyapatite (Hap) for Biomedical Applications* 3–19 (Elsevier, 2015). doi: 10.1016/B978-1-78242-033-0.00001-8.
31. Martin, R. B., Burr, D. B., Sharkey, N. A. & Fyhrie, D. P. *Skeletal Tissue Mechanics*. (Springer New York, New York, NY, 2015). doi: 10.1007/978-1-4939-3002-9.
32. Carpenter, T. O. *et al.* Rickets. *Nat Rev Dis Primers* **3**, 17101 (2017). doi: 10.1038/nrdp.2017.101
33. Forlino, A. & Marini, J. C. Osteogenesis imperfecta. *The Lancet* **387**, 1657–1671 (2016). doi: 10.1016/S0140-6736(15)00728-X
34. Miller, S. C., de Saint-Georges, L., Bowman, B. M. & Jee, W. S. Bone lining cells: structure and function. *Scanning Microsc* **3**, 953–960; discussion 960-961 (1989).
35. Andronowski, J. M., Crowder, C. & Soto Martinez, M. Recent advancements in the analysis of bone microstructure: new dimensions in forensic anthropology. *Forensic Sciences Research* **3**, 294–309 (2018). doi: 10.1080/20961790.2018.1483294
36. Andronowski, J. M. & Cole, M. E. Current and emerging histomorphometric and imaging techniques for assessing age-at-death and cortical bone quality. *WIREs Forensic Science* **3**, e1399 (2021). doi: 10.1002/wfs2.1399

37. Boyce, B. F. & Xing, L. Functions of RANKL/RANK/OPG in bone modeling and remodeling. *Archives of Biochemistry and Biophysics* **473**, 139–146 (2008). doi: 10.1016/j.abb.2008.03.018
38. Boyce, B., Yao, Z. & Xing, L. Osteoclasts Have Multiple Roles in Bone in Addition to Bone Resorption. *Crit Rev Eukar Gene Expr* **19**, 171–180 (2009). doi: 10.1615/CritRevEukarGeneExpr.v19.i3.10
39. Cerri, P. S., Boabaid, F. & Katchburian, E. Combined TUNEL and TRAP methods suggest that apoptotic bone cells are inside vacuoles of alveolar bone osteoclasts in young rats: *Apoptotic bone cells inside osteoclasts. Journal of Periodontal Research* **38**, 223–226 (2003). doi: 10.1034/j.1600-0765.2003.02006.x
40. Porter, J. L. & Varacallo, M. Osteoporosis. in *StatPearls* (StatPearls Publishing, Treasure Island (FL), 2023).
41. Tański, W., Kosiorowska, J. & Szymańska-Chabowska, A. Osteoporosis – risk factors, pharmaceutical and non-pharmaceutical treatment. *European Review for Medical and Pharmacological Sciences* **25**, 3557–3566 (2021). doi: 10.26355/eurrev\_202105\_25838
42. Zhou, B. *et al.* High-resolution peripheral quantitative computed tomography (HR-pQCT) can assess microstructural and biomechanical properties of both human distal radius and tibia: Ex vivo computational and experimental validations. *Bone* **86**, 58–67 (2016). doi: 10.1016/j.bone.2016.02.016
43. Fang, H. *et al.* The Mechanism of Bone Remodeling After Bone Aging. *CIA Volume* **17**, 405–415 (2022). doi: 10.2147/CIA.S349604
44. Lane, N. E. Epidemiology, etiology, and diagnosis of osteoporosis. *American Journal of Obstetrics and Gynecology* **194**, S3–S11 (2006). doi: 10.1016/j.ajog.2005.08.047

45. Bala, Y., Zebaze, R. & Seeman, E. Role of cortical bone in bone fragility. *Curr Opin Rheumatol* **27**, 406–413 (2015). doi: 10.1097/BOR.000000000000183
46. Hannah, K. M., Thomas, C. D. L., Clement, J. G., De Carlo, F. & Peele, A. G. Bimodal distribution of osteocyte lacunar size in the human femoral cortex as revealed by micro-CT. *Bone* **47**, 866–871 (2010). doi: 10.1016/j.bone.2010.07.025
47. United Nations publication. *World Drug Report 2021*. (Sales No. E.21.XI.8, 2021).
48. Krinsky, C. S., Lathrop, S. L., Crossey, M., Baker, G. & Zumwalt, R. A Toxicology-Based Review of Fentanyl-Related Deaths in New Mexico (1986–2007). *American Journal of Forensic Medicine & Pathology* **32**, 347–351 (2011). doi: 10.1097/PAF.0b013e31822ad269
49. Stanley, T. H. The Fentanyl Story. *The Journal of Pain* **15**, 1215–1226 (2014). doi: 10.1016/j.jpain.2014.08.010
50. Garriott, J. C., Rodriguez, R. & Di Maio, V. J. M. A Death from Fentanyl Overdose. *Journal of Analytical Toxicology* **8**, 288–289 (1984). doi: 10.1093/jat/8.6.288
51. Stockwell, T. *et al.* *Canadian Substance Use Costs and Harms 2015-2017*. (Canadian Centre on Substance Use and Addiction, Ottawa, Ont., 2020).
52. Canadian Institute for Health Information. Opioid Prescribing in Canada: How Are Practices Changing? 42 (2019).
53. Coluzzi, F., Pergolizzi, J., Raffa, R. B. & Mattia, C. The unsolved case of ‘bone-impairing analgesics’: the endocrine effects of opioids on bone metabolism. *Ther Clin Risk Manag* **11**, 515–23 (2015). doi: 10.2147/TCRM.S79409
54. Henderson, G. L. Fentanyl-Related Deaths: Demographics, Circumstances, and Toxicology of 112 Cases. *J. Forensic Sci.* **36**, 13045J (1991). doi: 10.1520/JFS13045J

55. Canadian Centre on Substance Use and Addiction. Prescription Opioids (Canadian Drug Summary) | Canadian Centre on Substance Use and Addiction.  
<https://www.ccsa.ca/prescription-opioids-canadian-drug-summary> (2020).
56. Special Advisory Committee on the Epidemic of Opioid Overdoses. Opioid- and Stimulant-related Harms in Canada. (2022).
57. Public Health Agency of Canada. Modelling opioid-related deaths during the COVID-19 outbreak. (2022).
58. Edwards, K. A. *et al.* A Kappa Opioid Receptor Agonist Blocks Bone Cancer Pain Without Altering Bone Loss, Tumor Size, or Cancer Cell Proliferation in a Mouse Model of Cancer-Induced Bone Pain. *The Journal of Pain* **19**, 612–625 (2018). doi: 10.1016/j.jpain.2018.01.002
59. Boshra, V. Evaluation of Osteoporosis Risk Associated with Chronic Use of Morphine, Fentanyl and Tramadol in Adult Female Rats.  
<https://www.ingentaconnect.com/content/ben/cds/2011/00000006/00000003/art00006>  
(2011) doi: 10.2174/157488611797579267
60. Tanaka, K., Kondo, H., Hamamura, K. & Togari, A. Systemic administration of low-dose naltrexone increases bone mass due to blockade of opioid growth factor receptor signaling in mice osteoblasts. *Life Sciences* **224**, 232–240 (2019). doi: 10.1016/j.lfs.2019.03.069
61. Thakur, N. A., DeBoyace, S. D. & Margulies, B. S. Antagonism of the Met5-enkephalin-opioid growth factor receptor-signaling axis promotes MSC to differentiate into osteoblasts: ANTAGONISM OF OGFR BY NALOXONE INCREASES BONE FORMATION. *J. Orthop. Res.* **34**, 1195–1205 (2016). doi: 10.1002/jor.23135

62. Meleger, A. L., Froude, C. K. & Walker, J. Nutrition and Eating Behavior in Patients With Chronic Pain Receiving Long-Term Opioid Therapy. *PM&R* **6**, 7-12.e1 (2014). doi: 10.1016/j.pmrj.2013.08.597
63. Wiss, D. A. A Biopsychosocial Overview of the Opioid Crisis: Considering Nutrition and Gastrointestinal Health. *Front. Public Health* **7**, 193 (2019). doi: 10.3389/fpubh.2019.00193
64. Meng, J. *et al.* Morphine Induces Bacterial Translocation in Mice by Compromising Intestinal Barrier Function in a TLR-Dependent Manner. *PLoS ONE* **8**, e54040 (2013). doi: 10.1371/journal.pone.0054040
65. Banerjee, S. *et al.* Opioid-induced gut microbial disruption and bile dysregulation leads to gut barrier compromise and sustained systemic inflammation. *Mucosal Immunology* **9**, 1418–1428 (2016). doi: 10.1038/mi.2016.9
66. Lee, K. *et al.* The gut microbiota mediates reward and sensory responses associated with regimen-selective morphine dependence. *Neuropsychopharmacol* **43**, 2606–2614 (2018). doi: 10.1038/s41386-018-0211-9
67. Benyamin, R. *et al.* Opioid complications and side effects. *Pain Physician* **11**, S105-120 (2008).
68. Jain, N. *et al.* Opioids delay healing of spinal fusion: a rabbit posterolateral lumbar fusion model. *The Spine Journal* **18**, 1659–1668 (2018). doi: 10.1016/j.spinee.2018.04.012
69. Dempster, D. W. *et al.* Standardized nomenclature, symbols, and units for bone histomorphometry: a 2012 update of the report of the ASBMR Histomorphometry Nomenclature Committee. *J. Bone Miner. Res.* **28**, 2–17 (2013). doi: 10.1002/jbmr.1805

70. Parfitt, A. M. *et al.* Bone histomorphometry: standardization of nomenclature, symbols, and units. Report of the ASBMR Histomorphometry Nomenclature Committee. *J Bone Miner Res* **2**, 595–610 (1987). doi: 10.1002/jbmr.5650020617
71. Schindelin, J. *et al.* Fiji: an open-source platform for biological-image analysis. *Nature Methods* **9**, 676–682 (2012). doi: 10.1038/nmeth.2019
72. Ma, S. *et al.* Synchrotron Imaging Assessment of Bone Quality. *Clinic Rev Bone Miner Metab* **14**, 150–160 (2016). doi: 10.1007/s12018-016-9223-3
73. Canadian Light Source. *The Canadian Light Source*  
<https://www.lightsource.ca/public/what-is-a-synchrotron.php#Overview> (2023).
74. Thomlinson, W., Suortti, P. & Chapman, D. Recent advances in synchrotron radiation medical research. *Nuclear Instruments and Methods in Physics Research Section A: Accelerators, Spectrometers, Detectors and Associated Equipment* **543**, 288–296 (2005). doi: 10.1016/j.nima.2005.01.243
75. Dallin, L. *et al.* Canadian Light Source Status and Commissioning Results. (2004). doi: 10.1109/PAC.2003.1288884
76. Wysokinski, T. W. *et al.* Beamlines of the Biomedical Imaging and Therapy Facility at the Canadian Light Source - Part 2. *J. Phys.: Conf. Ser.* **425**, 072013 (2013). doi: 10.1088/1742-6596/425/7/072013
77. Grochulski, P. *et al.* Review of Canadian Light Source facilities for biological applications. *Nuclear Instruments and Methods in Physics Research Section B: Beam Interactions with Materials and Atoms* **411**, 17–21 (2017). doi: 10.1016/j.nimb.2017.01.065
78. Wysokinski, T. W. *et al.* Beamlines of the biomedical imaging and therapy facility at the Canadian light source—Part 1. *Nuclear Instruments and Methods in Physics Research*

*Section A: Accelerators, Spectrometers, Detectors and Associated Equipment* **582**, 73–76 (2007). doi: 10.1016/j.nima.2007.08.087

79. Wysokinski, T. W. *et al.* BMIT facility at the Canadian Light Source: Advances in X-ray phase-sensitive imaging. *Physica Medica* **32**, 1753–1758 (2016). doi: 10.1016/j.ejmp.2016.07.090
80. Akhter, M. P. & Recker, R. R. High resolution imaging in bone tissue research-review. *Bone* **143**, 115620 (2021). doi: 10.1016/j.bone.2020.115620
81. Andronowski, J. M., Mundorff, A. Z., Pratt, I. V., Davoren, J. M. & Cooper, D. M. L. Evaluating differential nuclear DNA yield rates and osteocyte numbers among human bone tissue types: A synchrotron radiation micro-CT approach. *Forensic Science International: Genetics* **28**, 211–218 (2017). doi: 10.1016/j.fsigen.2017.03.002
82. Carter, Y., Suchorab, J. L., Thomas, C. D. L., Clement, J. G. & Cooper, D. M. L. Normal variation in cortical osteocyte lacunar parameters in healthy young males. *Journal of Anatomy* **225**, 328–336 (2014). doi: 10.1111/joa.12213
83. Carter, Y., Thomas, C. D. L., Clement, J. G. & Cooper, D. M. L. Femoral osteocyte lacunar density, volume and morphology in women across the lifespan. *Journal of Structural Biology* **183**, 519–526 (2013). doi: 10.1016/j.jsb.2013.07.004
84. Carter, Y. *et al.* Variation in osteocyte lacunar morphology and density in the human femur—a synchrotron radiation micro-CT study. *Bone* **52**, 126–32 (2013). doi: 10.1016/j.bone.2012.09.010
85. Cooper, D. M. L. *et al.* Visualization of 3D osteon morphology by synchrotron radiation micro-CT. *J. Anat.* **219**, 481–489 (2011). doi: 10.1111/j.1469-7580.2011.01398.x



86. Janna M Andronowski. Evaluating Differential Nuclear DNA Yield Rate Among. (The University of Tennessee, Knoxville, TN, 2016).
87. Schneider, P. *et al.* Simultaneous 3D visualization and quantification of murine bone and bone vasculature using micro-computed tomography and vascular replica. *Microsc. Res. Tech.* **72**, 690–701 (2009). doi: 10.1002/jemt.20720
88. Rusk, N. Deep learning. *Nat Methods* **13**, 35–35 (2016). doi: 10.1038/nmeth.3707
89. Ronneberger, O., Fischer, P. & Brox, T. U-Net: Convolutional Networks for Biomedical Image Segmentation. in *Medical Image Computing and Computer-Assisted Intervention - MICCAI 2015* vol. 3 234–241 (Springer, Munich, Germany, 2015).
90. Milletari, F., Navab, N. & Ahmadi, S.-A. V-Net: Fully Convolutional Neural Networks for Volumetric Medical Image Segmentation. in *2016 Fourth International Conference on 3D Vision (3DV)* 565–571 (IEEE, Stanford, CA, USA, 2016). doi:10.1109/3DV.2016.79. doi: 10.1109/3DV.2016.79
91. Zhou, Z., Rahman Siddiquee, M. M., Tajbakhsh, N. & Liang, J. UNet++: A Nested U-Net Architecture for Medical Image Segmentation. in *Deep Learning in Medical Image Analysis and Multimodal Learning for Clinical Decision Support* (eds. Stoyanov, D. et al.) vol. 11045 3–11 (Springer International Publishing, Cham, 2018).
92. Larson, D. B. *et al.* Performance of a Deep-Learning Neural Network Model in Assessing Skeletal Maturity on Pediatric Hand Radiographs. *Radiology* **287**, 313–322 (2018). doi: 10.1148/radiol.2017170236
93. Lea, W. W. *et al.* External validation of deep learning-based bone-age software: a preliminary study with real world data. *Sci Rep* **12**, 1232 (2022). doi: 10.1038/s41598-022-05282-z

94. Littek, A. *et al.* Automatic Segmentation of Osteonal Microstructure in Human Cortical Bone Using Deep Learning: A Proof of Concept. *Biology* **12**, 619 (2023). doi: 10.3390/biology12040619
95. Tanzi, L., Vezzetti, E., Moreno, R. & Moos, S. X-Ray Bone Fracture Classification Using Deep Learning: A Baseline for Designing a Reliable Approach. *Applied Sciences* **10**, 1507 (2020). doi: 10.3390/app10041507
96. Lee, J. H., Kim, Y. J. & Kim, K. G. Bone age estimation using deep learning and hand X-ray images. *Biomed. Eng. Lett.* **10**, 323–331 (2020). doi: 10.1007/s13534-020-00151-y
97. Spampinato, C., Palazzo, S., Giordano, D., Aldinucci, M. & Leonardi, R. Deep learning for automated skeletal bone age assessment in X-ray images. *Medical Image Analysis* **36**, 41–51 (2017). doi: 10.1016/j.media.2016.10.010
98. He, Y. *et al.* Deep learning-based classification of primary bone tumors on radiographs: A preliminary study. *eBioMedicine* **62**, 103121 (2020). doi: 10.1016/j.ebiom.2020.103121
99. Von Schacky, C. E. *et al.* Multitask Deep Learning for Segmentation and Classification of Primary Bone Tumors on Radiographs. *Radiology* **301**, 398–406 (2021). doi: 10.1148/radiol.2021204531
100. Crowder, C., Heinrich, J. & Stout, S. D. Rib Histomorphometry for Adult Age Estimation. in *Forensic Microscopy for Skeletal Tissues* (ed. Bell, L. S.) vol. 915 109–127 (Humana Press, Totowa, NJ, 2012).
101. Andronowski, J. M. & Taylor, J. T. The Andronowski Skeletal Collection for Histological Research: A Modern Anatomical Contribution. *Forensic Sciences* **2**, 175–189 (2022). doi: 10.3390/forensicsci2010014

102. Andronowski, J. M., Davis, R. A. & Holyoke, C. W. A Sectioning, Coring, and Image Processing Guide for High-Throughput Cortical Bone Sample Procurement and Analysis for Synchrotron Micro-CT. *JoVE* 61081 (2020) doi: 10.3791/61081.
103. Vogelgesang, M. *et al.* Real-time image-content-based beamline control for smart 4D X-ray imaging. *J Synchrotron Rad* **23**, 1254–1263 (2016). doi: 10.1107/S1600577516010195
104. Faragó, T. *et al.* *Tofu* : a fast, versatile and user-friendly image processing toolkit for computed tomography. *J Synchrotron Rad* **29**, 916–927 (2022). doi: 10.1107/S160057752200282X
105. Hemke, R., Buckless, C. G., Tsao, A., Wang, B. & Torriani, M. Deep learning for automated segmentation of pelvic muscles, fat, and bone from CT studies for body composition assessment. *Skeletal Radiol* **49**, 387–395 (2020). doi: 10.1007/s00256-019-03289-8
106. Zhang, Z., Coyle, J. L. & Sejdić, E. Automatic hyoid bone detection in fluoroscopic images using deep learning. *Sci Rep* **8**, 12310 (2018). doi: 10.1038/s41598-018-30182-6
107. Taylor, J. T., Hassan, M. & Andronowski, J. M. Application of Deep Learning Image Segmentation to Synchrotron Radiation  $\mu$ CT Bone Microstructure Datasets. (2023).
108. Cooper, D. m. l., Turinsky, A. l., Sensen, C. w. & Hallgrímsson, B. Quantitative 3D analysis of the canal network in cortical bone by micro-computed tomography. *The Anatomical Record Part B: The New Anatomist* **274B**, 169–179 (2003). doi: 10.1002/ar.b.10024
109. Kampschulte, M. *et al.* Nano-Computed Tomography: Technique and Applications. *Fortschr Röntgenstr* **188**, 146–154 (2016). doi: 10.1055/s-0041-106541

110. Ho, C.-S. *et al.* Application of deep learning neural network in predicting bone mineral density from plain X-ray radiography. *Arch Osteoporos* **16**, 153 (2021). doi: 10.1007/s11657-021-00985-8
111. Yasaka, K., Akai, H., Kunimatsu, A., Kiryu, S. & Abe, O. Prediction of bone mineral density from computed tomography: application of deep learning with a convolutional neural network. *Eur Radiol* **30**, 3549–3557 (2020). doi: 10.1007/s00330-020-06677-0
112. Xiao, P. *et al.* Prediction of trabecular bone architectural features by deep learning models using simulated DXA images. *Bone Reports* **13**, 100295 (2020). doi: 10.1016/j.bonr.2020.100295
113. Dimililer, K. IBFDS: Intelligent bone fracture detection system. *Procedia Computer Science* **120**, 260–267 (2017). doi: 10.1016/j.procs.2017.11.237
114. Chung, S. W. *et al.* Automated detection and classification of the proximal humerus fracture by using deep learning algorithm. *Acta Orthopaedica* **89**, 468–473 (2018). doi: 10.1080/17453674.2018.1453714
115. Rajpurkar, P. *et al.* MURA: Large Dataset for Abnormality Detection in Musculoskeletal Radiographs. (2017) doi: 10.48550/ARXIV.1712.06957.
116. Lindsey, R. *et al.* Deep neural network improves fracture detection by clinicians. *Proc. Natl. Acad. Sci. U.S.A.* **115**, 11591–11596 (2018). doi: 10.1073/pnas.1806905115
117. Hassan, M., Taylor, J. T. & Andronowski, J. M. An Automated Deep Learning Approach to the Segmentation of Vascular Pore Systems and Osteocyte Lacunae in Virtual and Traditional Histologic Datasets. (2023).
118. Todd, T. W. Age changes in the pubic bone. *American J Phys Anthropol* **4**, 1–70 (1921). doi: 10.1002/ajpa.1330040102

119. Berger, C. *et al.* Change in bone mineral density as a function of age in women and men and association with the use of antiresorptive agents. *Canadian Medical Association Journal* **178**, 1660–1668 (2008). doi: 10.1503/cmaj.071416
120. Bonewald, L. Use it or lose it to age: A review of bone and muscle communication. *Bone* **120**, 212–218 (2019). doi: 10.1016/j.bone.2018.11.002
121. Chen, H., Zhou, X., Fujita, H., Onozuka, M. & Kubo, K.-Y. Age-related changes in trabecular and cortical bone microstructure. *Int J Endocrinol* **2013**, (2013). doi: 10.1155/2013/213234
122. Demontiero, O., Vidal, C. & Duque, G. Aging and bone loss: new insights for the clinician. *Ther Adv Musculoskelet Dis* **4**, 61–76 (2012). doi: 10.1177/1759720X11430858
123. Frost, H. M. On our age-related bone loss: Insights from a new paradigm. *J Bone Miner Res* **12**, 1539–1546 (1997). doi: 10.1359/jbmr.1997.12.10.1539
124. Halloran, B. P. *et al.* Changes in Bone Structure and Mass With Advancing Age in the Male C57BL/6J Mouse. *J of Bone & Mineral Res* **17**, 1044–1050 (2002). doi: 10.1359/jbmr.2002.17.6.1044
125. Szulc, P., Marchand, F., Duboeuf, F. & Delmas, P. D. Cross-sectional assessment of age-related bone loss in men: the MINOS study. *Bone* **26**, 123–129 (2000). doi: 10.1016/S8756-3282(99)00255-0
126. Jilka, R. L. & O'Brien, C. A. The Role of Osteocytes in Age-Related Bone Loss. *Curr Osteoporos Rep* **14**, 16–25 (2016). doi: 10.1007/s11914-016-0297-0
127. Khosla, S. Pathogenesis of Age-Related Bone Loss in Humans. *The Journals of Gerontology Series A: Biological Sciences and Medical Sciences* **68**, 1226–1235 (2013). doi: 10.1093/gerona/gls163

128. Jowsey, J. Age Changes in Human Bone. *Clinical Orthopaedics and Related Research* **17**, 210 (1960).
129. Russo, C. R. *et al.* Aging bone in men and women: beyond changes in bone mineral density. *Osteoporos Int* **14**, 531–538 (2003). doi: 10.1007/s00198-002-1322-y
130. Heaney, R. P. *et al.* Bone Dimensional Change with Age: Interactions of Genetic, Hormonal, and Body Size Variables: *Osteoporos Int* **7**, 426–431 (1997). doi: 10.1007/PL00004150
131. Cooper, D., Turinsky, A., Sensen, C. & Hallgrímsson, B. Effect of Voxel Size on 3D Micro-CT Analysis of Cortical Bone Porosity. *Calcif Tissue Int* **80**, 211–219 (2007). doi: 10.1007/s00223-005-0274-6
132. Cooper, D. M. L., Thomas, C. D. L., Clement, J. G. & Hallgrímsson, B. Three-dimensional microcomputed tomography imaging of basic multicellular unit-related resorption spaces in human cortical bone. *Anat. Rec.* **288A**, 806–816 (2006). doi: 10.1002/ar.a.20344
133. Nicks, K. M. *et al.* Relationship of age to bone microstructure independent of areal bone mineral density. *J of Bone & Mineral Res* **27**, 637–644 (2012). doi: 10.1002/jbmr.1468
134. Ding, Z., Ma, Z., Yang, X. & Sun, Y. Effect of Eight-Month Exercise Intervention on Bone Outcomes of Young Opioid-Dependent Women. *IJERPH* **18**, 11336 (2021). doi: 10.3390/ijerph182111336
135. Greenspan, S. L., Maitland, L. A., Myers, E. R., Krasnow, M. B. & Kido, T. H. Femoral bone loss progresses with age: A longitudinal study in women over age 65. *J of Bone & Mineral Res* **9**, 1959–1965 (1994). doi: 10.1002/jbmr.5650091216
136. Epstein, S. *et al.* The influence of age on bone mineral regulating hormones. *Bone* **7**, 421–425 (1986). doi: 10.1016/8756-3282(86)90001-3

137. Wishart, J. M., Need, A. O., Horowitz, M., Morris†, H. A. & Nordin, B. E. C. Effect of age on bone density and bone turnover in men. *Clinical Endocrinology* **42**, 141–146 (1995). doi: 10.1111/j.1365-2265.1995.tb01854.x
138. Burger, H. *et al.* The association between age and bone mineral density in men and women aged 55 years and over: The Rotterdam Study. *Bone and Mineral* **25**, 1–13 (1994). doi: 10.1016/S0169-6009(08)80203-6
139. Parfitt, A. M. Age-related structural changes in trabecular and cortical bone: cellular mechanisms and biomechanical consequences. *Calcif Tissue Int* **36 Suppl 1**, S123-128 (1984). doi: 10.1007/BF02406145
140. Kelly, J. P. *et al.* Prevalence and characteristics of opioid use in the US adult population. *Pain* **138**, 507–513 (2008). doi: 10.1016/j.pain.2008.01.027
141. Park, J.-Y. & Wu, L.-T. Sources of Misused Prescription Opioids and Their Association with Prescription Opioid Use Disorder in the United States: Sex and Age Differences. *Substance Use & Misuse* **55**, 928–936 (2020). doi: 10.1080/10826084.2020.1713818
142. Schieber, L. Z., Guy, G. P., Seth, P. & Losby, J. L. Variation in Adult Outpatient Opioid Prescription Dispensing by Age and Sex - United States, 2008-2018. *MMWR Morb Mortal Wkly Rep* **69**, 298–302 (2020). doi: 10.15585/mmwr.mm6911a5
143. Thielke, S. M. *et al.* Age and Sex Trends in Long-term Opioid Use in Two Large American Health Systems Between 2000 and 2005. *Pain Med* **11**, 248–256 (2010). doi: 10.1111/j.1526-4637.2009.00740.x
144. Chisholm-Burns, M. A., Spivey, C. A., Sherwin, E., Wheeler, J. & Hohmeier, K. The opioid crisis: Origins, trends, policies, and the roles of pharmacists. *American Journal of Health-System Pharmacy* **76**, 424–435 (2019). doi: 10.1093/ajhp/zxy089

145. Marsh, J. C., Park, K., Lin, Y.-A. & Bersamira, C. Gender differences in trends for heroin use and nonmedical prescription opioid use, 2007–2014. *Journal of Substance Abuse Treatment* **87**, 79–85 (2018). doi: 10.1016/j.jsat.2018.01.001
146. Campbell, C. I. *et al.* Age and Gender Trends in Long-Term Opioid Analgesic Use for Noncancer Pain. *Am J Public Health* **100**, 2541–2547 (2010). doi: 10.2105/AJPH.2009.180646
147. Gotthardt, F. *et al.* Bone mineral density and its determinants in men with opioid dependence. *J Bone Miner Metab* **35**, 99–107 (2017). doi: 10.1007/s00774-015-0732-9
148. Fortin, J. D., Bailey, G. M. & Vilensky, J. A. Does opioid use for pain management warrant routine bone mass density screening in men? *Pain Physician* **11**, 539–541 (2008).
149. Duarte, R. V. *et al.* Hypogonadism and low bone mineral density in patients on long-term intrathecal opioid delivery therapy. *BMJ Open* **3**, e002856 (2013). doi: 10.1136/bmjopen-2013-002856
150. Finch, P. M., Price, L. M., Pullan, P. T. & Drummond, P. D. Effects of Testosterone Treatment on Bone Mineral Density in Hypogonadal Men Receiving Intrathecal Opioids. *Pain Practice* **15**, 308–313 (2015). doi: 10.1111/papr.12190
151. Kim, T. W., Alford, D. P., Malabanan, A., Holick, M. F. & Samet, J. H. Low bone density in patients receiving methadone maintenance treatment. *Drug and Alcohol Dependence* **85**, 258–262 (2006). doi: 10.1016/j.drugalcdep.2006.05.027
152. Grey, A. *et al.* Decreased bone density in men on methadone maintenance therapy. *Addiction* **106**, 349–354 (2011). doi: 10.1111/j.1360-0443.2010.03159.x



153. Al-Bashaireh, A. M. *et al.* The Effect of Tobacco Smoking on Bone Mass: An Overview of Pathophysiologic Mechanisms. *Journal of Osteoporosis* vol. 2018 e1206235  
<https://www.hindawi.com/journals/jos/2018/1206235/> (2018). doi: 10.1155/2018/1206235
154. Seeman, E. Chapter 31 - Effects of Tobacco and Alcohol Use on Bone. in *Osteoporosis (Second Edition)* (eds. Marcus, R., Feldman, D. & Kelsey, J.) 771–794 (Academic Press, San Diego, 2001). doi:10.1016/B978-012470862-4/50032-5.
155. Maurel, D. B., Boisseau, N., Benhamou, C. L. & Jaffre, C. Alcohol and bone: review of dose effects and mechanisms. *Osteoporos Int* **23**, 1–16 (2012). doi: 10.1007/s00198-011-1787-7
156. Mikosch, P. Alcohol and bone. *Wien Med Wochenschr* **164**, 15–24 (2014). doi: 10.1007/s10354-013-0258-5
157. Sampson, H. W. Alcohol and other factors affecting osteoporosis risk in women. *Alcohol Res Health* **26**, 292–298 (2002).
158. Turner, R. T. *Alcohol and Adaptation to Mechanical Usage*.  
<https://apps.dtic.mil/sti/citations/ADA398383> (2001).
159. Wu, L. *et al.* Effects of dezocine on morphine tolerance and opioid receptor expression in a rat model of bone cancer pain. *BMC Cancer* **21**, 1128 (2021). doi: 10.1186/s12885-021-08850-0
160. Vellucci, R., Mediati, R. D. & Ballerini, G. Use of opioids for treatment of osteoporotic pain. *Clin Cases Miner Bone Metab* **11**, 173–176 (2014).
161. Wezeman, F. H. & Gong, Z. Adipogenic Effect of Alcohol on Human Bone Marrow-Derived Mesenchymal Stem Cells: *Alcoholism: Clinical & Experimental Research* **28**, 1091–1101 (2004). doi: 10.1097/01.ALC.0000130808.49262.F5

162. Ko, C. H. *et al.* Deteriorating Effect on Bone Metabolism and Microstructure by Passive Cigarette Smoking Through Dual Actions on Osteoblast and Osteoclast. *Calcif Tissue Int* **96**, 389–400 (2015). doi: 10.1007/s00223-015-9966-8
163. Duca, Y., Aversa, A., Condorelli, R. A., Calogero, A. E. & La Vignera, S. Substance Abuse and Male Hypogonadism. *Journal of Clinical Medicine* **8**, 732 (2019). doi: 10.3390/jcm8050732
164. Heath, I. & Montori, V. M. Responding to the crisis of care. *BMJ* p464 (2023) doi: 10.1136/bmj.p464.
165. Rogers, L. C., Lavery, L. A., Joseph, W. S. & Armstrong, D. G. All Feet on Deck: The Role of Podiatry During the COVID-19 Pandemic: Preventing Hospitalizations in an Overburdened Health-Care System, Reducing Amputation and Death in People with Diabetes. *Journal of the American Podiatric Medical Association* **113**, 20–051 (2023). doi: 10.7547/20-051
166. Ali, H., Cole, A., Ahmed, A., Hamasha, S. & Panos, G. Major Stressors and Coping Strategies of Frontline Nursing Staff During the Outbreak of Coronavirus Disease 2020 (COVID-19) in Alabama. *JMDH Volume* **13**, 2057–2068 (2020). doi: 10.2147/JMDH.S285933
167. Room, R. Stigma, social inequality and alcohol and drug use. *Drug and Alcohol Review* **24**, 143–155 (2005). doi: 10.1080/09595230500102434
168. Olsen, J. A., Richardson, J., Dolan, P. & Menzel, P. The moral relevance of personal characteristics in setting health care priorities. *Social Science & Medicine* **57**, 1163–1172 (2003). doi: 10.1016/S0277-9536(02)00492-6

169. Muncan, B., Walters, S. M., Ezell, J. & Ompad, D. C. “They look at us like junkies”: influences of drug use stigma on the healthcare engagement of people who inject drugs in New York City. *Harm Reduct J* **17**, 53 (2020). doi: 10.1186/s12954-020-00399-8
170. Stengel, C. The risk of being ‘too honest’: drug use, stigma and pregnancy. *Health, Risk & Society* **16**, 36–50 (2014). doi: 10.1080/13698575.2013.868408
171. Strong, P. M. Doctors and dirty work--the case of alcoholism. *Sociol Health & Illness* **2**, 24–47 (1980). doi: 10.1111/1467-9566.ep11340296
172. Sudnow, D. Dead on arrival. *Society* **5**, 36–43 (1967). doi: 10.1007/BF03180093
173. Ahern, J., Stuber, J. & Galea, S. Stigma, discrimination and the health of illicit drug users. *Drug and Alcohol Dependence* **88**, 188–196 (2007). doi: 10.1016/j.drugalcdep.2006.10.014
174. Kurtz, S. P., Surratt, H. L., Kiley, M. C. & Inciardi, J. A. Barriers to Health and Social Services for Street-Based Sex Workers. *Journal of Health Care for the Poor and Underserved* **16**, 345–361 (2005). doi: 10.1353/hpu.2005.0038

## 7. Appendices

## Appendix 7.1: Ethics Approval Renewal

# HREB - Approval of Ethics Renewal 558966

administrator@hrea.ca

Tue 1/11/2022 10:49 AM

To: Andronowski, Janna <jandronowski@mun.ca>;

Cc: administrator@hrea.ca <administrator@hrea.ca>;

Researcher Portal File #: 20211245

Dear Dr. Janna Andronowski:

This e-mail serves as notification that your ethics renewal for study HREB # 2020.308 – Are Sex Differences in Bone's Cellular Network Linked to Osteoporosis? – has been **approved**. Please log in to the Researcher Portal to view the approved event.

Ethics approval for this project has been granted for a period of twelve months effective from **January 6, 2022** to January 6, 2023.

Please note, it is the responsibility of the Principal Investigator (PI) to ensure that the Ethics Renewal form is submitted prior to the renewal date each year. Though the Research Ethics Office makes every effort to remind the PI of this responsibility, the PI may not receive a reminder. The Ethics Renewal form can be found on the Researcher Portal as an “Event”.

The ethics renewal **[will be reported]** to the Health Research Ethics Board at their meeting dated **January 13, 2022**.

Thank you,

Research Ethics Office

(e) [info@hrea.ca](mailto:info@hrea.ca)

(t) 709-777-6974

(f) 709-777-8776

(w) [www.hrea.ca](http://www.hrea.ca)

Office Hours: 8:30 a.m. – 4:30 p.m. (NL TIME) Monday-Friday

This email is intended as a private communication for the sole use of the primary addressee and those individuals copied in the original message. If you are not an intended recipient of this message you are hereby notified that copying, forwarding or other dissemination or distribution of this communication by any means is prohibited. If you believe that you have received this message in error please notify the original sender immediately.

## HREB - Approval of Ethics Renewal 20211245

administrator@hrea.ca

Thu 1/12/2023 9:39 PM

To: Andronowski, Janna <jandronowski@mun.ca>;

Cc: administrator@hrea.ca <administrator@hrea.ca>;

Researcher Portal File #: 20211245

Dear Dr. Janna Andronowski:

This e-mail serves as notification that your ethics renewal for study HREB # 2020.308 – Are Sex Differences in Bone's Cellular Network Linked to Osteoporosis? – has been **approved**. Please log in to the Researcher Portal to view the approved event.

Ethics approval for this project has been granted for a period of twelve months effective from **January 6, 2023 to January 6, 2024**.

Please note, it is the responsibility of the Principal Investigator (PI) to ensure that the Ethics Renewal form is submitted prior to the renewal date each year. Though the Research Ethics Office makes every effort to remind the PI of this responsibility, the PI may not receive a reminder. The Ethics Renewal form can be found on the Researcher Portal as an “Event”.

The ethics renewal **will be reported** to the Health Research Ethics Board at their meeting dated **January 26, 2023**.

Thank you,

Research Ethics Office

(e) [info@hrea.ca](mailto:info@hrea.ca)

(t) 709-777-6974

(f) 709-777-8776

(w) [www.hrea.ca](http://www.hrea.ca)

Office Hours: 8:30 a.m. – 4:30 p.m. (NL TIME) Monday-Friday

This email is intended as a private communication for the sole use of the primary addressee and those individuals copied in the original message. If you are not an intended recipient of this message you are hereby notified that copying, forwarding or other dissemination or distribution of this communication by any means is prohibited. If you believe that you have received this message in error please notify the original sender immediately.

## **Appendix 7.2: Deep Learning Training Tests**

Definitions for the parameters tested:

Best Val Loss - The best reported loss from the loss function during the data training.

Depth Level – Depth of the convolutional neural network.

Initial Filter Count – number of filters applied at the first convolutional layer

Brightness – Darkens the image by a specified amount during the training process.

Gaussian Noise – Adds noise to the data for training.

Elastic Transformation – Stretches the training data to a specific range.

Patch Size – Separates the training data to a specified size of pixels to decrease training time and computer memory usage.

Stride Ratio – Ratio of the overlap between adjacent patches.

Batch Size – Patches are randomly categorized and sorted into batches. Batch size determines the number of patches per batch.

Loss Function – The detected error between the predicted segmentation and the outcome.

Optimization Algorithm – A calculation that uses the loss function to update training parameters to reduce future predictive errors.



**Table 1.** U-Net++ Parameter Testing.

Test Type	Best Val Loss	Depth level	Initial filter count	Brightness	Gaussian Noise	Elastic Transformation	Patch size	Stride ratio	Batch size	Loss function	Optimization algorithm
Depth Level	0.07686	4	32	N	N	N	64	1	32	ORSDiceLoss	Adadelta
	0.02741	2	32	N	N	N	64	1	32	ORSDiceLoss	Adadelta
	0.02097	3	32	N	N	N	64	1	32	ORSDiceLoss	Adadelta
	0.02342	4	32	N	N	N	64	1	32	ORSDiceLoss	Adadelta
	0.02208	5	32	N	N	N	64	1	32	ORSDiceLoss	Adadelta
	0.025	6	32	N	N	N	64	1	32	ORSDiceLoss	Adadelta
	0.07607	7	32	N	N	N	64	1	32	ORSDiceLoss	Adadelta
Initial Filter Count	0.02516	4	8	N	N	N	64	1	32	ORSDiceLoss	Adadelta
	0.01991	4	16	N	N	N	64	1	32	ORSDiceLoss	Adadelta
	0.08243	4	32	N	N	N	64	1	32	ORSDiceLoss	Adadelta
	0.02188	4	64	N	N	N	64	1	32	ORSDiceLoss	Adadelta
	0.10173	4	128	N	N	N	64	1	32	ORSDiceLoss	Adadelta
	0.01528	4	256	N	N	N	64	1	32	ORSDiceLoss	Adadelta
Horizontal Flip	0.03317	4	32	N	N	N	64	1	32	ORSDiceLoss	Adadelta
	0.02378	4	32	N	N	N	64	1	32	ORSDiceLoss	Adadelta
Vertical Flip	0.02348	4	32	N	N	N	64	1	32	ORSDiceLoss	Adadelta
	0.074	4	32	N	N	N	64	1	32	ORSDiceLoss	Adadelta
Rotate	0.01954	4	32	N	N	N	64	1	32	ORSDiceLoss	Adadelta
	0.0277	4	32	N	N	N	64	1	32	ORSDiceLoss	Adadelta
	0.02852	4	32	N	N	N	64	1	32	ORSDiceLoss	Adadelta
	0.0785	4	32	N	N	N	64	1	32	ORSDiceLoss	Adadelta
	0.02238	4	32	N	N	N	64	1	32	ORSDiceLoss	Adadelta

	0.07817	4	32	N	N	N	64	1	32	ORSDiceLoss	Adadelta
	0.02321	4	32	N	N	N	64	1	32	ORSDiceLoss	Adadelta
	0.02401	4	32	N	N	N	64	1	32	ORSDiceLoss	Adadelta
	0.08669	4	32	N	N	N	64	1	32	ORSDiceLoss	Adadelta
	0.03018	4	32	N	N	N	64	1	32	ORSDiceLoss	Adadelta
	0.08334	4	32	N	N	N	64	1	32	ORSDiceLoss	Adadelta
	0.02483	4	32	N	N	N	64	1	32	ORSDiceLoss	Adadelta
	0.02706	4	32	N	N	N	64	1	32	ORSDiceLoss	Adadelta
Shear	0.08318	4	32	N	N	N	64	1	32	ORSDiceLoss	Adadelta
	0.02893	4	32	N	N	N	64	1	32	ORSDiceLoss	Adadelta
	0.02371	4	32	N	N	N	64	1	32	ORSDiceLoss	Adadelta
	0.02194	4	32	N	N	N	64	1	32	ORSDiceLoss	Adadelta
	0.02211	4	32	N	N	N	64	1	32	ORSDiceLoss	Adadelta
	0.02176	4	32	N	N	N	64	1	32	ORSDiceLoss	Adadelta
	0.03398	4	32	N	N	N	64	1	32	ORSDiceLoss	Adadelta
	0.02358	4	32	N	N	N	64	1	32	ORSDiceLoss	Adadelta
	0.07794	4	32	N	N	N	64	1	32	ORSDiceLoss	Adadelta
	0.02581	4	32	N	N	N	64	1	32	ORSDiceLoss	Adadelta
0.02243	4	32	N	N	N	64	1	32	ORSDiceLoss	Adadelta	
Scale	0.06872	4	32	N	N	N	64	1	32	ORSDiceLoss	Adadelta
	0.08308	4	32	N	N	N	64	1	32	ORSDiceLoss	Adadelta
	0.0215	4	32	N	N	N	64	1	32	ORSDiceLoss	Adadelta
	0.08123	4	32	N	N	N	64	1	32	ORSDiceLoss	Adadelta
	0.01752	4	32	N	N	N	64	1	32	ORSDiceLoss	Adadelta
	0.07212	4	32	N	N	N	64	1	32	ORSDiceLoss	Adadelta
	0.02298	4	32	N	N	N	64	1	32	ORSDiceLoss	Adadelta
	0.02145	4	32	N	N	N	64	1	32	ORSDiceLoss	Adadelta
	0.01736	4	32	N	N	N	64	1	32	ORSDiceLoss	Adadelta
0.07193	4	32	N	N	N	64	1	32	ORSDiceLoss	Adadelta	
Brightn ess	0.02679	4	32	N	N	N	64	1	32	ORSDiceLoss	Adadelta
	0.03641	4	32	0.1-2	N	N	64	1	32	ORSDiceLoss	Adadelta
	0.02099	4	32	0.2-1.9	N	N	64	1	32	ORSDiceLoss	Adadelta

	<b>0.03115</b>	<b>4</b>	<b>32</b>	<b>0.3-1.8</b>	<b>N</b>	<b>N</b>	<b>64</b>	<b>1</b>	<b>32</b>	<b>ORSDiceLoss</b>	<b>Adadelta</b>
	<b>0.02418</b>	<b>4</b>	<b>32</b>	<b>0.4-1.7</b>	<b>N</b>	<b>N</b>	<b>64</b>	<b>1</b>	<b>32</b>	<b>ORSDiceLoss</b>	<b>Adadelta</b>
	<b>0.0263</b>	<b>4</b>	<b>32</b>	<b>0.5-1.6</b>	<b>N</b>	<b>N</b>	<b>64</b>	<b>1</b>	<b>32</b>	<b>ORSDiceLoss</b>	<b>Adadelta</b>
	<b>0.07404</b>	<b>4</b>	<b>32</b>	<b>0.6-1.5</b>	<b>N</b>	<b>N</b>	<b>64</b>	<b>1</b>	<b>32</b>	<b>ORSDiceLoss</b>	<b>Adadelta</b>
	<b>0.03172</b>	<b>4</b>	<b>32</b>	<b>0.7-1.4</b>	<b>N</b>	<b>N</b>	<b>64</b>	<b>1</b>	<b>32</b>	<b>ORSDiceLoss</b>	<b>Adadelta</b>
	<b>0.01992</b>	<b>4</b>	<b>32</b>	<b>0.8-1.3</b>	<b>N</b>	<b>N</b>	<b>64</b>	<b>1</b>	<b>32</b>	<b>ORSDiceLoss</b>	<b>Adadelta</b>
	<b>0.07878</b>	<b>4</b>	<b>32</b>	<b>0.9-1.2</b>	<b>N</b>	<b>N</b>	<b>64</b>	<b>1</b>	<b>32</b>	<b>ORSDiceLoss</b>	<b>Adadelta</b>
	<b>0.07724</b>	<b>4</b>	<b>32</b>	<b>0.9-1.1</b>	<b>N</b>	<b>N</b>	<b>64</b>	<b>1</b>	<b>32</b>	<b>ORSDiceLoss</b>	<b>Adadelta</b>
<b>Noise</b>	<b>0.0881</b>	<b>4</b>	<b>32</b>	<b>N</b>	<b>N</b>	<b>N</b>	<b>64</b>	<b>1</b>	<b>32</b>	<b>ORSDiceLoss</b>	<b>Adadelta</b>
	<b>0.03059</b>	<b>4</b>	<b>32</b>	<b>N</b>	<b>0-0.1</b>	<b>N</b>	<b>64</b>	<b>1</b>	<b>32</b>	<b>ORSDiceLoss</b>	<b>Adadelta</b>
	<b>0.03267</b>	<b>4</b>	<b>32</b>	<b>N</b>	<b>0-0.09</b>	<b>N</b>	<b>64</b>	<b>1</b>	<b>32</b>	<b>ORSDiceLoss</b>	<b>Adadelta</b>
	<b>0.04419</b>	<b>4</b>	<b>32</b>	<b>N</b>	<b>0-0.08</b>	<b>N</b>	<b>64</b>	<b>1</b>	<b>32</b>	<b>ORSDiceLoss</b>	<b>Adadelta</b>
	<b>0.08511</b>	<b>4</b>	<b>32</b>	<b>N</b>	<b>0-0.07</b>	<b>N</b>	<b>64</b>	<b>1</b>	<b>32</b>	<b>ORSDiceLoss</b>	<b>Adadelta</b>
	<b>0.08254</b>	<b>4</b>	<b>32</b>	<b>N</b>	<b>0-0.06</b>	<b>N</b>	<b>64</b>	<b>1</b>	<b>32</b>	<b>ORSDiceLoss</b>	<b>Adadelta</b>
	<b>0.03495</b>	<b>4</b>	<b>32</b>	<b>N</b>	<b>0-0.05</b>	<b>N</b>	<b>64</b>	<b>1</b>	<b>32</b>	<b>ORSDiceLoss</b>	<b>Adadelta</b>
	<b>0.08257</b>	<b>4</b>	<b>32</b>	<b>N</b>	<b>0-0.04</b>	<b>N</b>	<b>64</b>	<b>1</b>	<b>32</b>	<b>ORSDiceLoss</b>	<b>Adadelta</b>
	<b>0.03378</b>	<b>4</b>	<b>32</b>	<b>N</b>	<b>0-0.03</b>	<b>N</b>	<b>64</b>	<b>1</b>	<b>32</b>	<b>ORSDiceLoss</b>	<b>Adadelta</b>
	<b>0.05272</b>	<b>4</b>	<b>32</b>	<b>N</b>	<b>0-0.02</b>	<b>N</b>	<b>64</b>	<b>1</b>	<b>32</b>	<b>ORSDiceLoss</b>	<b>Adadelta</b>
	<b>0.08341</b>	<b>4</b>	<b>32</b>	<b>N</b>	<b>0-0.01</b>	<b>N</b>	<b>64</b>	<b>1</b>	<b>32</b>	<b>ORSDiceLoss</b>	<b>Adadelta</b>
<b>0.08059</b>	<b>4</b>	<b>32</b>	<b>N</b>	<b>0-0.001</b>	<b>N</b>	<b>64</b>	<b>1</b>	<b>32</b>	<b>ORSDiceLoss</b>	<b>Adadelta</b>	
<b>Elastic Transformation</b>	<b>0.08389</b>	<b>4</b>	<b>32</b>	<b>N</b>	<b>N</b>	<b>N</b>	<b>64</b>	<b>1</b>	<b>32</b>	<b>ORSDiceLoss</b>	<b>Adadelta</b>
	<b>0.02734</b>	<b>4</b>	<b>32</b>	<b>N</b>	<b>N</b>	<b>0.01-1</b>	<b>64</b>	<b>1</b>	<b>32</b>	<b>ORSDiceLoss</b>	<b>Adadelta</b>
	<b>0.07815</b>	<b>4</b>	<b>32</b>	<b>N</b>	<b>N</b>	<b>0.05-0.95</b>	<b>64</b>	<b>1</b>	<b>32</b>	<b>ORSDiceLoss</b>	<b>Adadelta</b>
	<b>0.03482</b>	<b>4</b>	<b>32</b>	<b>N</b>	<b>N</b>	<b>0.1-0.9</b>	<b>64</b>	<b>1</b>	<b>32</b>	<b>ORSDiceLoss</b>	<b>Adadelta</b>
	<b>0.02531</b>	<b>4</b>	<b>32</b>	<b>N</b>	<b>N</b>	<b>0.15-0.85</b>	<b>64</b>	<b>1</b>	<b>32</b>	<b>ORSDiceLoss</b>	<b>Adadelta</b>
	<b>0.0264</b>	<b>4</b>	<b>32</b>	<b>N</b>	<b>N</b>	<b>0.2-0.8</b>	<b>64</b>	<b>1</b>	<b>32</b>	<b>ORSDiceLoss</b>	<b>Adadelta</b>
	<b>0.08462</b>	<b>4</b>	<b>32</b>	<b>N</b>	<b>N</b>	<b>0.25-0.75</b>	<b>64</b>	<b>1</b>	<b>32</b>	<b>ORSDiceLoss</b>	<b>Adadelta</b>
	<b>0.02554</b>	<b>4</b>	<b>32</b>	<b>N</b>	<b>N</b>	<b>0.3-0.7</b>	<b>64</b>	<b>1</b>	<b>32</b>	<b>ORSDiceLoss</b>	<b>Adadelta</b>
	<b>0.02654</b>	<b>4</b>	<b>32</b>	<b>N</b>	<b>N</b>	<b>0.35-0.65</b>	<b>64</b>	<b>1</b>	<b>32</b>	<b>ORSDiceLoss</b>	<b>Adadelta</b>
	<b>0.02512</b>	<b>4</b>	<b>32</b>	<b>N</b>	<b>N</b>	<b>0.4-0.6</b>	<b>64</b>	<b>1</b>	<b>32</b>	<b>ORSDiceLoss</b>	<b>Adadelta</b>
<b>0.02097</b>	<b>4</b>	<b>32</b>	<b>N</b>	<b>N</b>	<b>0.45-0.55</b>	<b>64</b>	<b>1</b>	<b>32</b>	<b>ORSDiceLoss</b>	<b>Adadelta</b>	
<b>0.08279</b>	<b>4</b>	<b>32</b>	<b>N</b>	<b>N</b>	<b>0.5-0.5</b>	<b>64</b>	<b>1</b>	<b>32</b>	<b>ORSDiceLoss</b>	<b>Adadelta</b>	

	<b>0.02096</b>	<b>4</b>	<b>32</b>	<b>N</b>	<b>N</b>	<b>0.08-0.16</b>	<b>64</b>	<b>1</b>	<b>32</b>	<b>ORSDiceLoss</b>	<b>Adadelta</b>
<b>Stride Ratio</b>	<b>0.01552</b>	<b>4</b>	<b>32</b>	<b>N</b>	<b>N</b>	<b>N</b>	<b>64</b>	<b>0.05</b>	<b>32</b>	<b>ORSDiceLoss</b>	<b>Adadelta</b>
	<b>0.01697</b>	<b>4</b>	<b>32</b>	<b>N</b>	<b>N</b>	<b>N</b>	<b>64</b>	<b>0.15</b>	<b>32</b>	<b>ORSDiceLoss</b>	<b>Adadelta</b>
	<b>0.01482</b>	<b>4</b>	<b>32</b>	<b>N</b>	<b>N</b>	<b>N</b>	<b>64</b>	<b>0.25</b>	<b>32</b>	<b>ORSDiceLoss</b>	<b>Adadelta</b>
	<b>0.02064</b>	<b>4</b>	<b>32</b>	<b>N</b>	<b>N</b>	<b>N</b>	<b>64</b>	<b>0.35</b>	<b>32</b>	<b>ORSDiceLoss</b>	<b>Adadelta</b>
	<b>0.02827</b>	<b>4</b>	<b>32</b>	<b>N</b>	<b>N</b>	<b>N</b>	<b>64</b>	<b>0.45</b>	<b>32</b>	<b>ORSDiceLoss</b>	<b>Adadelta</b>
	<b>0.03631</b>	<b>4</b>	<b>32</b>	<b>N</b>	<b>N</b>	<b>N</b>	<b>64</b>	<b>0.55</b>	<b>32</b>	<b>ORSDiceLoss</b>	<b>Adadelta</b>
	<b>0.08015</b>	<b>4</b>	<b>32</b>	<b>N</b>	<b>N</b>	<b>N</b>	<b>64</b>	<b>0.65</b>	<b>32</b>	<b>ORSDiceLoss</b>	<b>Adadelta</b>
	<b>0.09291</b>	<b>4</b>	<b>32</b>	<b>N</b>	<b>N</b>	<b>N</b>	<b>64</b>	<b>0.75</b>	<b>32</b>	<b>ORSDiceLoss</b>	<b>Adadelta</b>
	<b>0.0754</b>	<b>4</b>	<b>32</b>	<b>N</b>	<b>N</b>	<b>N</b>	<b>64</b>	<b>0.85</b>	<b>32</b>	<b>ORSDiceLoss</b>	<b>Adadelta</b>
	<b>0.0357</b>	<b>4</b>	<b>32</b>	<b>N</b>	<b>N</b>	<b>N</b>	<b>64</b>	<b>0.95</b>	<b>32</b>	<b>ORSDiceLoss</b>	<b>Adadelta</b>
	<b>0.02512</b>	<b>4</b>	<b>32</b>	<b>N</b>	<b>N</b>	<b>N</b>	<b>64</b>	<b>1</b>	<b>32</b>	<b>ORSDiceLoss</b>	<b>Adadelta</b>
	<b>0.09936</b>	<b>4</b>	<b>32</b>	<b>N</b>	<b>N</b>	<b>N</b>	<b>64</b>	<b>1.1</b>	<b>32</b>	<b>ORSDiceLoss</b>	<b>Adadelta</b>
	<b>0.66014</b>	<b>4</b>	<b>32</b>	<b>N</b>	<b>N</b>	<b>N</b>	<b>64</b>	<b>1.2</b>	<b>32</b>	<b>ORSDiceLoss</b>	<b>Adadelta</b>
	<b>0.03369</b>	<b>4</b>	<b>32</b>	<b>N</b>	<b>N</b>	<b>N</b>	<b>64</b>	<b>1.3</b>	<b>32</b>	<b>ORSDiceLoss</b>	<b>Adadelta</b>
	<b>0.15741</b>	<b>4</b>	<b>32</b>	<b>N</b>	<b>N</b>	<b>N</b>	<b>64</b>	<b>1.4</b>	<b>32</b>	<b>ORSDiceLoss</b>	<b>Adadelta</b>
	<b>0.66541</b>	<b>4</b>	<b>32</b>	<b>N</b>	<b>N</b>	<b>N</b>	<b>64</b>	<b>1.5</b>	<b>32</b>	<b>ORSDiceLoss</b>	<b>Adadelta</b>
<b>0.65964</b>	<b>4</b>	<b>32</b>	<b>N</b>	<b>N</b>	<b>N</b>	<b>64</b>	<b>1.6</b>	<b>32</b>	<b>ORSDiceLoss</b>	<b>Adadelta</b>	
<b>Patch Size</b>	<b>0.02447</b>	<b>4</b>	<b>32</b>	<b>N</b>	<b>N</b>	<b>N</b>	<b>32</b>	<b>1</b>	<b>32</b>	<b>ORSDiceLoss</b>	<b>Adadelta</b>
	<b>0.05351</b>	<b>4</b>	<b>32</b>	<b>N</b>	<b>N</b>	<b>N</b>	<b>40</b>	<b>1</b>	<b>32</b>	<b>ORSDiceLoss</b>	<b>Adadelta</b>
	<b>0.0548</b>	<b>4</b>	<b>32</b>	<b>N</b>	<b>N</b>	<b>N</b>	<b>48</b>	<b>1</b>	<b>32</b>	<b>ORSDiceLoss</b>	<b>Adadelta</b>
	<b>0.02396</b>	<b>4</b>	<b>32</b>	<b>N</b>	<b>N</b>	<b>N</b>	<b>56</b>	<b>1</b>	<b>32</b>	<b>ORSDiceLoss</b>	<b>Adadelta</b>
	<b>0.02415</b>	<b>4</b>	<b>32</b>	<b>N</b>	<b>N</b>	<b>N</b>	<b>64</b>	<b>1</b>	<b>32</b>	<b>ORSDiceLoss</b>	<b>Adadelta</b>
	<b>0.0352</b>	<b>4</b>	<b>32</b>	<b>N</b>	<b>N</b>	<b>N</b>	<b>72</b>	<b>1</b>	<b>32</b>	<b>ORSDiceLoss</b>	<b>Adadelta</b>
	<b>0.02127</b>	<b>4</b>	<b>32</b>	<b>N</b>	<b>N</b>	<b>N</b>	<b>80</b>	<b>1</b>	<b>32</b>	<b>ORSDiceLoss</b>	<b>Adadelta</b>
	<b>0.04146</b>	<b>4</b>	<b>32</b>	<b>N</b>	<b>N</b>	<b>N</b>	<b>88</b>	<b>1</b>	<b>32</b>	<b>ORSDiceLoss</b>	<b>Adadelta</b>
	<b>0.03454</b>	<b>4</b>	<b>32</b>	<b>N</b>	<b>N</b>	<b>N</b>	<b>96</b>	<b>1</b>	<b>32</b>	<b>ORSDiceLoss</b>	<b>Adadelta</b>
	<b>0.65269</b>	<b>4</b>	<b>32</b>	<b>N</b>	<b>N</b>	<b>N</b>	<b>104</b>	<b>1</b>	<b>32</b>	<b>ORSDiceLoss</b>	<b>Adadelta</b>
	<b>0.04483</b>	<b>4</b>	<b>32</b>	<b>N</b>	<b>N</b>	<b>N</b>	<b>112</b>	<b>1</b>	<b>32</b>	<b>ORSDiceLoss</b>	<b>Adadelta</b>
<b>0.62585</b>	<b>4</b>	<b>32</b>	<b>N</b>	<b>N</b>	<b>N</b>	<b>120</b>	<b>1</b>	<b>32</b>	<b>ORSDiceLoss</b>	<b>Adadelta</b>	
<b>Batch Size</b>	<b>0.04399</b>	<b>4</b>	<b>32</b>	<b>N</b>	<b>N</b>	<b>N</b>	<b>64</b>	<b>1</b>	<b>1</b>	<b>ORSDiceLoss</b>	<b>Adadelta</b>
	<b>0.04066</b>	<b>4</b>	<b>32</b>	<b>N</b>	<b>N</b>	<b>N</b>	<b>64</b>	<b>1</b>	<b>2</b>	<b>ORSDiceLoss</b>	<b>Adadelta</b>

	<b>0.03134</b>	<b>4</b>	<b>32</b>	<b>N</b>	<b>N</b>	<b>N</b>	<b>64</b>	<b>1</b>	<b>4</b>	<b>ORSDiceLoss</b>	<b>Adadelta</b>
	<b>0.02769</b>	<b>4</b>	<b>32</b>	<b>N</b>	<b>N</b>	<b>N</b>	<b>64</b>	<b>1</b>	<b>8</b>	<b>ORSDiceLoss</b>	<b>Adadelta</b>
	<b>0.02508</b>	<b>4</b>	<b>32</b>	<b>N</b>	<b>N</b>	<b>N</b>	<b>64</b>	<b>1</b>	<b>16</b>	<b>ORSDiceLoss</b>	<b>Adadelta</b>
	<b>0.07723</b>	<b>4</b>	<b>32</b>	<b>N</b>	<b>N</b>	<b>N</b>	<b>64</b>	<b>1</b>	<b>32</b>	<b>ORSDiceLoss</b>	<b>Adadelta</b>
	<b>0.02449</b>	<b>4</b>	<b>32</b>	<b>N</b>	<b>N</b>	<b>N</b>	<b>64</b>	<b>1</b>	<b>64</b>	<b>ORSDiceLoss</b>	<b>Adadelta</b>
	<b>0.04177</b>	<b>4</b>	<b>32</b>	<b>N</b>	<b>N</b>	<b>N</b>	<b>64</b>	<b>1</b>	<b>128</b>	<b>ORSDiceLoss</b>	<b>Adadelta</b>
<b>Loss Function</b>	<b>0.01177</b>	<b>4</b>	<b>32</b>	<b>N</b>	<b>N</b>	<b>N</b>	<b>64</b>	<b>1</b>	<b>32</b>	<b>Categorical Crossentropy</b>	<b>Adadelta</b>
	<b>0.10984</b>	<b>4</b>	<b>32</b>	<b>N</b>	<b>N</b>	<b>N</b>	<b>64</b>	<b>1</b>	<b>32</b>	<b>Categorical Hinge</b>	<b>Adadelta</b>
	<b>-0.95017</b>	<b>4</b>	<b>32</b>	<b>N</b>	<b>N</b>	<b>N</b>	<b>64</b>	<b>1</b>	<b>32</b>	<b>Cosine Similarity</b>	<b>Adadelta</b>
	<b>0.01098</b>	<b>4</b>	<b>32</b>	<b>N</b>	<b>N</b>	<b>N</b>	<b>64</b>	<b>1</b>	<b>32</b>	<b>KLDivergence</b>	<b>Adadelta</b>
	<b>0.02335</b>	<b>4</b>	<b>32</b>	<b>N</b>	<b>N</b>	<b>N</b>	<b>64</b>	<b>1</b>	<b>32</b>	<b>ORSDiceLoss</b>	<b>Adadelta</b>
	<b>0.04656</b>	<b>4</b>	<b>32</b>	<b>N</b>	<b>N</b>	<b>N</b>	<b>64</b>	<b>1</b>	<b>32</b>	<b>OrsJaccardDist ance</b>	<b>Adadelta</b>
<b>Optimiz ation Algorit hm</b>	<b>0.02358</b>	<b>4</b>	<b>32</b>	<b>N</b>	<b>N</b>	<b>N</b>	<b>64</b>	<b>1</b>	<b>32</b>	<b>ORSDiceLoss</b>	<b>Adadelta</b>
	<b>0.67523</b>	<b>4</b>	<b>32</b>	<b>N</b>	<b>N</b>	<b>N</b>	<b>64</b>	<b>1</b>	<b>32</b>	<b>ORSDiceLoss</b>	<b>Adagrad</b>
	<b>Error</b>	<b>4</b>	<b>32</b>	<b>N</b>	<b>N</b>	<b>N</b>	<b>64</b>	<b>1</b>	<b>32</b>	<b>ORSDiceLoss</b>	<b>Adam</b>
	<b>Error</b>	<b>4</b>	<b>32</b>	<b>N</b>	<b>N</b>	<b>N</b>	<b>64</b>	<b>1</b>	<b>32</b>	<b>ORSDiceLoss</b>	<b>Adamax</b>
	<b>0.66221</b>	<b>4</b>	<b>32</b>	<b>N</b>	<b>N</b>	<b>N</b>	<b>64</b>	<b>1</b>	<b>32</b>	<b>ORSDiceLoss</b>	<b>Ftrl</b>
	<b>Error</b>	<b>4</b>	<b>32</b>	<b>N</b>	<b>N</b>	<b>N</b>	<b>64</b>	<b>1</b>	<b>32</b>	<b>ORSDiceLoss</b>	<b>Nadam</b>
	<b>Error</b>	<b>4</b>	<b>32</b>	<b>N</b>	<b>N</b>	<b>N</b>	<b>64</b>	<b>1</b>	<b>32</b>	<b>ORSDiceLoss</b>	<b>RMSProp</b>
	<b>0.66406</b>	<b>4</b>	<b>32</b>	<b>N</b>	<b>N</b>	<b>N</b>	<b>64</b>	<b>1</b>	<b>32</b>	<b>ORSDiceLoss</b>	<b>SGD</b>

Table 2. U-Net 3D Parameter Testing

Test Type	Best Val Loss	Initial filter count	Brightness	Gaussian Noise	Elastic Transformation	Slices	Patch size	Stride ratio	Batch size	Loss function	Optimization algorithm
Depth Level and Patch Size	0.03128	32	N	N	N	32	32	1	32	ORSDiceLoss	Adadelta
	0.01968	32	N	N	N	32	32	1	32	ORSDiceLoss	Adadelta
	0.02064	32	N	N	N	64	64	1	16	ORSDiceLoss	Adadelta
	0.02389	32	N	N	N	64	64	1	16	ORSDiceLoss	Adadelta
	0.02377	32	N	N	N	32	32	1	32	ORSDiceLoss	Adadelta
	0.33079	32	N	N	N	64	64	1	16	ORSDiceLoss	Adadelta
Initial Filter Count	0.03663	8	N	N	N	32	32	1	32	ORSDiceLoss	Adadelta
	0.02125	16	N	N	N	32	32	1	32	ORSDiceLoss	Adadelta
	0.02429	32	N	N	N	32	32	1	32	ORSDiceLoss	Adadelta
	0.03204	64	N	N	N	32	32	1	32	ORSDiceLoss	Adadelta
	0.04873	128	N	N	N	32	32	1	32	ORSDiceLoss	Adadelta
Brightness	0.03189	32	0.9-1.10	N	N	32	32	1	32	ORSDiceLoss	Adadelta
	0.03001	32	0.8-1.2	N	N	32	32	1	32	ORSDiceLoss	Adadelta
	0.03614	32	0.7-1.3	N	N	32	32	1	32	ORSDiceLoss	Adadelta
	0.02984	32	0.6-1.4	N	N	32	32	1	32	ORSDiceLoss	Adadelta
	0.02864	32	0.5-1.5	N	N	32	32	1	32	ORSDiceLoss	Adadelta
	0.03004	32	0.4-1.6	N	N	32	32	1	32	ORSDiceLoss	Adadelta
	0.03443	32	0.3-1.7	N	N	32	32	1	32	ORSDiceLoss	Adadelta
	0.03418	32	0.2-1.8	N	N	32	32	1	32	ORSDiceLoss	Adadelta
	0.03283	32	0.1-1.9	N	N	32	32	1	32	ORSDiceLoss	Adadelta
0.03829	32	0.1-2.0	N	N	32	32	1	32	ORSDiceLoss	Adadelta	
Noise	0.03408	32	N	N	N	32	32	1	32	ORSDiceLoss	Adadelta
	0.04395	32	N	0-0.01	N	32	32	1	32	ORSDiceLoss	Adadelta
	0.04563	32	N	0-0.02	N	32	32	1	32	ORSDiceLoss	Adadelta
	0.04238	32	N	0-0.03	N	32	32	1	32	ORSDiceLoss	Adadelta
	0.05364	32	N	0-0.03	N	32	32	1	32	ORSDiceLoss	Adadelta
	0.04375	32	N	0-0.04	N	32	32	1	32	ORSDiceLoss	Adadelta
	0.05653	32	N	0-0.05	N	32	32	1	32	ORSDiceLoss	Adadelta

	0.04794	32	N	0-0.06	N	32	32	1	32	ORSDiceLoss	Adadelta
	0.06191	32	N	0-0.07	N	32	32	1	32	ORSDiceLoss	Adadelta
	0.05778	32	N	0-0.08	N	32	32	1	32	ORSDiceLoss	Adadelta
	0.3432	32	N	0-0.09	N	32	32	1	32	ORSDiceLoss	Adadelta
	0.05595	32	N	0-1.0	N	32	32	1	32	ORSDiceLoss	Adadelta
Elastic Transformation	0.02822	32	N	N	N	32	32	1	32	ORSDiceLoss	Adadelta
	0.02654	32	N	N	0.08-0.16	32	32	1	32	ORSDiceLoss	Adadelta
	0.02991	32	N	N	0.07-0.17	32	32	1	32	ORSDiceLoss	Adadelta
	0.02474	32	N	N	0.06-0.18	32	32	1	32	ORSDiceLoss	Adadelta
	0.04061	32	N	N	0.05-0.19	32	32	1	32	ORSDiceLoss	Adadelta
	0.02668	32	N	N	0.04-0.20	32	32	1	32	ORSDiceLoss	Adadelta
	0.03065	32	N	N	0.03-0.21	32	32	1	32	ORSDiceLoss	Adadelta
	0.02359	32	N	N	0.02-0.22	32	32	1	32	ORSDiceLoss	Adadelta
	0.02922	32	N	N	0.01-0.23	32	32	1	32	ORSDiceLoss	Adadelta
	0.02429	32	N	N	0.01-0.60	32	32	1	32	ORSDiceLoss	Adadelta
	0.0292	32	N	N	0.01-0.80	32	32	1	32	ORSDiceLoss	Adadelta
0.02419	32	N	N	0.01-1.00	32	32	1	32	ORSDiceLoss	Adadelta	
Use Validation	0.02854	32	N	N	N	32	32	1	32	ORSDiceLoss	Adadelta
	0.6723	32	N	N	N	32	32	1	32	ORSDiceLoss	Adadelta
	0.02594	32	N	N	N	32	32	1	32	ORSDiceLoss	Adadelta
	0.02586	32	N	N	N	32	32	1	32	ORSDiceLoss	Adadelta
	0.02689	32	N	N	N	32	32	1	32	ORSDiceLoss	Adadelta
Stride Ratio	0.02602	32	N	N	N	32	32	0.25	32	ORSDiceLoss	Adadelta
	0.02647	32	N	N	N	32	32	0.5	32	ORSDiceLoss	Adadelta
	0.0321	32	N	N	N	32	32	0.75	32	ORSDiceLoss	Adadelta
	0.02342	32	N	N	N	32	32	1	32	ORSDiceLoss	Adadelta
	0.04769	32	N	N	N	32	32	1.25	32	ORSDiceLoss	Adadelta
	0.05353	32	N	N	N	32	32	1.5	32	ORSDiceLoss	Adadelta
	0.06333	32	N	N	N	32	32	1.75	32	ORSDiceLoss	Adadelta
	0.08032	32	N	N	N	32	32	2	32	ORSDiceLoss	Adadelta
0.06158	32	N	N	N	32	32	2.25	32	ORSDiceLoss	Adadelta	
Batch Size	0.19526	32	N	N	N	32	32	1	1	ORSDiceLoss	Adadelta

	<b>0.31668</b>	<b>32</b>	<b>N</b>	<b>N</b>	<b>N</b>	<b>32</b>	<b>32</b>	<b>1</b>	<b>2</b>	<b>ORSDiceLoss</b>	<b>Adadelta</b>
	<b>0.44534</b>	<b>32</b>	<b>N</b>	<b>N</b>	<b>N</b>	<b>32</b>	<b>32</b>	<b>1</b>	<b>4</b>	<b>ORSDiceLoss</b>	<b>Adadelta</b>
	<b>0.07265</b>	<b>32</b>	<b>N</b>	<b>N</b>	<b>N</b>	<b>32</b>	<b>32</b>	<b>1</b>	<b>8</b>	<b>ORSDiceLoss</b>	<b>Adadelta</b>
	<b>0.03108</b>	<b>32</b>	<b>N</b>	<b>N</b>	<b>N</b>	<b>32</b>	<b>32</b>	<b>1</b>	<b>16</b>	<b>ORSDiceLoss</b>	<b>Adadelta</b>
	<b>0.02481</b>	<b>32</b>	<b>N</b>	<b>N</b>	<b>N</b>	<b>32</b>	<b>32</b>	<b>1</b>	<b>32</b>	<b>ORSDiceLoss</b>	<b>Adadelta</b>
	<b>0.02413</b>	<b>32</b>	<b>N</b>	<b>N</b>	<b>N</b>	<b>32</b>	<b>32</b>	<b>1</b>	<b>64</b>	<b>ORSDiceLoss</b>	<b>Adadelta</b>
	<b>0.01931</b>	<b>32</b>	<b>N</b>	<b>N</b>	<b>N</b>	<b>32</b>	<b>32</b>	<b>1</b>	<b>128</b>	<b>ORSDiceLoss</b>	<b>Adadelta</b>
<b>Loss Function</b>	<b>0.00156</b>	<b>32</b>	<b>N</b>	<b>N</b>	<b>N</b>	<b>32</b>	<b>32</b>	<b>1</b>	<b>32</b>	<b>Categorical Crossentropy</b>	<b>Adadelta</b>
	<b>0.07289</b>	<b>32</b>	<b>N</b>	<b>N</b>	<b>N</b>	<b>32</b>	<b>32</b>	<b>1</b>	<b>32</b>	<b>CategoricalHinge</b>	<b>Adadelta</b>
	<b>-0.96065</b>	<b>32</b>	<b>N</b>	<b>N</b>	<b>N</b>	<b>32</b>	<b>32</b>	<b>1</b>	<b>32</b>	<b>CosineSimilarity</b>	<b>Adadelta</b>
	<b>0.00181</b>	<b>32</b>	<b>N</b>	<b>N</b>	<b>N</b>	<b>32</b>	<b>32</b>	<b>1</b>	<b>32</b>	<b>KLDivergence</b>	<b>Adadelta</b>
	<b>0.02928</b>	<b>32</b>	<b>N</b>	<b>N</b>	<b>N</b>	<b>32</b>	<b>32</b>	<b>1</b>	<b>32</b>	<b>ORSDiceLoss</b>	<b>Adadelta</b>
	<b>0.05485</b>	<b>32</b>	<b>N</b>	<b>N</b>	<b>N</b>	<b>32</b>	<b>32</b>	<b>1</b>	<b>32</b>	<b>ORSJaccardDistance</b>	<b>Adadelta</b>
<b>Optimizati on Algorithm</b>	<b>0.02256</b>	<b>32</b>	<b>N</b>	<b>N</b>	<b>N</b>	<b>32</b>	<b>32</b>	<b>1</b>	<b>32</b>	<b>ORSDiceLoss</b>	<b>Adadelta</b>
	<b>0.67346</b>	<b>32</b>	<b>N</b>	<b>N</b>	<b>N</b>	<b>32</b>	<b>32</b>	<b>1</b>	<b>32</b>	<b>ORSDiceLoss</b>	<b>Adagrad</b>
	<b>Error</b>	<b>32</b>	<b>N</b>	<b>N</b>	<b>N</b>	<b>32</b>	<b>32</b>	<b>1</b>	<b>32</b>	<b>ORSDiceLoss</b>	<b>Adam</b>
	<b>Error</b>	<b>32</b>	<b>N</b>	<b>N</b>	<b>N</b>	<b>32</b>	<b>32</b>	<b>1</b>	<b>32</b>	<b>ORSDiceLoss</b>	<b>Adamax</b>
	<b>0.66914</b>	<b>32</b>	<b>N</b>	<b>N</b>	<b>N</b>	<b>32</b>	<b>32</b>	<b>1</b>	<b>32</b>	<b>ORSDiceLoss</b>	<b>Ftrl</b>
	<b>0.66761</b>	<b>32</b>	<b>N</b>	<b>N</b>	<b>N</b>	<b>32</b>	<b>32</b>	<b>1</b>	<b>32</b>	<b>ORSDiceLoss</b>	<b>Nadam</b>
	<b>Error</b>	<b>32</b>	<b>N</b>	<b>N</b>	<b>N</b>	<b>32</b>	<b>32</b>	<b>1</b>	<b>32</b>	<b>ORSDiceLoss</b>	<b>RMSprop</b>
	<b>0.35146</b>	<b>32</b>	<b>N</b>	<b>N</b>	<b>N</b>	<b>32</b>	<b>32</b>	<b>1</b>	<b>32</b>	<b>ORSDiceLoss</b>	<b>SGD</b>



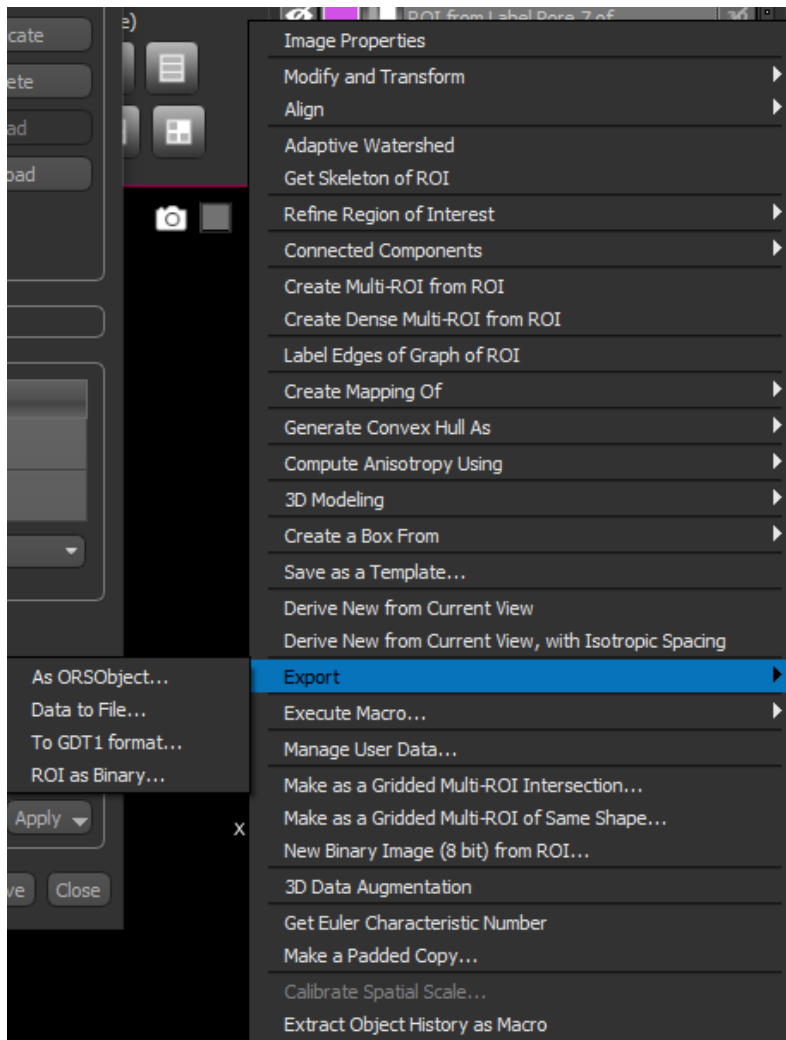
## **Appendix 7.3: Extracting Data With CTAn From ORS Dragonfly Deep Learning Outputs**

*Created by Joshua Taylor (Last Updated: April 6, 2023)*

**Note:** This SOP assumes the reader can generate deep learning outputs (or other ROIs) in ORS Dragonfly. Please refer to other SOPs if this is not the case.



### Task 1: ORS Dragonfly

1. Look for the 'Properties' tab, typically on the right-hand side.
2. Right click on the ROI to be extracted.
3. Hover the mouse over 'Export >' and select 'ROI as binary...' (**Figure 1**).
4. A new prompt will appear asking where and what name to save the file under.
  - a. The location is purely organizational and is up to the user.
  - b. The name **must not** have any spaces.
5. Click 'Ok'.



**Figure 1.** Exporting ROIs from Dragonfly.

## Task 2: Fiji/ImageJ

1. Open Fiji (  or  ).
2. Drag and drop the folder of image files into Fiji.
  - a. A new prompt will appear, just click ‘OK’.
3. Once the image stack has opened, click ‘File’.
4. Hover over ‘Save As >’ and select ‘Image Sequence...’ (**Figure 2**).

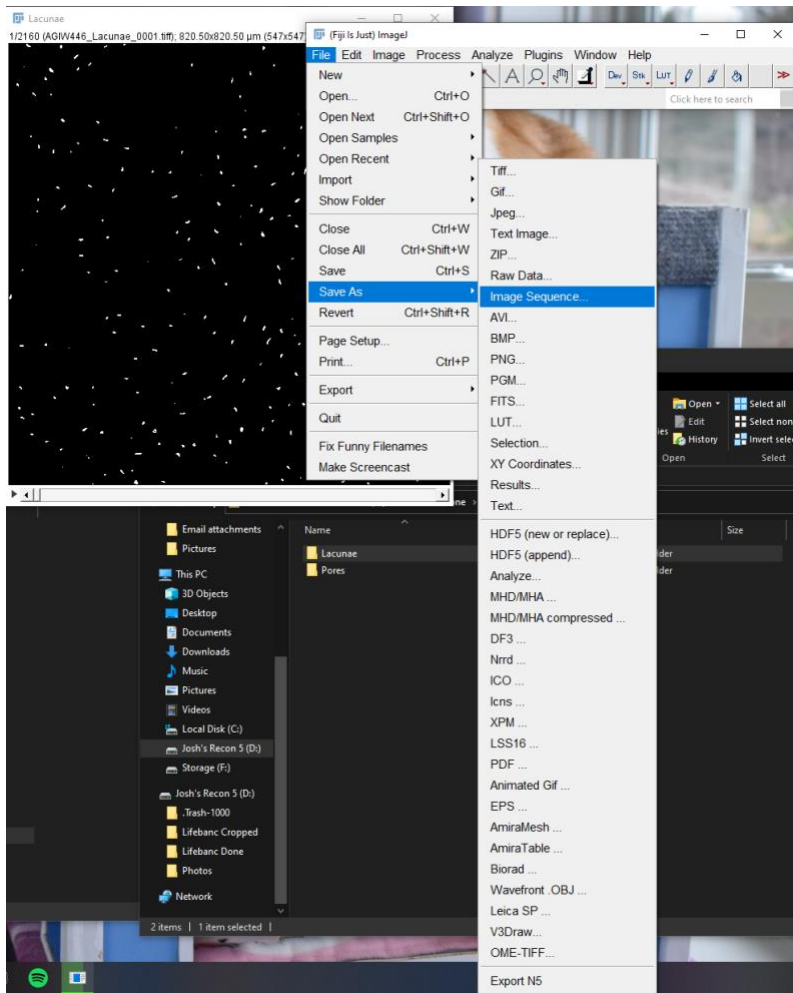
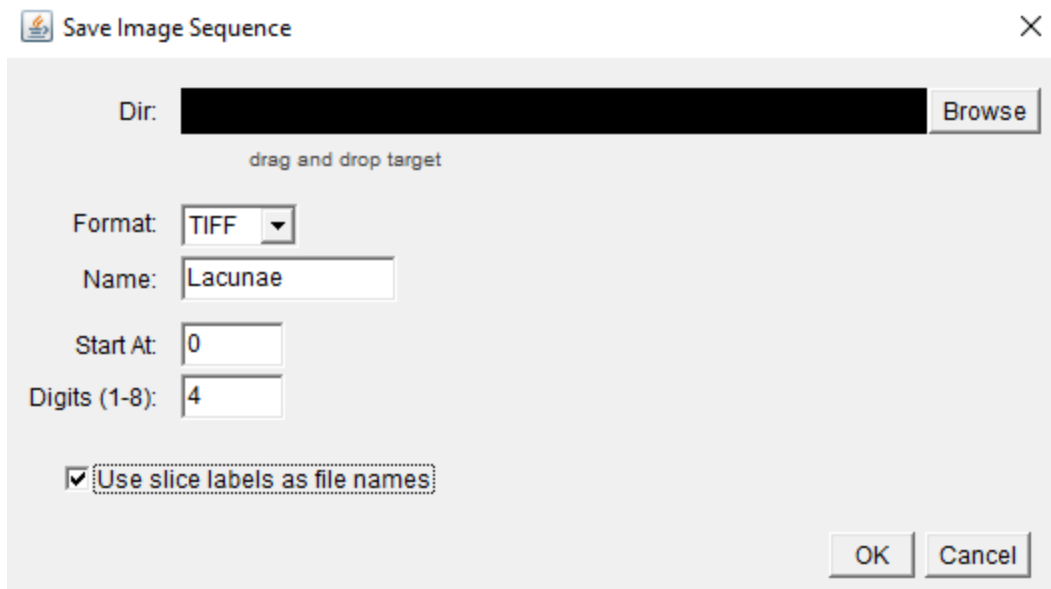


Figure 2. Saving the files in Fiji.

5. A new window will emerge. Make sure the fields match **Figure 3**.




**Figure 3.** The three most important fields are the directory, format (TIFF) and the checkmark for ‘Use slice labels as file names’. Since the last option is check marked, the other options do not matter.

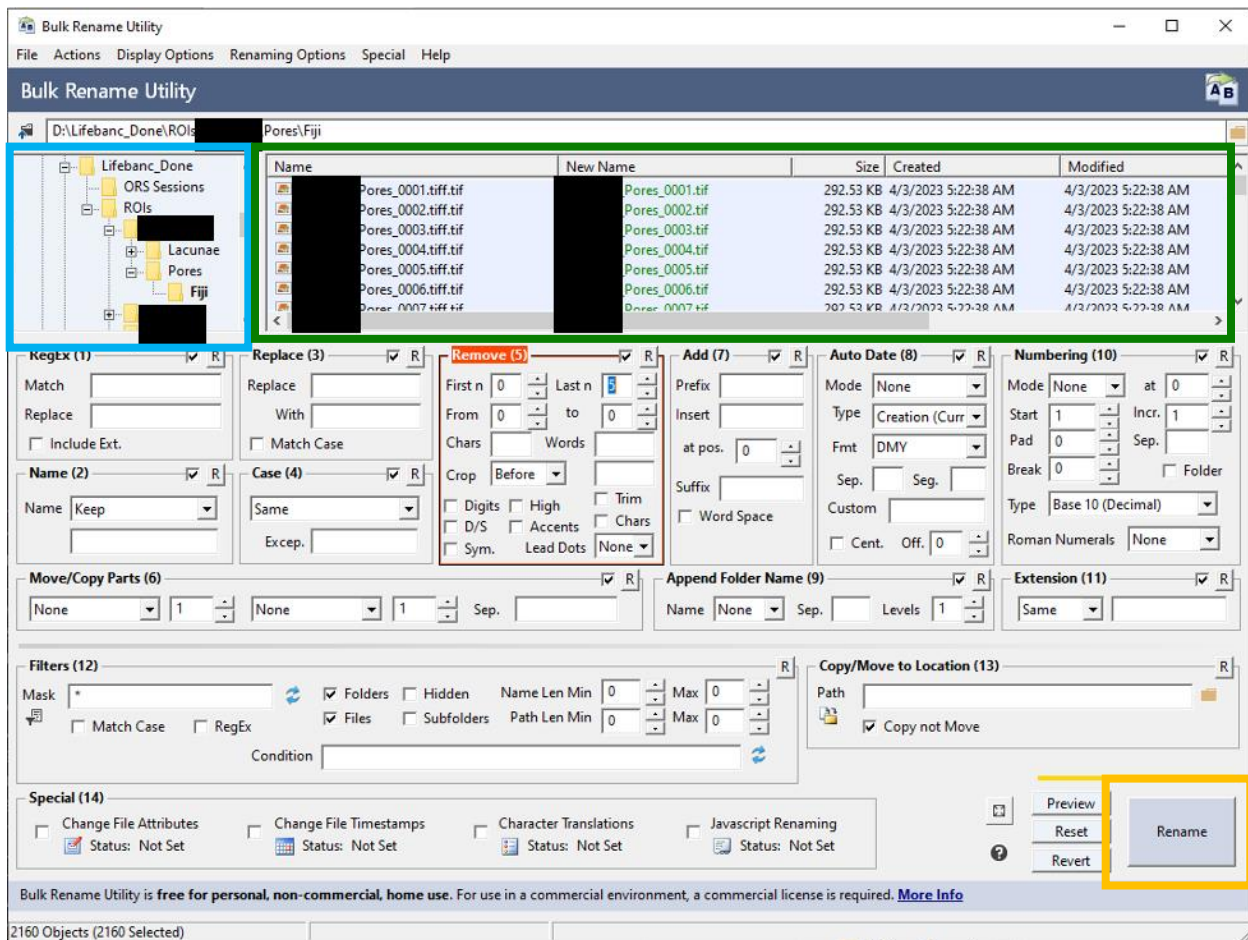
6. Click ‘OK’

### Task 3: Bulk Rename Utility

CTAn does not recognize the filetype ‘.tiff’ which Dragonfly saves as. CTAn recognizes the older ‘.tif’ file format, which is what Fiji saves in. This is the reason that the Fiji tasks exist. However, Fiji will save the document as ‘NameoftheDocument.tiff.tif’ . For some reason, it recognizes ‘.tiff’ as a part of the name and not the type.

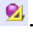
7. Open Bulk Rename Utility .
8. Using the left-hand panel, navigate to the location of the files (**Figure 4**).
9. In the middle panel, click on the first file and press ‘CTRL’ + ‘A’.

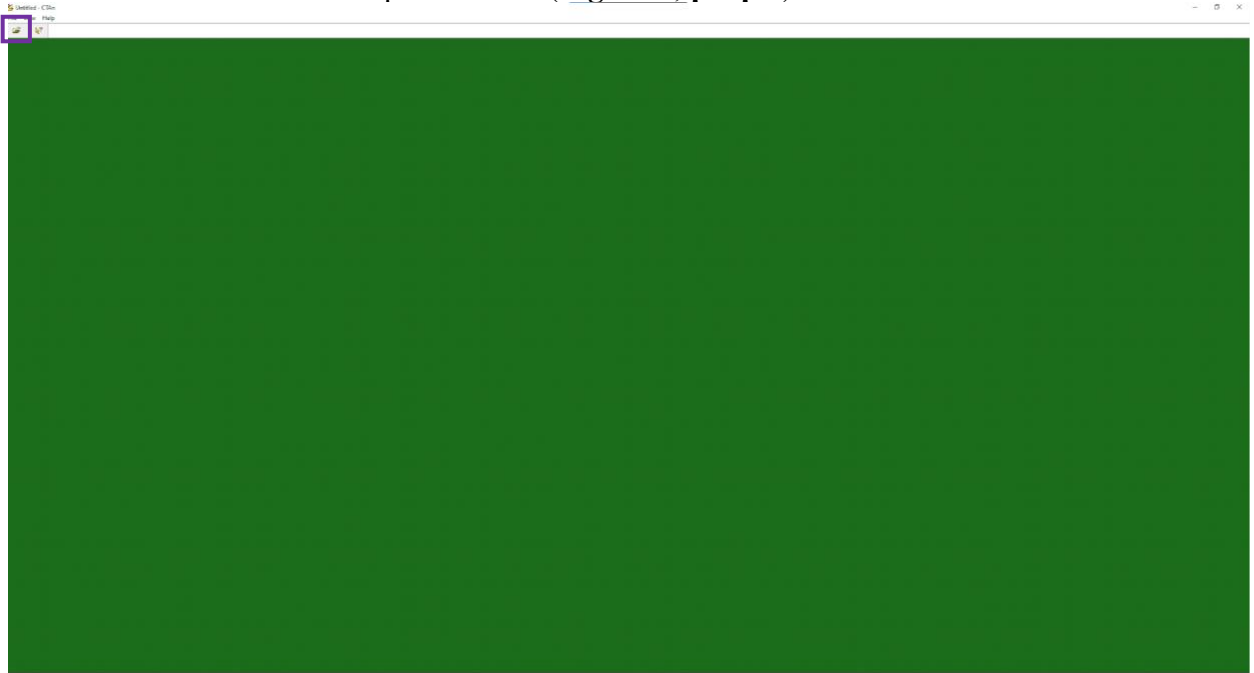
- a. All files should be selected.
10. In the remove box, increase the 'Last n' number until '.tiff' is gone (usually 5).
  11. Click 'Rename'.
  12. A warning will pop-up saying the action is irreversible.
    - a. Take a second to make sure that you are in the right location and working with the right files. When you are confident that it is doing the right action, press 'OK'.



**Figure 4.** The Bulk Rename Utility Application default window. The file panel (green) shows the contents of the immediate directory in the directory window (blue). Once the files appear in the green panel, select the first file and press 'Control' + 'A' so all files are selected. In the remove panel (red), adjust the 'Last n' selection to remove '.tiff' (5). Click the Rename (yellow) button to rename all of the files in just one click.

## Task 4: CTAn

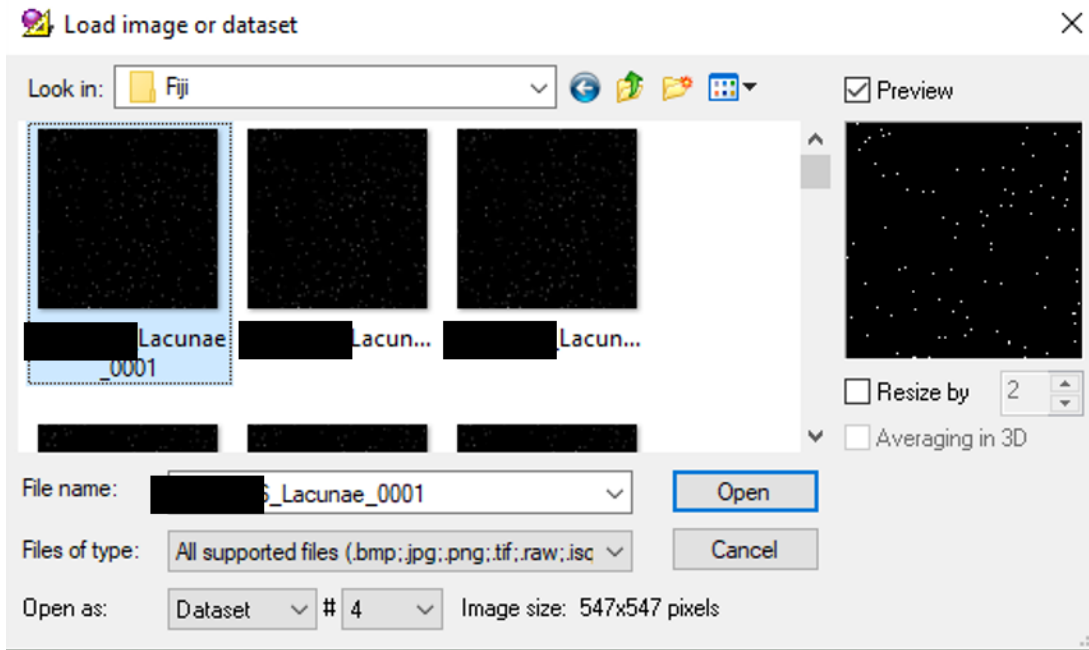
1. Open CTAn .
2. Click the folder icon in the top left corner (**Figure 5, purple**).



**Figure 5.** The default window view of CTAn with no images loaded in.

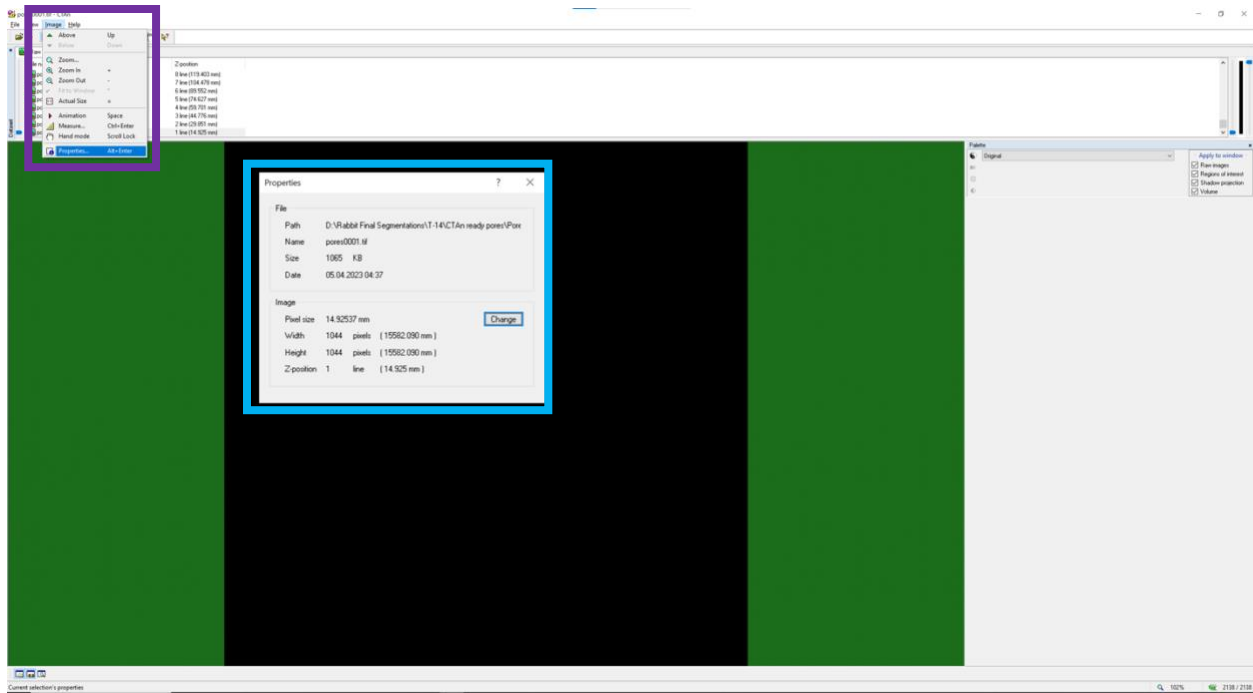
3. Navigate to the images to be opened and click on the first image (**Figure 6**).
  - a. Note the ‘Open as: Dataset’ option should now be usable.
  - b. If the button is unusable or you cannot see the images, there is something wrong with the images that CTAn cannot recognize.
    - i. There are way too many possibilities for these issues to list, but below are the two common problems and solutions.
      1. Problem: Cannot see the images in the CTAn window.
        - a. Solution: use Fiji to convert the filetype to something CTAn recognizes (.tif or .bmp).

2. Problem: The ‘Open as: Dataset’ prompt is not editable.
  - a. Solution: Use Bulk Rename Utility to ensure the image files all end in a 4 padded digit (eg., File\_0001) and there are no spaces in the file name.




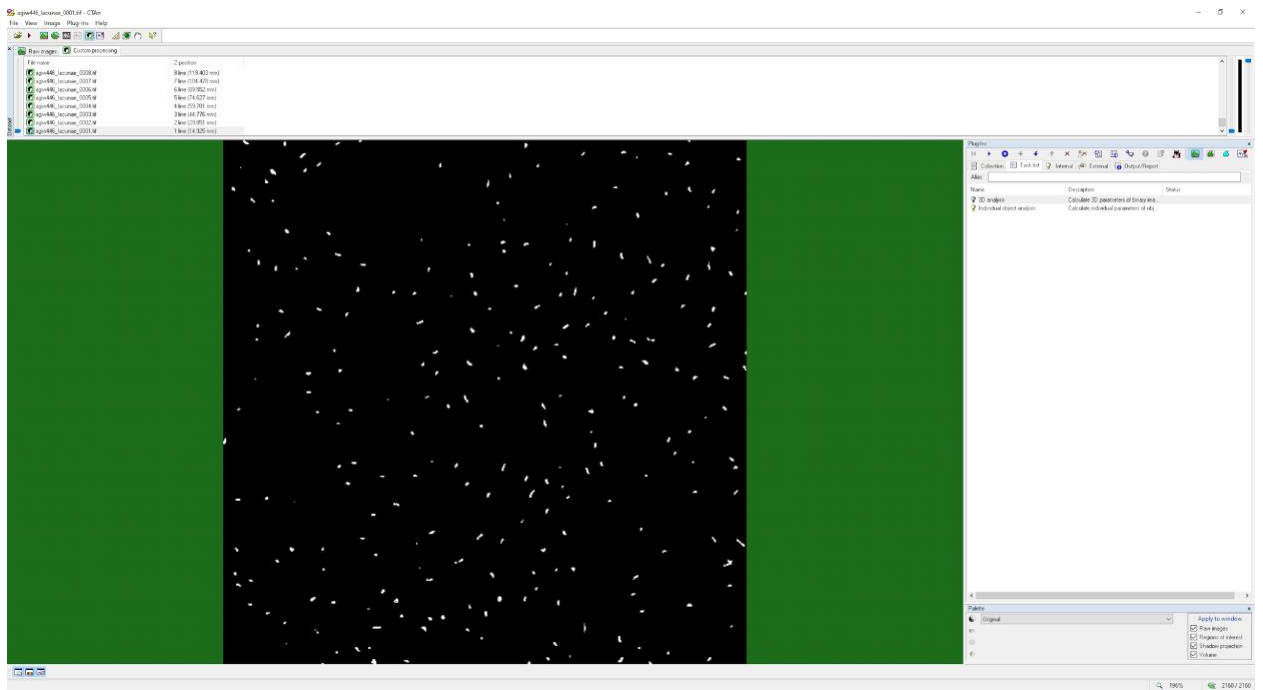
**Figure 6.** CTAn’s GUI for opening a dataset. Note that an image is selected and that the ‘Open as: Dataset’ option is editable and not grayed out. These are signs that opening the dataset in CTAn will be successful.

4. If everything is okay, click ‘Open’.
5. Adjust the pixel size by going to ‘Image’ -> ‘Properties...’ (‘Alt’ + ‘Enter’) (**Figure 7**).
6. A new window will emerge. Click ‘Change’ and enter the correct value.



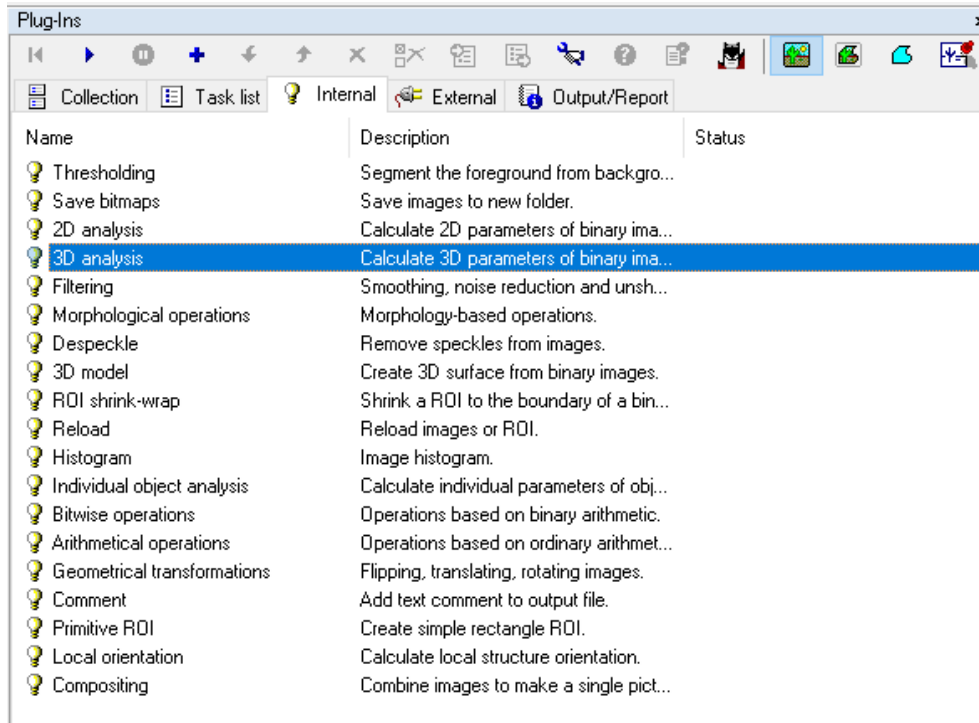
**Figure 7.** Change the pixel size of the image by going to ‘Image’ -> ‘Properties...’ (purple box) and clicking ‘Change’ in the new pop-up window (blue box).

7. Press the custom processing tool .
8. Navigate to the Plug-Ins section on the right panel (**Figure 8 and 9**).



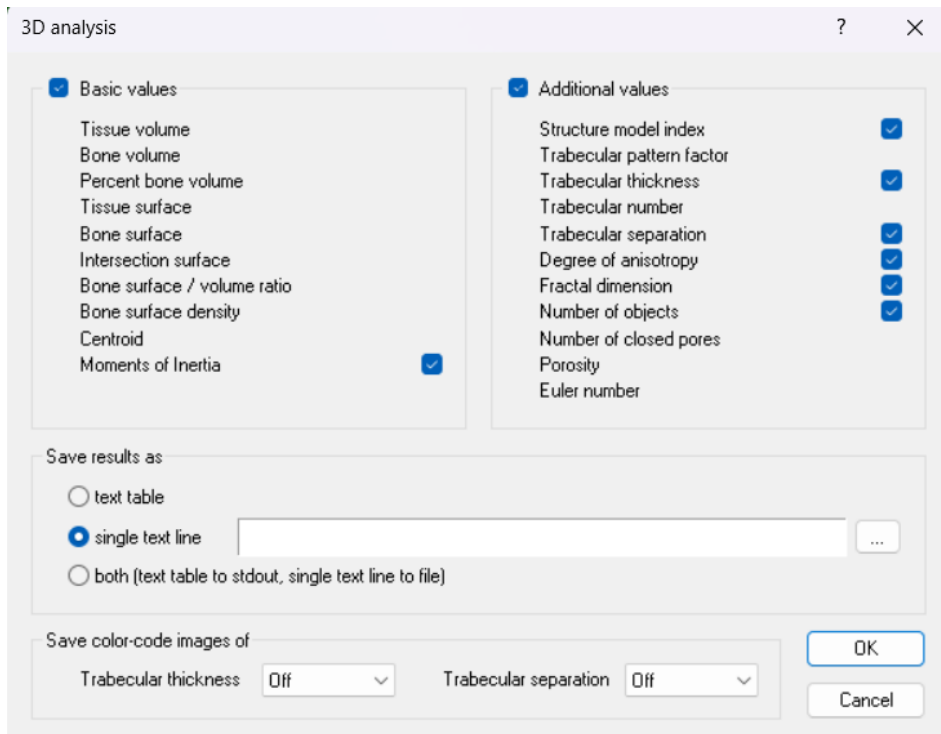
**Figure 8.** The window for CTAn with a sample preloaded and the custom processing tool selected. The Plug-Ins section is to the right of the image.





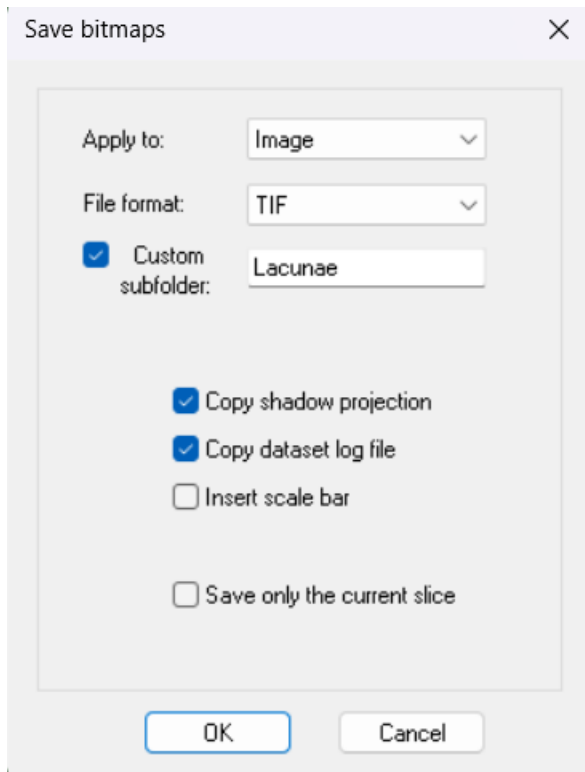
**Figure 9.** A close up of the Plug-Ins section.

9. Double click 'Thresholding'.
  - a. Adjust the values (0 and 50 work).
10. Click the + button twice.
  - a. You are adding the thresholding function twice. The only reason this function is needed is because CTAn will output an error saying it requires a black and white image.
11. Double click 3D analysis, select 'Additional Values', and select all values below it  
(**Figure 10**).



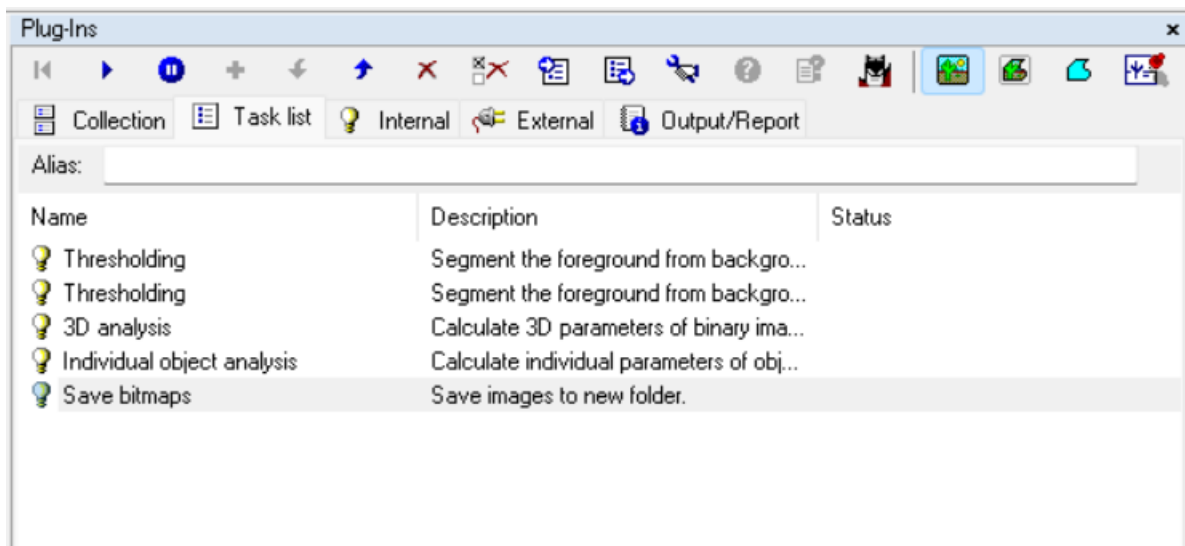
**Figure 10.** The 3D analysis settings.

12. Click the + button.
13. Select ‘Individual object analysis’ and press the + button.
14. Double click ‘Save bitmaps’ and make sure the settings are as follows (**Figure 11**):
  - a. Apply to: Image
  - b. File Format: TIF
  - c. Custom Subfolder: Lacunae or Pores (whichever you are applying it to)







**Figure 11.** Save bitmaps settings.







15. Click 'OK'.
16. Click the + button to add it.
17. (Optional): Export the task list as a .ctt file. Ensures the task list remains the same and you can import it instead of adding each item individually.
18. Press the play button to run through the task list.



**Figure 12.** An example of a completed task list.

**Table 1.** A description of all tools in CTAn's image processing window.

CTAn Processing Tools	
Symbol	Function
	Restores the dataset to its original imported configuration. Any effects of the tasks run on the dataset will be reverted. The original dataset is open and no tasks have been run on it so that is why the appearance of the restore symbol is gray.
	Runs through the entirety of the task list unless paused
	Pauses the task that is highlighted. If you run the task list, CTAn will stop at the paused task. It will not skip it if tasks after it do not have the paused icon
	This adds a task to the task list. The tab is on the task list and not on internal so no tasks can be added at this time, hence its gray appearance.

	<p>The down arrow moves a task down on the task list. The currently selected item is at the bottom of the task list so it cannot be moved down. The gray appearance of the tool is an indicator of that.</p>
	<p>The up arrow moves a task up on the task list. This raises its priority as the first item on the list is applied first.</p>
	<p>Removes the currently selected item from the task list.</p>
	<p>Completely clears the task list of all tasks.</p>
	<p>Import a task list from a file saved locally.</p>
	<p>Exports a task list into a .ctt file. This file can be imported later to save time from reading all of the tasks.</p>